

NOVEL CATALYSTS DEVELOPMENT FOR PRODUCTION OF JET FUEL RANGE
HYDROCARBONS FROM VEGETABLE OILS

A Thesis Submitted to the
College of Graduate and Postdoctoral Studies
In Partial Fulfillment of the Requirements
For the Degree of Doctor of Philosophy
In the Department of Chemical and Biological Engineering
University of Saskatchewan
Saskatoon

By

AFEES AYODEJI AYANDIRAN

© Copyright Afees Ayodeji Ayandiran, April, 2021. All rights reserved.

Unless otherwise noted, copyright of the material in this thesis belongs to the author

Permission to Use

In presenting this thesis in partial fulfillment of the requirements for a Doctor of Philosophy Degree from the University of Saskatchewan, I agree that the Libraries of the University of Saskatchewan may make this thesis freely available for inspection. I further agree that permission for copying of this thesis in any manner, in whole or in part, for scholarly purposes may be granted by Dr. Ajay Dalai and Dr. Yongfeng Hu, who supervised my PhD thesis work or, in their absence, by the Head of Department or the Dean of the College of Engineering. It is understood that any copying or publication or use of this thesis as a whole or parts thereof for financial gain shall not be allowed without any written permission. It is also understood that due recognition shall be given to me and to the University of Saskatchewan in any scholarly use which may be made of any material in my thesis.

Requests for permission to copy or to make other use of material in this thesis in whole or parts shall be addressed to:

Head of the Department of Chemical & Biological Engineering
University of Saskatchewan, 57 Campus Drive
Saskatoon, Saskatchewan S7N 5A9, Canada.

OR

Dean
College of Graduate and Postdoctoral Studies
University of Saskatchewan, 116 Thorvaldson Building,
110 Science Place
Saskatoon, Saskatchewan S7N 5C9, Canada.

Abstract

Production of jet fuel range hydrocarbons via processing of oleic acid has proved to be a viable alternative to the conventional ways of producing jet fuel range hydrocarbons. In this study, the collaborative influence of Fe on the Cu/SiO₂-Al₂O₃ catalysts of 5–15 wt. % Cu loadings was established by changing the contents of Fe in the range of 1–5 wt. % on the optimized 13 wt. % Cu catalyst supported on SiO₂-Al₂O₃. The highest yield (59.5%) and selectivity (73.6%) jet fuel range hydrocarbons were obtained from the evaluation of the Fe(3)-Cu(13)/SiO₂-Al₂O₃ catalyst at 300 °C and 2.07 MPa H₂ pressure, which can be attributed to its desirable textural properties, mild Bronsted acid sites confirmed pyridine FTIR analysis, high metal dispersion revealed from CO chemisorption analysis and TPR analysis.

In the second phase of this research work, the collaborative effects of 1 wt.% Ti, 1 wt.% Zr, and 0.5-2 wt.% Sn on the promising bimetallic catalyst (Fe(3)-Cu(13)/SiO₂-Al₂O₃) were also established through in depth characterization and evaluation to produce jet fuel range hydrocarbons via hydroprocessing of oleic acid. Hydroprocessing of oleic acid over 1 wt. % Sn promoted Fe(3)-Cu(13)/SiO₂-Al₂O₃ catalyst at 320°C, 2.1 MPa H₂ pressure and 8 h, resulted in the highest selectivity (76.8 %) and yield (71.7 %) of jet fuel range hydrocarbons. The promising performance of the catalyst is attributed to its high metal dispersion (revealed from its smallest crystallite size of 5.1 nm and its weakest metal-support interaction), desirable textural properties (revealed from its largest surface area of 571 m²/g and highest pore volume of 0.65 cm³/g).

Maximization of selectivity of jet fuel range hydrocarbons and oleic acid conversion with the best combination of the process parameters involved and evaluation of thermodynamic and kinetic activation parameters is the focus of phase 3 of this research work. Reduced quadratic jet fuel range hydrocarbons selectivity model and reduced cubic oleic acid conversion model of high significance levels and high correlation coefficient were developed. Reaction temperature of 339.5 °C, 6.2 wt.% catalyst concentration, 1.6 MPa H₂ pressure and 8.0 h reaction time were the optimum process parameters that can maximize selectivity of jet fuel range hydrocarbons and oleic acid conversion at 82.2% and 98.2 %, respectively. This process was found to be endothermic, irreversible and non-spontaneous with 45.8kJ/mol activation enthalpy of reaction, -0.25kJ/mol entropy of reaction and the reaction's Gibb's free energy of 198.8kJ/mol at 340 °C. The minimum energy required for the reaction to take place was evaluated to be 50.7kJ/mol.

Production of aviation biofuel that will be competitive with the conventional jet fuel derived from crude oil in terms of its cost effectiveness has been the subject of research in recent years. In the phase 4 of this research work, techno-economic analysis of greenseed canola derived jet fuel range hydrocarbons were carried out using a SuperPro design software. 79200 MT/year of oleic acid (model compound of greenseed canola oil) was hydroprocessed with 1.6 MPa of hydrogen over a 1 wt. % Sn promoted trimetallic catalyst to produce 59345 MT/year jet fuel range hydrocarbons of 99.5 wt. % purity. Economic evaluation of the production process revealed net annual profit of 1.25 million dollars, respectively, with 38.46 % return on investment and 2.6 years payback time.

In conclusion, a novel 1 wt. % Sn promoted on Fe(3)-Cu(13)/SiO₂-Al₂O₃ catalyst was established to be effective and profitable for production of jet fuel range hydrocarbons after optimization of catalysts of different supports, loadings of Sn, Fe and Cu, process parameters and economic evaluation.

Acknowledgements

I would like to sincerely appreciate the efforts of my supervisors Dr. Ajay Dalai, and Dr. Yongfeng Hu for their technical advice and supervision of my research work. Special thanks to my Ph.D. advisory committee, Dr. Venkatesh Meda, Dr. Qiaolin Yang, Dr. Lifeng Zhang, and Dr. Amira Abdulrasoul for evaluating my research progress.

Technical support and suggestions from Ms. Heli Eunike, Ms Rosa Do, Mr. Richard Blondin and Mr. Rlee Prokopishyn are appreciated.

My sincere gratitude to the financial supporters of my research including Canada Research Chair (CRC), Natural Science and Engineering Research Council of Canada (NSERC), and the University of Saskatchewan.

I would like to sincerely appreciate the efforts of Dr. Philip Boahene, Dr. Sonil Nanda, Dr. Venu Babu Borgadda, Dr. Emma Aryee, Dr. Wahab Alabi and Dr. Ankeeta Kurhade for their great support during the course of my program.

Above all, I want to thank my family: my wife Pharm. Zainab Azeez, daughter Maryam Ayandiran, parents Mr. Bashiru Ayandiran and Mrs Sherifah Ayandiran and my siblings for their great support throughout the course of my research.

Dedication

I dedicate this thesis to:

The Almighty God, the one who granted me the knowledge, wisdom and strength during the cause of
my education.

Table of Contents

Permission to Use	i
Abstract	ii
Acknowledgements	iv
Dedication	v
Table of Contents	vi
List of Tables	x
List of Figures	xii
List of Abbreviations	xv
List of Nomenclatures and Symbols	xvi
Glossary of Terms	xvii
CHAPTER 1 Introduction and Thesis Outline	1
1.1 Introduction.....	2
1.2 Knowledge gaps.....	2
1.3 Hypotheses.....	3
1.4 Research objective and sub objectives.....	3
1.5 Organisation of the thesis.....	4
CHAPTER 2 Literature Review	6
2.1 Aviation sector, aviation turbine fuel and sustainability.....	6
2.2 Sustainable aviation fuel conversion routes.....	7
2.3 Hydroprocessed renewable jet fuel.....	9
2.4 Hydroprocessing Catalysts.....	14
2.4.1 Active sites.....	15
2.4.2 Supports.....	17
2.5 Feedstocks for hydroprocessed Renewable jet fuel.....	19
2.6 Kinetics and thermodynamics of hydroprocessing of vegetable oils.....	20
2.7 Technoeconomic analysis.....	21
CHAPTER 3 Experimental Section	23
3.1 Catalyst Synthesis.....	23
3.1.1 Chemical and Materials.....	23
3.1.2 Support preparation.....	23

3.1.3 Catalyst preparation by impregnation.....	23
3.2 Catalyst Characterization.....	24
3.2.1 Inductively Coupled Plasma-Optical Emission Spectrometry (ICP-OES) analysis.....	24
3.2.2 N ₂ - Adsorption/Desorption Measurement.....	24
3.2.3 XRD Analysis.....	25
3.2.4 Fourier Transform Infra-Red Analysis.....	25
3.2.5 XPS Analysis.....	25
3.2.6 H ₂ -TPR Analysis.....	25
3.2.7 Pyridine FTIR Analysis.....	26
3.2.8 CO Chemisorption Analysis.....	26
3.3 Catalyst Evaluation.....	27
3.4 Product Analysis.....	27

CHAPTER 4 Hydroprocessing of Oleic Acid for Production of Jet-Fuel Range

hydrocarbons over Cu and FeCu Catalysts.....	29
4.1 Abstract.....	30
4.2 Introduction.....	30
4.3 Experimental Section.....	33
4.4 Results and Discussion.....	34
4.4.1 N ₂ - Adsorption/Desorption Measurement.....	34
4.4.2 XRD Analysis.....	37
4.4.3 Inductively Coupled Plasma-Optical Emission Spectrometry (ICP-OES) and CO Chemisorption Analyses.....	39
4.4.4 Fourier Transform Infra-Red Analysis.....	39
4.4.5 XPS Analysis.....	40
4.4.6 H ₂ -TPR Analysis.....	42
4.4.7 Pyridine FTIR Analysis.....	42
4.4.8 Catalyst Evaluation.....	46
4.5 Conclusions.....	52

CHAPTER 5 Hydroprocessing of oleic acid for the production of aviation turbine

fuel range hydrocarbons over bimetallic Fe-Cu/SiO₂-Al₂O₃ catalysts promoted by Sn, Ti and Zr.....	53
---	-----------

5.1 Abstract.....	53
5.2 Introduction.....	54
5.3 Experimental Section.....	56
5.4 Results and discussion.....	58
5.4.1 Characterization of support and catalysts.....	58
5.4.2 Catalytic evaluation.....	67
5.5 Conclusions.....	76
CHAPTER 6 Hydroprocessing of oleic acid for production of jet fuel range hydrocarbons over Sn(1)-Fe(3)-Cu(13)/SiO₂-Al₂O₃ catalyst: process parameters optimization, kinetics and thermodynamic study.....	78
6.1 Abstract.....	78
6.2 Introduction.....	79
6.3 Experimental design for modelling and optimization studies.....	82
6.4 Reaction kinetics and thermodynamic activation parameters.....	83
6.5 Results and Discussion.....	85
6.5.1 Modelling and optimization of hydroprocessing of oleic acid.....	85
6.5.2 Kinetic and thermodynamic study of the hydroprocessing reaction.....	96
6.6 Conclusions.....	101
CHAPTER 7 Technoeconomic analysis of jet fuel produced from greenseed canola oil over tin promoted catalyst.....	102
7.1 Abstract.....	102
7.2 Introduction.....	102
7.3 Methods and approaches of the simulation of jet fuel produced from greenseed canola oil over tin promoted catalyst.....	104
7.4 Process Description.....	105
7.5 Techno-economic analysis.....	106
7.6 Conclusions.....	111
CHAPTER 8 Conclusions and Recommendations.....	112
8.1 Overall discussion and conclusions.....	112
8.2 Recommendations.....	113

References	114
Appendix A Additional data.....	127
Appendix B Sample calculations for absence of internal mass transfer limitations.....	134
Appendix C Aspen plus simulation results for production of jet fuel range hydrocarbons.....	135

List of Tables

Table 2.1	Global availability of vegetable oils.....	22
Table 4.1	Textural properties of catalyst samples and their respective supports.....	35
Table 4.2	Cu _{2p_{3/2}} and Fe 2p _{3/2} values for Fe(3)-Cu(13)/SiO ₂ -Al ₂ O ₃ , Fe(3)-Cu(13)/ZSM-5 and Fe(3)-Cu(13)/HZSM catalysts.....	40
Table 4.3	H ₂ uptake and reduction peak temperatures of catalyst samples.....	44
Table 4.4	ICP OES and CO Chemisorption analyses of catalyst samples.....	45
Table 4.5	Yield of C ₈ -C ₁₆ hydrocarbons at t: 2-10 hours; T: 300-340 °C, and P _{H₂} : 2.07 MPa H ₂ pressure.....	51
Table 5.1	ICP-OES analysis of catalyst samples.....	59
Table 5.2	Textural properties of catalyst samples.....	61
Table 5.3	XPS deconvolution results of catalyst samples.....	66
Table 5.4	H ₂ uptake and reduction peak temperatures of catalyst samples.....	66
Table 5.5	Amount of Brønsted and Lewis acid sites from pyridine-FTIR analysis.....	69
Table 5.6	Effect of impeller speed on oleic acid conversion and selectivity of jet fuel range hydrocarbons at 320°C and 2.1 MPa H ₂ pressure over 1 wt.% Sn supported catalyst.....	69
Table 5.7	Selectivity of C ₈ -C ₁₆ hydrocarbons at different temperatures (300-340°C) and reaction time (2-8 h) under 2.1 MPa H ₂ pressure.....	71
Table 5.8	Product distribution of hydrocarbons at 320°C in 8 h under 2.1 MPa H ₂ pressure.....	72
Table 5.9	Selectivity of C ₈ -C ₁₆ hydrocarbons at 320°C in 8 h under 2.1 MPa H ₂ Pressure.....	72
Table 5.10	Catalysts productivity towards C ₈ -C ₁₆ hydrocarbons at 300-340°C in 8 h under 2.1 MPa H ₂ pressure.....	74
Table 5.11	Comparison of the performance of 1 wt.% Sn-supported catalyst with other catalysts evaluated for jet fuel range hydrocarbons from literature.....	76
Table 6.1	Process Parameters and levels used for face-centered central composite design.....	83
Table 6.2	Face-centered central composite design matrix with four operational parameters, corresponding levels and responses for hydroprocessing of oleic acid.....	86

Table 6.3	Model adequacy verification for the face-centered central composite design: Oleic acid conversion.....	87
Table 6.4	Model adequacy verification for the face-centered central composite design: Selectivity of jet fuel range hydrocarbons.....	87
Table 6.5	Analysis of variance and regression analysis of the reduced cubic models for oleic acid conversion.....	89
Table 6.6	Analysis of variance and regression analysis of the reduced cubic models for selectivity of jet fuel range hydrocarbons.....	90
Table 6.7	Kinetic and thermodynamic parameters for oleic acid Hydroprocessing.....	100
Table 6.8	A review on activation energy of hydroprocessing of fatty acids/ Triglycerides.....	100
Table 7.1	Properties and compositions of the main streams.....	117
Table 7.2	Cost of Equipment.....	108
Table 7.3	Estimation of fixed capital for the plant operation.....	108
Table 7.4	Profitability analysis.....	108
Table 7.5	Unit Production Cost/Revenue and economic feasibility criteria.....	110
Table 7.6	A review on minimum jet fuel selling price from technoeconomic analyses of jet fuel production.....	110
Table A.1.	Selectivity of lighter hydrocarbons at t: 8 hrs; T: 300 °C, and P _{H2} : 2.07 MPa H ₂ pressure.....	132
Table A.2.	Selectivity of C ₈ -C ₁₆ hydrocarbons at t: 8 hrs; T: 300 °C, and P _{H2} : 2.07 MPa H ₂ pressure.....	132
Table A.3.	Catalysts productivity towards C ₈ -C ₁₆ hydrocarbons at t: 8 hours; T: 300-340 °C, and P _{H2} : 2.07 MPa H ₂ pressure.....	133

List of Figures

Figure 4.1	Wide angle XRD patterns of SiO ₂ -Al ₂ O ₃ , Cu(5)/SiO ₂ -Al ₂ O ₃ , Cu(10)/SiO ₂ -Al ₂ O ₃ , Cu(13)/SiO ₂ -Al ₂ O ₃ and Cu(15)/SiO ₂ -Al ₂ O ₃ , Fe(1)-Cu(13)/SiO ₂ -Al ₂ O ₃ , Fe(2)-Cu(13)/SiO ₂ -Al ₂ O ₃ , Fe(3)-Cu(13)/SiO ₂ -Al ₂ O ₃ and Fe(5)-Cu(13)/SiO ₂ -Al ₂ O ₃ catalysts.....	36
Figure 4.2	XRD patterns of SiO ₂ -Al ₂ O ₃ , ZSM-5 and HZSM-5 supports; Fe(3)-Cu(13)/SiO ₂ -Al ₂ O ₃ , Fe(3)-Cu(13)/ZSM-5 and Fe(3)-Cu(13)/HZSM catalysts.....	38
Figure 4.3	FTIR spectra of SiO ₂ -Al ₂ O ₃ , ZSM-5 and HZSM-5 supports; Fe(3)-Cu(13)/SiO ₂ -Al ₂ O ₃ , Fe(3)-Cu(13)/ZSM-5 and Fe(3)-Cu(13)/HZSM catalysts.....	41
Figure 4.4	Cu2p and Fe2p XPS spectra of (a,b) FeCu/HZSM (c,d) FeCu/SiO ₂ -Al ₂ O ₃ (e,f) FeCu/ZSM-5 catalysts.....	43
Figure 4.5	TPR profiles of Fe(3)-Cu(13)/SiO ₂ -Al ₂ O ₃ , Fe(3)-Cu(13)/ZSM and Fe(3)-Cu(13)/HZSM catalysts.....	45
Figure 4.6	Selectivity of jet fuel hydrocarbons at 300 °C and 2.07 MPa H ₂ pressure over the Brønsted/Lewis acid sites ratio and metal dispersion of Fe(3)-Cu(13)/SiO ₂ -Al ₂ O ₃ , Fe(3)-Cu(13)/ZSM-5 and Fe(3)-Cu(13)/HZSM-5 catalysts.....	46
Figure 4.7	Conversion of oleic acid and Selectivity of jet fuel hydrocarbons at different temperatures and 2.07 MPa H ₂ pressure over (A) Cu(5)/SiO ₂ -Al ₂ O ₃ , (B) Cu(10)/SiO ₂ -Al ₂ O ₃ , (C) Cu(13)/SiO ₂ -Al ₂ O ₃ and (D) Cu(15)/SiO ₂ -Al ₂ O ₃ catalysts.....	47
Figure 4.8	Conversion of oleic acid and selectivity of jet fuel hydrocarbons at different temperatures and 2.07 MPa H ₂ pressure over (E) Fe(1)-Cu(13)/SiO ₂ -Al ₂ O ₃ , (F) Fe(2)-Cu(13)/SiO ₂ -Al ₂ O ₃ , (G) Fe(3)-Cu(13)/SiO ₂ -Al ₂ O ₃ and (H) Fe(5)-Cu(13)/SiO ₂ -Al ₂ O ₃ catalysts.....	49
Figure 4.9	Conversion of oleic acid and selectivity of jet fuel hydrocarbons at different temperatures and 2.07 MPa H ₂ pressure over Fe(3)-Cu(13)/HZSM-5 catalysts.....	50
Figure 4.10	Conversion of oleic acid and selectivity of jet fuel hydrocarbons at different temperatures and 2.07 MPa H ₂ pressure over Fe(3)-Cu(13)/ZSM-5 catalyst.....	50
Figure 4.11	Conversion of oleic acid and selectivity of jet fuel hydrocarbons at different temperatures and 2.07 MPa H ₂ pressure over	

	Fe(3)-Cu(13)/SiO ₂ -Al ₂ O ₃ catalyst.....	51
Figure 5.1	N ₂ -adsorption isotherms of support, base catalyst and Ti, Zr and Sn supported catalysts.....	59
Figure 5.2	XRD patterns of support, base catalyst and Ti, Zr and Sn supported Catalysts.....	62
Figure 5.3	XPS spectra of 0.5 wt.% Sn (a-c), 1 wt.% Sn (d-f), 1 wt.% Sn (g-i), 1 wt.% Ti (j-l) and 1 wt.% Zr (m-o) supported catalysts.....	64
Figure 5.4	FTIR spectra of support, base catalyst and Ti, Zr and Sn supported Catalysts.....	65
Figure 5.5	TPR profiles of base catalyst and Ti, Zr and Sn supported catalysts.....	65
Figure 5.6	Oleic acid conversion and selectivity of jet fuel range hydrocarbons at 300-340°C and 2.1 MPa H ₂ pressure over 1 wt.% Ti-supported catalyst.....	70
Figure 5.7	Oleic acid conversion and selectivity of jet fuel range hydrocarbons at 300-340°C and 2.1 MPa H ₂ pressure over 1 wt.% Zr-supported catalyst.....	70
Figure 5.8	Oleic acid conversion and selectivity of jet fuel range hydrocarbons at 300-340°C and 2.1 MPa H ₂ pressure over 1 wt.% Sn-supported catalyst.....	71
Figure 5.9	Yield of jet fuel range hydrocarbons at 320°C, 8 h and 2.1 MPa H ₂ pressure over crystallite size of base catalyst (B), 1 wt.% Ti (C), 1 wt.% Zr (D), 1 wt.% Sn (E), 0.5 wt.% Sn (F) and 2 wt.% Sn (G) supported catalysts.....	73
Figure 5.10	Longevity test showing Oleic acid conversion and selectivity of jet fuel range hydrocarbons at 320°C, 8-150 h and 2.1 MPa H ₂ pressure over 1 wt.% Sn supported catalyst.....	75
Figure 5.11	Reusability test showing Oleic acid conversion and yield of jet fuel range hydrocarbons at 320°C, 7 reaction runs and 2.1 MPa H ₂ pressure over 1 wt.% Sn supported catalyst.....	76
Figure 6.1	Parity plot of the predicted versus experimental oleic acid conversion.....	91
Figure 6.2	Parity plot of the predicted versus experimental selectivity of jet fuel range hydrocarbons.....	91
Figure 6.3	3D response surface plot of the main and interaction effects of H ₂ pressure and temperature on oleic acid conversion.....	92

Figure 6.4	3D response surface plot of the main and interaction effects of H ₂ pressure and temperature on selectivity of jet fuel range hydrocarbons.....	93
Figure 6.5	3D response surface plot of the main and interaction effects of reaction time and catalyst concentration on oleic acid conversion.....	93
Figure 6.6	3D response surface plot of the main and interaction effects of reaction time and catalyst concentration on selectivity of jet fuel range hydrocarbons....	94
Figure 6.7	Experimental limit and optimum values of process parameters and responses...	97
Figure 6.8	Effect of reaction temperature (300-340 °C) on oleic acid conversion, 1.6 MPa H ₂ pressure and 6.2 wt. % catalyst concentration.....	98
Figure 6.9	ln(1/(1-0.01X)) versus reaction time at reaction temperature of 300-340 °C, 1.6 MPa H ₂ pressure and catalyst concentration of 6.2 wt.%.....	99
Figure 6.10	ln(k) versus 1/T at reaction temperature of 300-340 °C, 1.6 MPa H ₂ pressure and catalyst concentration of 6.2 wt.%.....	99
Figure 6.11	ln(k/T) versus 1/T at reaction temperature of 300-340 °C, 1.6 MPa H ₂ Pressure and catalyst concentration of 6.2 wt.%.....	101
Figure 7.1	Process flow diagram for jet fuel production from green seed canola oil using 1 wt. % Sn promoted Fe(3)-Cu(13) catalyst.....	106
Figure A.1	Temperature Calibration of the Parr Reactor.....	127
Figure A.2	GC Calibration curve for the jet fuel range hydrocarbons.....	128
Figure A.3	N ₂ -adsorption isotherms of SiO ₂ -Al ₂ O ₃ , Cu(5)/SiO ₂ -Al ₂ O ₃ , Cu(10)/SiO ₂ -Al ₂ O ₃ , Cu(13)/SiO ₂ -Al ₂ O ₃ and Cu(15)/SiO ₂ -Al ₂ O ₃ , Fe(1)-Cu(13)/SiO ₂ -Al ₂ O ₃ , Fe(2)-Cu(13)/SiO ₂ -Al ₂ O ₃ , Fe(3)-Cu(13)/SiO ₂ -Al ₂ O ₃ and Fe(5)-Cu(13)/SiO ₂ -Al ₂ O ₃ catalysts.....	129
Figure A.4	N ₂ -adsorption isotherms of SiO ₂ -Al ₂ O ₃ , ZSM-5 and HZSM-5 supports; Fe(3)-Cu(13)/SiO ₂ -Al ₂ O ₃ , Fe(3)-Cu(13)/ZSM-5 and Fe(3)-Cu(13)/HZSM catalysts.....	130
Figure A.5	Py-FTIR spectra of SiO ₂ -Al ₂ O ₃ , ZSM-5 and HZSM-5 supports; Fe(3)-Cu(13)/SiO ₂ -Al ₂ O ₃ , Fe(3)-Cu(13)/ZSM-5 and Fe(3)-Cu(13)/HZSM catalysts.....	131

Abbreviations

ATF	Aviation turbine fuel
BJH	Barrett-Joyner-Halenda
FT	Fischer-Tropsch
FTIR	Fourier transform infrared
GHG	Greenhouse gas
HDCJ	Hydrotreated depolymerized cellulosic jet fuel
HDO	Hydrodeoxygenation
HRJ	Hydroprocessed Renewable Jet Fuel
IATA	International Air Transport Association
ICAO	International Civil Aviation Organization
ICP-OES	Inductively Coupled Plasma-Optical Emission Spectrometry
IMEC(B)	Integrated molar extinction coefficients of Bronsted acid site
IMEC(L)	Integrated molar extinction coefficients of Lewis acid site
IT(B)	Integrated transmittances of Bronsted acid sites
IT(L)	Integrated transmittances of Lewis acid sites
TPR	Temperature Programmed Reduction
XPS	X-ray Photoelectron Spectroscopy Analysis

List of Nomenclature and Symbols

A	pre-exponential factor (h^{-1})
C	catalyst concentration (wt.%)
ΔG	Gibbs free energy (J/kg)
H	Planck constant (6.62×10^{-34} Js)
HZSM-5	Protonated Zeolite Socony Mobil-5
ΔH	activation enthalpy of reaction (J/kg)
k	kinetic rate constant (h^{-1})
K_B	Boltzman constant (1.38×10^{-23} J/K)
P	H_2 pressure (MPa)
R	universal molar gas constant (8.314 J/mol K)
R^2	correlation coefficient (%)
S	Selectivity of jet fuel range hydrocarbon (%)
ΔS	activation entropy of reaction (J/kgK)
t	reaction time (h)
T	absolute temperature (Kelvin)
X	Oleic acid conversion (%)
ZSM-5	Zeolite Socony Mobil-5

Glossary of Terms

wt. % metal loading	$(\text{Weight of metal} \times 100) / (\text{Weight of metal} + \text{Weight of support})$
Oleic acid conversion	Percentage of oleic acid converted during the reaction
Product selectivity	Percentage ratio of the desired jet fuel range hydrocarbons produced to the undesired products
Product yield	Percentage ratio of the desired jet fuel range hydrocarbons produced to oleic acid consumed
Catalyst concentration	Weight percentage of the catalyst in the feed
H ₂ pressure	Pressure of hydrogen in the reactor before the reaction

CHAPTER 1

Introduction and Thesis Outline

1.1 Introduction

Air transport plays an essential role in the daily life of the contemporary world (Wang and Tao, 2016). This leads to annual global consumption of 1.7 billion barrels of conventional jet fuel (Thushara et al., 2015; Wei-Cheng, 2016). About 9.5% of conventional crude oil is utilized for jet fuel production (Wang and Tao, 2016). The challenges of environmental impact and the declining petroleum resources have made it imperative to produce sustainable fuels using renewably clean technologies of high energy efficiency (Liu et al., 2013). Bio-jet fuels provide solutions to these problems due to their high renewability, sustainability and energy efficiency.

The commercial viability of aviation biofuel strongly depends on the production cost. Process design, efficiency of feedstock conversion, feedstocks cost and composition, market value of byproducts and conservation of energy have significant effects on the production cost of bio-jet fuel. The cost of petroleum-derived jet fuel has been faced by large fluctuations. Based on the annual global consumption of 1.7 billion barrels of jet fuel stated earlier, a penny increase per barrel will result in \$17 million increase in annual fuel cost. The cost of production of bio-jet fuel is estimated to decrease from \$254 in 2017 to \$107 per barrel in 2030 as a result of the improvement in process technology (Wang and Tao, 2016). Bio-jet fuel will occupy three-tenths of the annual global consumption in 2030 of jet fuel due to this predicted decrease. There is a need for significant improvements in the productivity of feedstocks, the yield of oil extract and the increase in process energy in order to reduce the cost of production of bio-jet fuel (Wang and Tao, 2016).

Production of bio-jet fuels using different renewable resources such as halophytes, camelina, algae, waste oil and jatropha is presently being researched. The vegetable oils used as feedstocks for bio-jet fuel include sunflower, cottonseed, rapeseed, soybean, palm, peanut, camelina, jatropha and microalgal oils. These feedstocks are better than the feedstocks used for crude oil based conventional jet fuel due to their renewability, sustainability and environmental friendliness. Non-edible oils are preferred for bio-jet fuel production in order to avert the food-fuel crisis caused by edible oils. The lowest priced bio-jet fuel feedstocks are the abundant non-edible

oils including used cooking oil, which are obtained through the accumulation of oil from bakeries, hotels and restaurants (Mohammad et al., 2013).

Thermochemical and biochemical processes are among the process technologies utilized to produce aviation fuel from renewable sources (Wang and Tao, 2016). Sustainable aviation fuels include hydroprocessed renewable jet fuels (HRJ), Fischer-Tropsch jet fuels (FTJ), bioalcohol and biomethane. Hydroprocessed renewable jet fuels are produced from vegetable oils using hydroprocessing technologies which encompass hydrotreating, deoxygenation, hydrocracking and isomerization reactions. Fischer-Tropsch jet fuels are produced from solid-based feedstocks through gasification, Fischer-Tropsch synthesis and hydroprocessing (Thushara et al., 2015). For hydroprocessed renewable jet fuels and Fischer-Tropsch jet fuels production technologies, the standard specification is ASTM specification D7566 (Thushara et al., 2015). The process technologies for hydroprocessing of renewable jet fuels are in the stage of research and development.

The hydroprocessed renewable jet fuels have high energy density, and emission of greenhouse gases from its combustion is low. This jet fuel is aromatic and sulphur free. They have storage and thermal stability with high cetane number (Wang and Tao, 2016). They find application in conventional aviation turbine engines without modification and without blending with conventional crude oil-derived jet fuels. Hydroprocessed jet fuels are suitable for high altitude aircrafts due to their high cold flow properties. Propane is the major byproduct from the oil hydroprocessing, with higher economic value when compared with glycerol, the byproduct of the transesterification process (Wei-Cheng, 2016).

1.2 Knowledge gaps

The literature review discussed in chapter 2, on jet fuel range hydrocarbons production from vegetable oil revealed the following knowledge gaps:

1. There are limited reported studies on the evaluation of Cu and CuFe bimetallic catalysts supported on $\text{SiO}_2\text{-Al}_2\text{O}_3$, ZSM-5 and HZSM-5 in comparison for hydroprocessing of oleic acid.
2. The effects of promoters such as Sn, Ti, and Zr on the CuFe system for hydroprocessing of oleic acid are limited.

3. There are limited reported studies on process parameter optimization and kinetics of hydroprocessing of oleic acid to jet fuel range hydrocarbons over trimetallic catalysts.
4. Technoeconomic analysis of jet fuel produced from vegetable oil over tin promoted Fe(3)-Cu(13)/SiO₂-Al₂O₃ catalyst has not been explored.

1.3 Hypothesis

Based on the above knowledge gaps, the hypotheses are stated below:

1. Fe favors hydrodeoxygenation and copper aids hydrogen activation and adsorption.
2. Metals such as tin (Sn), titanium (Ti) and zirconium (Zr) favor oxygen abstraction due to their oxophilicity thus inspiring the HDO process.
3. Process parameters optimization is essential to maximize catalyst performance, and provide data for technoeconomic analysis. The kinetic study would provide insight into the kinetic parameters of hydroprocessing reaction.
4. Techno-economic analysis would show the cost effectiveness of biojet fuel production via hydroprocessing of oleic acid as compared to petroleum-derived jet fuel

1.4 Research objective and sub-objectives

The overall objective is to produce jet fuel range hydrocarbons of high selectivity from model oleic acid compound by developing novel and effective catalysts. Research sub-objectives are outlined to evaluate the hypotheses stated earlier and fill the above listed knowledge gaps. The following four phases explain the sub-objectives of this research work.

Phase 1: To produce jet fuel range hydrocarbons of high selectivity via hydroprocessing over Cu and CuFe catalysts supported on SiO₂-Al₂O₃, ZSM-5 and HZSM-5 and evaluate their properties using different characterization techniques, the following work was planned.

- Production of jet fuel range hydrocarbons of high selectivity via hydroprocessing over Cu/SiO₂-Al₂O₃ catalysts with different Cu loadings and the evaluation of their properties using different characterization techniques
- Production of jet fuel range hydrocarbons of high selectivity via hydroprocessing over iron promoted Cu(13)/SiO₂-Al₂O₃ catalysts with different Fe loadings and the evaluation of their properties using different characterization techniques, the following work was planned.

- Production of jet fuel range hydrocarbons of high selectivity via hydroprocessing over Fe(3)-Cu(13) catalysts with different supports (ZSM-5, HZSM-5 and SiO₂-Al₂O₃) and the evaluation of their properties using different characterization techniques

Phase 2: To produce jet fuel range hydrocarbons of high selectivity via hydroprocessing over Fe(3)-Cu(13)/SiO₂-Al₂O₃ catalysts promoted by Ti, Zr and Sn and evaluate their properties using different characterization techniques, the following work was planned

- Production of jet fuel range hydrocarbons of high selectivity via hydroprocessing over Fe(3)-Cu(13)/SiO₂-Al₂O₃ catalysts promoted by 1 wt.% Ti, Zr and Sn and the evaluation of their properties using different characterization techniques
- Production of jet fuel range hydrocarbons of high selectivity via hydroprocessing over Fe(3)-Cu(13)/SiO₂-Al₂O₃ catalysts promoted by 0.5 – 2 wt.% Sn and the evaluation of their properties using different characterization techniques

Phase 3: To optimize process parameters and conduct kinetic studies for production of jet fuel range hydrocarbons via hydroprocessing over 1 wt. % Sn promoted trimetallic catalyst, the following work was planned.

- Optimization of process parameters (reaction temperature, hydrogen pressure, catalyst concentration and reaction time) for production of jet fuel range hydrocarbons via hydroprocessing over 1 wt. % Sn promoted trimetallic catalyst.
- Investigation of kinetic and thermodynamic parameters of the hydroprocessing reaction

Phase 4: Techno-economic analysis for production of jet fuel range hydrocarbons over 1 wt. % Sn promoted catalyst

- Process simulation and techno-economic assessment of production of jet fuel range hydrocarbons using SuperPro design software

1.5 Organization of the thesis

The structure of this PhD thesis is based on the manuscript-style thesis preparation guidelines of College of Graduate and Postdoctoral studies. Thesis introduction and research background in terms of literature review and experimental section are provided in Chapters 1,2 and 3, respectively. Published manuscript constitutes a considerable portion of the thesis. The manuscripts were published in peer reviewed journals and described in Chapters 4, 5 and 6. Chapter 7 consists of an unpublished manuscript that is intended to be submitted as a book chapter.

The overall conclusions and recommendation from this dissertation are provided in Chapter 8. References and supporting information relating to this research are presented in the Reference and Appendix sections, respectively.

CHAPTER 2

Literature Review

Contribution of this chapter to overall study

This chapter is focused on recent developments in sustainable aviation fuel, hydroprocessed renewable fuel, hydroprocessing catalysts, kinetics and thermodynamics of hydroprocessing reactions.

2.1 Aviation sector, aviation turbine fuel and sustainability

The aviation industry is considered as the main driver of globalization, as it is the most convenient way of bridging large distances within a relatively short time (Lenaerts et al., 2021). The aviation sector is responsible for the transportation of 35 % of world trade shipments by value and 58 % of all international tourists. 2.3 billion barrels of jet fuel was used to power aircraft in 2019 (ATAG, 2021). Increase in consumption of jet fuel is paralleled with aviation greenhouse gas emissions. 915 million tons of greenhouse gas was emitted by flights in 2019. This accounts for 2.1 % of all anthropogenic greenhouse emissions (ATAG, 2021).

The effect of greenhouse gas emissions associated with the aviation industry is different from other means of transportation because they mainly occur at high altitude. High altitude emissions have potential of instigating physical and chemical processes that have grim climate change consequences. Thus, in comparison with other means of transportation, aviation emissions have the greatest influence on climate change. Fuel combustion in aircraft engines results in emissions of carbon (IV)oxide (CO_2), water vapour, nitrogen oxides, soot and aerosols (Jardine et al., 2005). Carbon (IV) oxide hangs around in the atmosphere for over 300 years and alters the balance of radiations entering and exiting the surface of the earth. It also has significant contribution to global warming, which has long lasting, far-reaching and devastating consequence for planet earth (ATAG, 2021).

A global sector-wide action framework was agreed by international aviation transport association (IATA) in 2008 to meet the challenge of greenhouse gas emissions in the aviation industry. The framework consists of short-, medium- and long-term goals. Attainment of 1.5 % increment in the annual fleet fuel efficiency from 2008 to 2020 is the short-term goal and it has already been exceeded with a 2 % average annual increment (IATA, 2019). Carbon neutral growth (medium term goal) in the aviation industry has already started. The long-term goal is the 50 %

reduction of net CO₂ emissions by 2050 relative to 2005 (IATA, 2019). The four-pillar strategy of the international air transport association for achieving these goals are investment in new technology (including sustainable aviation fuels), better use of infrastructure, continuous operational improvements, single global market-based measure. Technology improvements via production of bio-jet fuels is the only emission-mitigation measure with the potential of achieving the long-term goal (IATA, 2019).

2.2 Sustainable aviation fuel conversion routes

Jet fuel (Aviation turbine fuel) is a mixture consisting of C₈-C₁₆ hydrocarbons that is suitable for powering aircraft. Jet fuel experts have made giant strides in the research on bio-aviation fuel conversion pathways using different feedstocks. Most of the pathways have more than one production processes. Some of the processes have gained approval in the industry. The feedstock-based conversion pathways for production of bio-jet fuel are sugar to jet, alcohol to jet, oil to jet and gas to jet.

Alcohol to jet conversion pathway is used for producing bio-jet fuel via a single route known as alcohol oligomerization. This conversion pathway involves the dehydration of methanol, ethanol or higher alcohol to produce olefins. Higher hydrocarbons are produced from the oligomerization of the synthesized olefins in the presence of catalysts. These resulting hydrocarbons are hydrogenated to produce jet fuel range hydrocarbons. Petrochemical industry uses bio-alcohols as automobile fuel component, hence the commercialization of bio-jet fuel via this conversion route may lead to feedstock competition between land and air transportation. The profitability of alcohol to jet conversion pathway is also inhibited by low yield of bio-alcohol from sugar or starch biomass. The minimum jet fuel selling price from this production pathway ranges between 3.65-10.91 USD/gallon (Wang and Tao, 2016; Doliente et al. 2020).

Sugar to jet pathway for production of jet fuel range hydrocarbons involves chemical and biochemical processes. Aqueous phase reforming and direct fermentation are the production processes for converting sugar to jet fuel. Catalytic aqueous phase reforming involves pre-treatment and conditioning of sugar followed by enzymatic hydrolysis to produce C₅ and C₆ sugars. The hydrolysate is subjected to purification and concentration before catalytic hydrogenation to produce polyhydric alcohols. Aqueous phase reforming of polyhydric alcohols occurs through acid condensation by acid or base, dehydration and oligomerization to produce bio-jet fuel. The

minimum jet fuel selling price reported for catalytic aqueous phase reforming pathway ranges between 4.66-4.75 USD/gallon (Wei et al., 2020).

Production of bio-jet fuel via direct fermentation of sugar involves pre-treatment and conditioning of sugar followed by hydrolysis in the presence of organic catalysts (enzymes) to produce hydrolysate of sugar, which are then subjected to clarification for separation of concentrated sugars. Anaerobic fermentation of the concentrated sugars gives hydrocarbon intermediates. The hydrocarbon intermediates produced are then purified and hydroprocessed to jet fuel. The minimum jet fuel selling price for direct sugar fermentation pathway is within the range of 7.17-24.42 \$/gallon (Doleinte et al., 2020).

Gas to jet conversion pathway for production of jet fuel involves the conversion of biomass-derived syngas to bio-jet fuel via Fischer-Tropsch synthesis or fermentation. Syn-gas are produced via biomass gasification. The common processes involved in bio-jet fuel production via Fischer-Tropsch synthesis are pretreatment of feedstock, gasification of biomass, conditioning of gas, removal of acid gas, Fischer-Tropsch synthesis and refining of syncrude. The pure syngas after acid gas removal is converted to hydrocarbons via Fischer-Tropsch (FT) synthesis in the presence of iron or cobalt-based catalyst. The product is then upgraded to jet fuel range hydrocarbons via hydrocracking. Jet fuel derived from Fischer Tropsch synthesis have low energy density with high cost of production. The range of minimum jet fuel selling price via Fischer Tropsch pathway is 6.23-7.57 USD/gallon (Wei et al., 2019).

In lieu of Fischer-Tropsch synthesis, biomass derived syngas is also subjected to fermentation to produce aviation turbine fuel. Cooled syngas is fermented over acetogenic bacteria for production of C₂ and C₄ alcohols. Fermentation of cooled gas can also be carried out over other microbe strains to produce isopropanol, acetate and butanol. The product of fermentation is upgraded via dehydration, oligomerization, hydrogenation and also distillation to produce bio jet fuel. Jet fuel derived from cooled syngas fermentation have slightly higher energy density as compared to Fischer Tropsch derived jet fuel. Sustainable aviation turbine fuel is produced from oils via fast pyrolysis (hydrotreated depolymerized cellulosic jet fuel), hydrothermal liquefaction (catalytic hydrothermolysis derived jet fuel) and hydroprocessing (hydroprocessed renewable jet fuel). Catalytic hydrothermolysis derived jet fuel consists of series of reactions, such as cyclization, hydrolysis, decarboxylation and cracking. Triglycerides are subjected to catalytic hydrothermolysis after catalytic conjugation and cyclization. Catalytic hydrothermolysis reactions

are carried out at a pressure of 21 MPa and reaction temperature of 450-475 °C using triglycerides and water as reactants in the presence of a catalyst to produce carboxylic acids, unsaturated organic molecules and oxygenates. Decarboxylation and hydrotreating of the products give aromatics, iso-paraffins, n-paraffins and naphthenes. Jet fuel range hydrocarbons are then sourced from the fractionation of the classes of hydrocarbons produced. The minimum jet fuel selling prices reported for the catalytic hydrothermolysis conversion route is within the range of 2.48-5.06 \$/gallon (Doliente et al., 2020). Hydrotreated depolymerized cellulosic jet fuel (HDCJ) are produced via fast pyrolysis of cellulosic biomass. The bio-oil recovered from the product of the fast pyrolysis is hydrotreated to produce hydrocarbons which are refined to jet fuel. The limitations of this technology include high consumption of hydrogen, short lifetime of catalyst and low yield of jet fuel range hydrocarbons. 5.23-7.15 \$/gallon is the range of minimum jet fuel selling price reported for this technology (Wei et al., 2020).

Hydroprocessed renewable jet fuel are produced from hydroprocessing of vegetable oils. The reactions involved in its production include hydrogenation, hydrodeoxygenation, decarboxylation, decarbonylation and hydrocracking. Unsaturated triglycerides are hydrogenated to saturated triglycerides. Saturated triglycerides are hydrogenated to produce fatty acids and propane. The fatty acids are either subjected to hydrodeoxygenation/decarboxylation/decarbonylation to yield hydrocarbons. Jet fuel range hydrocarbons (C₈-C₁₆) are produced from hydrocracking of hydrocarbons obtained. Hydroprocessed renewable jet fuel have high energy density and high thermal stability. They can be utilized directly in aviation turbine engines without blending. The minimum selling price of hydroprocessed renewable jet fuel reported in the literature is in the range of 2.36-5.74 \$/gallon. This is the lowest minimum selling price in comparison with other technologies (Doliente et al, 2020).

2.3 Hydroprocessed renewable jet fuel (HRJ)

Hydroprocessed renewable jet fuel are highly paraffinic liquids that are produced by subjecting vegetable oils to catalytic hydrogenation, hydrodeoxygenation (HDO), mild hydrocracking and hydroisomerization. Hydrodehydration, hydrodecarboxylation and hydrodecarbonylation occur simultaneously during the stage of hydrodeoxygenation (Rabaev et al., 2015).

Historically, numerous catalysts have been utilized for the hydrodeoxygenation stage. Transition metals like nickel, cobalt, molybdenum, vanadium are widely reported in literature for catalytic deoxygenation of vegetable oil (Rabaev et al., 2015; Zhang et al., 2014). Some noble metals like Palladium, Platinum and Rhenium have also been reported (Rabaev et al., 2015). To achieve high conversion of the vegetable oil to desired hydrocarbons, these catalysts are supported with metallic oxides of high surface area. The hydrocracking stages utilize a bi-functional catalyst like the transition metals and noble metals supported on a mild acidic support. The transition or noble metals perform the hydrogenation function, while the acidic support (zeolites, mesoporous or gamma alumina, silica and titania) are utilized as the cracking agent. For jet fuel production, a mild acidic support is required in order to avoid the production of lighter hydrocarbon (C₁-C₇). The hydroisomerization stage utilizes a bifunctional catalyst, which consists of active sites for hydrogenation and isomerization. Acidic catalysts with high Bronsted sites have been reported to have the potential of yielding jet fuel of high isomerization selectivity (Galadima and Muraza, 2015).

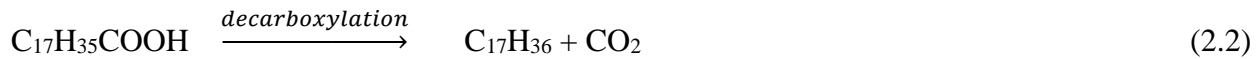
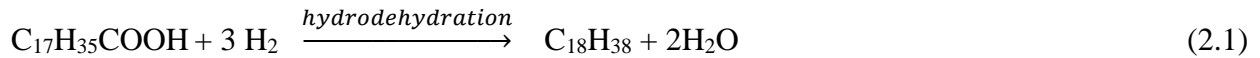
The challenges faced by the hydroprocessing catalysts over the years have been low yield of jet fuel and catalyst deactivation which can be in form of active phase sintering, coke formation, metal deposition and poisoning. The low yield of jet fuel occurs as a result of the production of light hydrocarbon in the cracking stage, or diesel range hydrocarbons production due to inadequate cracking (Rabaev et al., 2015).

Jet fuel production from fossil fuel has a serious environmental concern. The contribution of the aviation sector to the world anthropogenic emission of CO₂ is about 2-3 % annually. Bio-jet fuel has the potential of reducing greenhouse gas emissions in the aviation industry. There is a need for a life cycle assessment for proper comparison of the GHG emissions from bio-jet fuels and petroleum-derived jet fuel. This will involve considering the entire life-chain starting from the production of feedstock, change in land use, processes of conversion and emission from the combustion of jet fuel in the aviation turbine engines. The GHG emission from fuel has been reported to be 87.5 g of CO₂ per mega joule of energy obtained from jet fuel (Wang and Tao, 2016). Bio-jet fuel can offer as low as 98 % reduction of CO₂ in relation to the petroleum-derived jet fuel by emitting 1.5 g of CO₂ per mega joule of jet fuel. The magnitude and types of GHG emission is a function of types of renewable resources used and the process technologies employed

(Wang and Tao, 2016). The environmental impact involved in the production of hydroprocessed renewable jet fuel can be determined based on life cycle assessment. The assessment covers feedstock production and transportation, production and transportation of fuel and also consumption of fuel in the aircraft.

Hydroprocessed renewable jet fuel are suitable in mainstream aviation turbine engines without further engine modifications. The properties of the hydroprocessed renewable jet fuel are equivalent to that of the conventional jet fuel ((Galadima and Muraza, 2015).

The reactions involved in vegetable oil hydroprocessing technologies are hydrodeoxygenation, hydrocracking and hydroisomerization. Hydrodeoxygenation of vegetable oils can occur in form of hydrodehydration, hydrodecarboxylation or hydrodecarbonylation (Jeczminek and Porzycka-Semczuk, 2014). The sequential reaction pathways involved in the hydroprocessing of fatty acids in vegetable oils are shown in equations 2.1-2.10.



Hydrogenation and hydrodeoxygenation of vegetable oils can occur simultaneously to produce paraffins by using high hydrogen to oil ratio (Kandel et al., 2014) The reactions in equation 2.1, 2.2 and 2.3 are alternate pathways, while that of equations 2.4, 2.5 and 2.6 are also alternate pathways. Hydrocracking is required for the production of the desired jet fuel grade and hydroisomerization is required to produce jet fuel of desired cold flow properties and freezing

point (Rabeav et al; 2015, Galadima and Muraza, 2015). The challenge is to design a catalyst to favor more H₂ adsorption in order to have preference for the hydrodehydrogenation route over decarboxylation and decarbonylation.

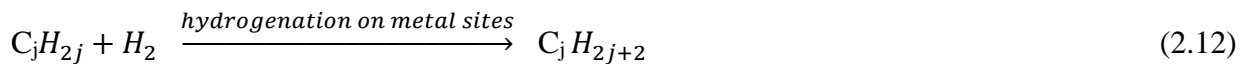
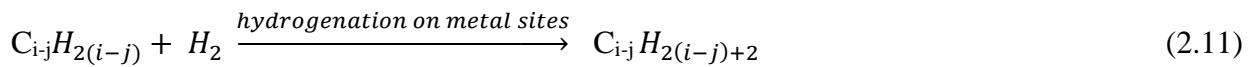
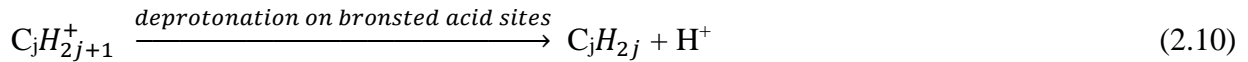
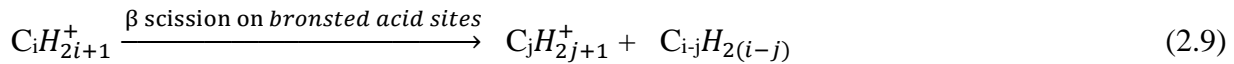
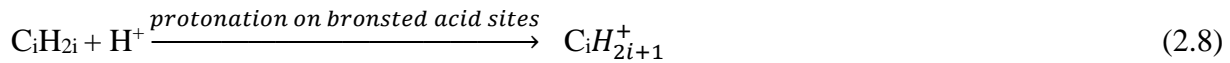
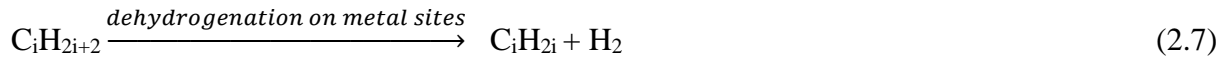
Hydroprocessing of vegetable oil starts from hydrodeoxygenation of the fatty acid and triglyceride in the vegetable oils to produce liquid hydrocarbons. Jet fuel hydrocarbon fractions (C₈-C₁₆) can be produced by subjecting the liquid hydrocarbons to mild hydrocracking. The jet fuel range hydrocarbons are then hydroisomerized to produce jet fuel of high cold flow properties, high energy density and high cetane number. These three stages have different mechanisms.

Upgrading of vegetable oil via hydrodeoxygenation is carried out by removing the oxygen content of the oil. The triglyceride content of the vegetable oil is initially transformed to three moles of fatty acids and propane via the hydrogenation of the C-O bond. Dehydration, decarboxylation and decarbonylation can occur via further hydrogenation of the fatty acids. Hydrodehydrogenation occurs through the hydrogenation of C-O bond and rupture of C=O bond without the cleavage of C-C bond. Hydrodecarboxylation and hydrodecarbonylation occur through the cleavage of C-C bond. The alkane products from hydrodehydrogenation are one carbon more than that of hydrodecarboxylation and hydrodecarbonylation. The hydrodehydrogenation route is the most desirable because it produces more isomerized products. The hydrodehydrogenation route is an exothermic reaction, while hydrodecarboxylation and hydrodecarbonylation are endothermic reactions. The hydrodehydrogenation reaction also requires more stoichiometric moles of hydrogen gas as compared to the other two reactions. Hence low temperature and high H₂/oil ratio favors dehydration. The hydrogenation of C-O can be catalyzed by the catalyst acid sites. It can also occur via the formation of adsorbed species on the surface of the catalyst. The metallic sites aid in the cleavage of adsorbed species (Muhammad et al., 2013).

Hydrocracking reaction involves the formation of free valencies due to the cleavage of C-C bond(s) in hydrocarbons. These free valencies are saturated by hydrogen. It can be carried out using bifunctional catalysts, in that case it is referred to as bifunctional hydrocracking. Monofunctional catalysts are used for the scission of the C-C bond followed by hydrogenation. The cracking is activated on the metal sites. This kind of hydrocracking is known as hydrogenolysis. Monofunctional acidic catalysts are also used for hydrocracking using Bronsted acid sites for cracking activation. It is termed as Haag-Dessau hydrocracking. The fourth case is

the thermal cracking which uses heat in the absence of catalyst. Our major focus is on the bifunctional hydrocracking which utilizes its metal sites for hydrogenation and dehydrogenation and its bronsted acidic sites for scission of the C-C bond of hydrocarbons (Jens et al., 2012).

The dehydrogenation of alkane takes place on metal sites of the bifunctional catalyst to produce alkene. Alkene diffuses to the bronsted sites of bifunctional catalyst, where it is protonated to form alkyl carbenium ions. Alkyl carbenium ions are unstable, hence they are susceptible to cracking. The protonation stage is followed by beta scission of the alkyl carbenium ions to form small chain alkene and small chain alkyl carbenium (primary alkyl carbenium ion). These ions are not stable, they can either be deprotonated or cracked further. Deprotonation leads to formation of alkenes while cracking leads to formation of small chain alkene and small chain alkyl carbenium ion. The alkenes formed diffuse to the metal sites of the bifunctional catalyst for hydrogenation to form alkanes ((Jens et al., 2012). The mechanism of cracking is depicted in equations (2.7- 2.12)



Reaction temperature and hydrogen pressure are some of the essential variables that influence the performance characteristics of the production of jet fuel through hydroprocessing (Sotelo-Boyas et al., 2011). High yield jet fuel and isomerization selectivity require optimum values of these essential operating variables (Galadima and Muraza, 2015). High conversion of vegetable oils increases with hydrodeoxygenation temperature while the selectivity to liquid

hydrocarbons increases initially with temperature and later decrease due to the production of light hydrocarbon gas produced through thermal cracking. An optimum temperature is required for high conversion and high yield of jet fuel. Kubicka et al., 2011 worked on the influence of nickel for the deoxygenation of rapeseed oil over Mo/Al₂O₃ and NiMo/Al₂O₃ catalysts at 3.5 MPa hydrogen pressure and 1 hour contact time. Over Mo/Al₂O₃ and NiMo/Al₂O₃, 61% and 93 % triglyceride conversions were obtained respectively at 260 °C; 80% and 100 % triglyceride conversions were obtained at 270 °C; and 99% and 100 % triglyceride conversion were obtained at 280 °C. The same authors worked on the deoxygenation of rapeseed oil over NiMo/Al₂O₃ catalyst at 3.5 MPa hydrogen pressure and 0.24 h contact time. 22, 57 and 74 % triglyceride conversions were obtained at 260 °C, 270 °C and 280 °C. These show that triglyceride conversion increases with temperature. The hydrocracking stage also has similar trends. For instance, Liu et al., 2013 obtained 79 % and 44 % selectivity of liquid hydrocarbons while evaluating 7 wt. % Ni/SAPO-11 catalyst for hydrodeoxygenation of palm oil at 280 and 320 °C, respectively. High lighter alkane selectivity was obtained at a temperature of 320 °C as compared to 280 °C (Galadima and Muraza, 2015).

High conversion of vegetable oils increases with hydrodeoxygenation, while the selectivity to liquid hydrocarbons increases initially with pressure and later decrease due to the production of light hydrocarbon gas which can easily be produced through thermal cracking. An optimum pressure is required for high conversion and high yield of jet fuel. The hydrocracking stage also has similar trends. For instance, alkane yields of 32% and 71% were obtained by Jeczminek et al., 2014 from the evaluation of NiMo catalysts for hydrocracking and hydrodeoxygenation of olive oil at 6 MPa and 0.3 MPa respectively.

2.4 Hydroprocessing catalysts

Researchers have utilized diverse ways to produce hydroprocessed renewable jet fuel. One of the ways is to produce jet fuel in four stages (hydrogenation, hydrodeoxygenation, mild hydrocracking and hydroisomerization). Hydrogenation and hydrodeoxygenation can be in a single stage with a single catalyst by utilizing a high hydrogen to oil ratio (Monnier et al., 2010). Hydrocracking can also be merged with the hydrodeoxygenation by using a bifunctional catalyst containing metallic sites for hydrogenation and mild acid sites for hydrocracking. Some researchers also try to merge hydroisomerization and hydrocracking in a single stage (Galadima and Muraza, 2015). In the evaluation of hydroprocessing catalysts for jet fuel production, the extent of oil conversion, the activity, and selectivity to desired jet fuel product are significantly

dependent on: 1) the kind of support; 2) the active phase; and 3) the reaction operating conditions (Galadima and Muraza, 2015).

2.4.1 Active sites

Vegetable oils are converted to paraffins in the hydrodeoxygenation process. Methanation reaction can occur as result of reaction between water and carbon oxides, hence the hydroprocessing catalysts must not be selective for such interaction. Noble metals and transition metals are generally used in the hydroprocessing of vegetable oils. Ru, Pd and Pt are among the noble metals supported catalysts evaluated for the hydrodeoxygenation of vegetable oil (Naveenji et al., 2015). Evaluation of noble metals as hydrodeoxygenation catalysts has been limited due to its high cost and preferential selectivity for hydrodecarbonylation and hydrodecarboxylation reactions over the much desired dehydration reactions (Muhammad et al., 2013). Cu, Ni, Co, Mo, W and Fe are among the transition metals used as metallic catalyst sites to produce hydroprocessed jet fuel (Rabaev et al., 2015, Galadima and Muraza, 2015). The metals can either be used as sulfided or reduced catalysts. Removal of sulfur, nitrogen and oxygen impurities in the oil is more effective with reduced catalysts as compared to sulfided catalysts (Muhammad et al., 2013). Of all the catalysts used, iron has the lowest price, highest natural abundance, and rich redox chemistry. It also has higher selectivity to the more desired dehydration reaction over the less desired decarboxylation and decarbonylation (Kandel et al., 2014). Kandel et al., 2014 carried out hydroprocessing of microalgal triglycerides over supported iron nanoparticles. The authors attributed high selectivity of liquid alkanes to the strength of Fe-O bond. The bond strength allows for sufficient reaction times for a far-reaching triglyceride reduction to paraffins. Iron is known for his high oxophilicity which is required for oxygen abstraction from triglycerides and fatty acids via hydrogenolysis of C-O and C=O bonds. Hydrodeoxygenation, hydrodecarboxylation and hydrodecarbonylation can facilitates the production of jet fuel range hydrocarbons. Olcese et al; 2013 examined hydrodeoxygenation over supported iron catalysts with different Fe loadings. The best conversion and selectivity towards the desired liquid hydrocarbons were obtained with the 10 wt. % loading of Fe. Copper has also been utilized as co-deoxygenation catalyst by different researchers. Bykoeva et al., 2012 performed hydroprocessing reaction over NiCu based catalysts and attributed high catalyst selectivity to the inclusion of Cu in the bimetallic catalyst. Copper containing catalyst are renowned for their high adsorption and activation which leads to high saturation of the active sites by adsorbates of activated hydrogen causing spillover of hydrogen to

site of the interface of catalyst support which will then facilitate induction of hydrogenolysis of C-O and C=O bonds of the fatty acids and triglycerides. The strength of adsorption and activation of Cu catalysts for hydrogen is a function of its oxidation state. Cu^{1+} has been reported to have the highest capacity for adsorption and activation of hydrogen. Similar catalysts have been utilized for mild hydrocracking of the hydrodeoxygenated products (paraffins) to produce jet fuel grade paraffins. Hydrodeoxygenation and hydrocracking are combined in a single stage by some researchers using a single catalyst (Liu et al., 2015). The challenges in the choice of catalyst for the hydrodeoxygenation are the limited yield of liquid hydrocarbon product. Limited yield of jet fuel grade paraffins is also a challenge in the choice of hydrocracking catalyst. Poor lifetime of catalyst due to deactivation is also a major problem facing hydrodeoxygenation and hydrocracking catalyst in the production of jet fuel (Vogelaar et al., 2010).

Researchers are still in search for a suitable catalyst for the hydrodeoxygenation and mild hydrocracking of vegetable oils. One of the best results obtained in the hydrodeoxygenation of oil is the evaluation of nickel-based catalyst for palm oil hydrodeoxygenation by Srifa et al., 2015. The authors obtained 100 % conversion of the palm oil feedstock and 41 % selectivity of jet fuel range hydrocarbons. Zhang et al., 2014 examined the role of nickel and cobalt in the deoxygenation of vegetable oils by comparison of the performance of unsupported NiMoS and CoMoS catalysts at 375 °C, 9 MPa hydrogen pressure and 1:20 (weight basis) catalyst/feed ratio in a batch reactor. Approximately, 2.5 wt. % and 1.7 wt. % $\text{C}_1\text{-C}_6$ hydrocarbons selectivities were obtained over CoMoS and NiMoS catalysts, respectively. This points to the fact that the undesired $\text{C}_1\text{-C}_6$ hydrocarbons in jet fuel are less favored with nickel catalyst. This shows that nickel containing catalyst has more selectivity for hydrodehydrogenation as compared to the cobalt containing catalyst. The product obtained from the evaluation of nickel containing catalyst will have better cold flow properties than the cobalt containing catalyst. The catalyst activity of the NiMoS and CoMoS was also compared on the basis of the conversion of triglyceride. About 99 % and 93 % triglyceride conversion was obtained over the nickel and cobalt catalysts respectively, at a common hydrotreating time of 2 hours. This shows that the nickel catalyst is more active for hydrodeoxygenation as compared to the cobalt catalyst. Paraffins are the main desired product of hydrodeoxygenation, 65 % and 95 % paraffin selectivities were obtained, respectively, over the cobalt and nickel catalysts at 8 hours hydrotreating time. Kubicka et al., 2011 worked on the influence of nickel for the deoxygenation of rapeseed oil over unsulfided $\text{Mo}/\text{Al}_2\text{O}_3$ and

NiMo/Al₂O₃ catalysts at 3.5 MPa hydrogen pressure. About 61% and 93 % triglyceride conversions were obtained over unsulfided Mo/Al₂O₃ and NiMo/Al₂O₃ catalysts respectively at 260 °C. Approximately, 80% and 100 % hydrocarbon selectivities were obtained over unsulfided Mo/Al₂O₃ and NiMo/Al₂O₃ catalysts, respectively, at 280 °C. This shows the influence of nickel in improving the HDO catalyst selectivity towards hydrocarbons.

Sn, Ti and Zr have oxophilic properties desirable for abstraction of oxygen from triglycerides and fatty acids via hydrogenolysis of C-O and C=O. The textural properties of Copper based catalysts can be promoted by Sn, Ti and Zr. Apart from the oxophilic properties of Sn, it also has effect on the cracking of triglycerides/fatty acids. For production of jet fuel range hydrocarbons, mild hydrocracking is required. Excessive cracking will lead to production of lighter hydrocarbons below the hydrocarbon range of jet fuel. Little or no cracking will result in the production of C₁₇ and C₁₈ hydrocarbons, which are more than the range of jet fuel hydrocarbons. The use of Sn to promote Cu based catalysts for production of jet fuel range hydrocarbons will require optimum Sn loading which will be maximize hydrogenolysis of C=O and C-O based on his oxygen abstraction ability. Excessive loading of Sn can result in severe cracking. The desired mild cracking can be achieved by avoiding excess Sn loading. Different loadings of Fe in a copper-based catalyst have been proven to have effect on catalyst dispersion (Lup et al., 2018).

2.4.2 Supports

The supports utilized in the hydroprocessing of triglycerides need to complement the activity role played by the active site phase of the catalyst. This can be accomplished by developing catalysts' support of high pore volume and specific surface area. Production of light hydrocarbons can be prevented with the use of support of mild acidity (Rabaev et al., 2015). Silico-alumino phosphates, alumina, zirconium oxide and zeolites have been developed by researchers for this purpose (Deepak et al., 2011; Verma et al., 2015; Saadi and Stuart, 1991). Kazuhisa et al., 2010 carried out hydrodeoxygenation of jatropha oil feedstock over a catalyst supported on ZSM-5 (23 wt. % silica-alumina ratio) in a 0.1 litre at 6.5 MPa H₂ pressure, 300 °C reaction temperature, 1 g catalyst/g oil ratio and 12 h reaction time. 83.8 % conversion of jatropha oil, 96.0 % selectivity of hydrocarbons within the range of C₁₀-C₂₀ was obtained. This shows that ZSM 5 zeolite is selective towards the production of liquid hydrocarbons. The low selectivity towards carbon oxides shows

that the catalyst has higher selectivity for deoxygenation over decarboxylation and decarbonylation. Rogelito et al., 2011 worked on hydrodeoxygenation of rapeseed oil over Pt/ZSM-5 catalyst in 80 cm³ batch reactor at 380 °C, 11 MPa hydrogen pressure, 3 g catalyst/g oil ratio and 3 h reaction time. 68 % yield of liquid hydrocarbons (C₅₊) and 13 % C₁-C₄ hydrocarbon yield were obtained. 1 % and 5.8 % respective yields of CO and CO₂ were obtained under these operating conditions. The breakdown of the 68 % yield of liquid hydrocarbon produced includes 43 % yield of C₅-C₁₂, 20 % yield of C₁₃-C₂₂ and 5 % yield of C₂₃₊. The high yield of C₅-C₁₂ shows the cracking effect of the ZSM-5 catalyst, thus indicating that it can also be suitable for the hydroprocessing of vegetable oils for production of jet fuel range hydrocarbons.

MgO support has also been used as component of bifunctional catalyst in the hydroprocessing of oil. Yun et al., 2009 performed hydrodeoxygenation of oil using a catalyst supported by MgO at 350 °C and 5 MPa H₂ pressure for 60 mins. The thermogravimetric analysis of the spent catalyst, which was heated to 900 °C from ambient temperature at 10 K/min in a 30 cm³/min air flow rate, shows that the loss of weight within the range of 250 °C and 600 °C can be ascribed to coke combustion and deposition on the surface of the catalyst. The amount of coke deposition was calculated to be approximately 8 % which depicts that the MgO containing catalyst has strong resistance to coke deposition. This was attributed to the basic character of MgO. Tarit et al., 2014 studied deoxygenation over a catalyst supported on MgO at 6.9 MPa H₂ pressure and 200 °C in a high pressure plug flow reactor. Catalyst deactivation studies were carried out by performing repetitive experiments consecutively. It was observed that after the second experimental run, feed conversion stabilizes, which shows that catalyst stability is desirable. The high catalyst stability can be attributed to the basic character of the MgO used in supporting the catalyst. MgO as a basic support has a strength of catalyst stability and weakness of lacking the mild cracking strength required for production of jet fuel range hydrocarbons.

SiO₂, Al₂O₃ and their combination have also been used for hydroprocessing of triglycerides. Yanyong et al., 2011 examined the hydroprocessing of vegetable oils over NiMo catalysts supported on silica, alumina and mixed support of silica and alumina at 350 °C and 4 MPa H₂ pressure. The catalysts supported on the mixture of silica and alumina gave the highest selectivity towards jet fuel range hydrocarbons. Calemma et al., 2000 worked on the hydrocracking of n-hexadecane over Pt/ SiO₂-Al₂O₃ catalyst. 96 % jet fuel range hydrocarbons selectivity was obtained at 360 °C, 8.1 MPa H₂ pressure, 32 h reaction time and catalyst/oil ratio of 4.94 g

catalyst/g oil. 37 % selectivity of cracking products (C₁-C₇ hydrocarbons) was obtained at these conditions. This shows that SiO₂-Al₂O₃ has the required bronsted acidity that can break the C-C bond in alkyl carbenium ion from the protonation of alkene that will result from the dehydrogenation of alkane. It can also subject the alkyl carbenium ion to skeletal rearrangement. This shows the cracking and selectivity of SiO₂-Al₂O₃ and makes it desirable for jet fuel production. Shaofeng et al., 2012 performed the hydroprocessing of jatropha oil over NiMo/SiO₂-Al₂O₃ and NiMo/ZSM-5-Al₂O₃ catalyst at 370 °C and 3 MPa H₂ pressure in a fixed bed flow reactor. Higher selectivity of jet range hydrocarbons selectivity were obtained from the evaluation NiMo/SiO₂-Al₂O₃.

Bie et al., 2013 evaluated noble metal catalysts using zirconia support for hydrodeoxygenation to obtain 91.9 % liquid alkane selectivity at 340 °C and 8 MPa. Kubicka et al., 2011 carried out the deoxygenation of rapeseed oil over catalysts using Al₂O₃ support to obtain 100% conversion and 100 % liquid alkane selectivity at 270 °C and 3.5 MPa. Hydrocracking catalyst support choice is more critical, since isomerization process follows hydrocracking. Catalyst with moderate acidity is required for the mild hydrocracking process. USY, HY, SAPO-11, HZSM, ZSM support materials have been used for evaluation for this purpose. Rabaev et al., 2015 worked on the hydrocracking of diesel hydrocarbon fractions over Ni₂P/HY catalyst at 315 °C and 3.04 MPa to obtain 100 % feed conversion and 48 % yield of jet graded paraffins. The formation of a secondary alkylcarbenium, rearrangement of alkyl carbenium ion and deprotonation in hydroisomerization requires catalyst supports with effective bronsted acid sites for protonation of olefins (Galadima and Muraza, 2015). An ideal mild hydrocracking catalyst should give a high yield of jet fuel range hydrocarbons Medium pore size, mild acidity levels and acidity strength, high metal dispersion are needed to achieve these characteristics. Hydrocracking of paraffins has been carried out over SAPO-11, Al₂O₃, zeolites, MCM-41 and AlMCM-41. Huang et al 2003 performed hydrocracking over Pd catalyst supported on SAPO-11. The SAPO-11 was synthesized in butanol-CTAB-H₂O system. 42 % selectivity to the desired jet fuel range hydrocarbons was obtained. Similar experiment was performed by Liu et al., 2004 using SAPO-11 support at 360 °C and 4 MPa to obtain 83 % conversion and 54.3 % jet fuel range hydrocarbon selectivity.

2.5 Feedstocks for hydroprocessed Renewable jet fuel

Production of bio-jet fuels using different renewable resources such as halophytes, camelina, algae, waste oil and jatropha is presently being researched. The vegetable oils used as

feedstocks for bio-jet fuel include rapeseed, soybean, cottonseed, palm, sunflower, peanut, camelina, jatropha and microalgal oils. These feedstocks are better than the feedstocks used for crude oil based conventional jet fuel due to their renewability, sustainability and environmental friendliness. Non-edible oils are preferred for bio-jet fuel production in order to avert the food-fuel crisis caused by the use of edible oils for biofuels. The lowest priced bio-jet fuel feedstocks are the abundant non-edible oils including used cooking oil, which are obtained through the accumulation of oil from bakeries, hotels and restaurants (Mohammad et al., 2013). Table 2.1 shows the global production capacity of edible and non-edible oils, oil yield per hectare of land and also the percentage composition of oil from its seed. Palm oil has the highest global capacity and oil yield per hectare out of all the edible oils. The algal oil (schizochytrium species) has the highest oil yield per hectare.

2.6 Kinetics and thermodynamics of hydroprocessing of vegetable oils

Kinetic modelling of reactions is carried out by proposing reaction pathways or network. Reaction mechanism can be formulated from these pathways. Kinetic model is proposed based on the proposed reaction network. Kinetic models are fitted with experimental data using least square regression. Correlation coefficient values and residual properties are used in determining fitting strength of experimental data with the model. Some kinetic parameters are determined after ensuring the fitness of the data with the experiment. These parameters can be activation energy and kinetic rate constant of the reaction. The value of the activation energy is the minimum energy required for reaction to take place. Activation energy of reactions is lowered by catalysts. The kinetic rate constant is the ratio of the rate of reaction and the concentration of the reactants. The concentration of the reactants will have an exponent based on the order of the reaction. Kinetic rate constant of reaction could increase with the use of catalyst. Hydroprocessing reactions of vegetable oils consist of hydrodeoxygenation, hydrocracking and hydroisomerization stages. Hydrodeoxygenation of vegetable oils (triglycerides and fatty acids) is accompanied with hydrodehydration, hydrodecarboxylation and hydrodecarbonylation. There could be some other side reactions. Among them are the water gas shift reaction, which can occur as a result of reaction of water and carbon (II) oxide produced from decarbonylation. The carbon (II) oxide from decarbonylation and carbon (IV) oxide from decarboxylation can also react with hydrogen to produce methane. The water gas shift and methanation reactions are undesirable. In the hydrodeoxygenation of vegetable oil, there could be cracking which could result in the production

of the undesired low chain hydrocarbons (C₁-C₄). There is also possibility of oligomerization to produce wax. All these are undesired reactions. Kinetic modelling of the hydroprocessing reaction gives the activation energy and kinetic rate constants of the desired and undesired reactions. Kinetic parameters of hydroprocessing of vegetable oils/ fatty acids over heterogeneous catalysts have been evaluated by different researchers (Kumar et al. 2013; Ayodele et al. 2015; Anand et al. 2016). Anand et al (2016) evaluated the activation energy of hydroprocessing of jatropha oil over Ni-W/SiO₂-Al₂O₃ catalyst and concluded that 115kJ/mol is the minimum energy required for the reaction. Ayodele et al (2015) and Kumar et al (2013) obtained activation energies of 130.3kJ/mol and 175.4kJ/mol from the hydroprocessing of oleic acid and stearic acid over FMOx/zeolite and Ni/Al₂O₃ catalyst, respectively.

2.7 Technoeconomic analysis

The commercial viability of bio-jet fuels strongly depends on the production cost. Process design, efficiency of feedstock conversion, feedstocks cost and composition, market value of byproducts and conservation of energy have significant effect on the production cost of bio-jet fuel. The cost of petroleum-derived jet fuel has been faced by large fluctuations. Based on the annual global consumption of 2.3 billion barrels of jet fuel stated earlier, a penny increase per barrel will result in \$23 million increase in annual fuel cost. The cost of production of bio-jet fuel is estimated to decrease significantly in the nearest future because of the improvement in process technology (Wang et al., 2016). Bio-jet fuel will occupy three-tenths of the annual global consumption of jet fuel due to this predicted decrease. There is a need for significant improvements in the minimization of cost of raw materials and energy in order to achieve the said decrease in the cost of production of bio-jet fuel (Wang et al., 2016).

Table 2.1: Global availability of vegetable oils (Balat et al., 2011; USDA, 2015)

Vegetable oils	Types	Global production capacity (million metric tons/yr)	Oil yield (kg oil/ha)	Oil yield from seed (%)
Palm oil	Edible	62.44	5000	20
Soybean	Edible	47.37	600	20
Sunflower	Edible	15.16	600	22-36
Peanut	Edible	5.52	1059	-
Cottonseed	Edible	5.13	325	-
Coconut oil	Edible	3.43	1400	-
Olive oil	Edible	2.34	1212	-
Rapeseed oil	Edible	26.98	1190	-
Canola oil	edible	2.56	1400	44
Jatropha oil	Non-edible		1590	35-40
Castor oil	Non-edible	1.5	1188	53
Algal oil (schizochytrium species)	Non-edible		92000	50-77
Used cooking oil	Non-edible	16.5	-	-

CHAPTER 3

Experimental Section

Contribution of this chapter to overall study

This chapter describes the catalysts' synthesis, characterization and evaluation for hydroprocessing of oleic acid for production of jet fuel range hydrocarbons

3.1 Catalysis Synthesis

Reduced Cu/SiO₂-Al₂O₃, FeCu/SiO₂-Al₂O₃, FeCu/ZSM-5 and FeCu/HZSM-5 bimetallic catalysts were synthesized using diffusional impregnation and co-impregnation techniques.

3.1.1 Chemical and Materials

Oleic acid (code number: 364525) and amorphous silica–alumina catalyst support (SiO₂/Al₂O₃: 6.25, code number: 343358) were procured from Sigma-Aldrich (Missouri, U.S.A). Copper (II) nitrate hemipentahydrate (code number: 467855) and iron nitrate nonahydrate (code number: 254223) were purchased from ES company (New Jersey, U.S.A) and Millipore (Canada) Ltd (Ontario, Canada) respectively. ZSM-5 zeolite (code number: CB2314, SiO₂/Al₂O₃: 23) was supplied by zeolyst international (Kansas, U.S.A).

3.1.2 Support Preparation

HZSM -5 support (SiO₂/Al₂O₃: 23) was prepared by exchanging ZSM-5 with a 1.0 M ammonium nitrate solution at 100 °C for 3 h followed by calcination in air at 550 °C for 4 h. Two commercial supports (amorphous silica alumina and ZSM-5) were used alongside the synthesized HZSM-5.

3.1.3 Catalyst Preparation by Impregnation

Monometallic 5, 10, 13 and 15 wt% Cu/SiO₂-Al₂O₃ catalysts were synthesized using copper (II) nitrate hemipentahydrate as precursor for copper. The solution of the precursor was impregnated on amorphous silica alumina using diffusional impregnation technique and then the mixture was dried overnight at 100 °C in a drying oven for each of the four catalyst samples. For instance, 15 g of 13 wt% Cu/SiO₂-Al₂O₃ was synthesized by impregnating 7.1 g of copper (II) nitrate hemipentahydrate, dissolved in 50 ml of water and the resulting solution was impregnated on 13.1 g of amorphous silica alumina. The dried mixture was calcined in air in a muffle furnace at 450 °C for 6 hours at 1 °C /min heating rate, reduced under 50 mL/min H₂ flow at 400 °C for 4 hours at 1 °C/min heating rate and passivated with 1% O₂/N₂ flowing at 50 mL/min for 1 hour

ambient temperature. Thirteen wt% Cu/SiO₂-Al₂O₃ was selected from the four catalyst samples for iron promotional effect studies.

Bimetallic Fe(1)-Cu(13)/SiO₂-Al₂O₃, Fe(2)-Cu(13)/SiO₂-Al₂O₃, Fe(3)-Cu(13)/SiO₂-Al₂O₃, Fe(5)-Cu(13)/SiO₂-Al₂O₃ catalysts were synthesized using copper (II) nitrate hemipentahydrate and iron nitrate nonahydrate as precursors for copper and iron respectively. Copper (II) nitrate hemipentahydrate solution and iron nitrate nonahydrate solution was first impregnated on amorphous silica alumina using diffusional co-impregnation method and then the mixture was dried overnight at 100 °C. For instance, 15 g of Fe(3)-Cu(13)/SiO₂-Al₂O₃ was synthesized by co-impregnating 7.1 g of copper (II) nitrate hemipentahydrate and 3.3 g of iron nitrate nonahydrate solution on 12.6 g of amorphous silica alumina. The dried co-impregnated mixture was calcined in air in a muffle furnace at 450 °C for 6 hours by heating at 1 °C/min, reduced under 50 mL/min H₂ flow at 400 °C for 4 hours at 1 °C/min heating rate and passivated with 1% O₂/N₂ flowing at 50 mL/min for 1 hour ambient temperature. Fe(3)-Cu(13)/SiO₂-Al₂O₃ catalyst was selected as the catalyst from the four bimetallic catalysts for supports optimization studies.

For effective support optimization, Fe(3)-Cu(13)/ZSM-5 and Fe(3)-Cu(13)/HZSM-5 catalysts were also synthesized using the same procedure as Fe(3)-Cu(13)/SiO₂-Al₂O₃ catalyst.

3.2 Catalyst Characterization

3.2.1 Inductively Coupled Plasma-Optical Emission Spectrometry (ICP-OES) analysis

The mass compositions of copper and iron in Fe(3)-Cu(13)/SiO₂-Al₂O₃, Fe(3)-Cu(13)/ZSM-5 and Fe(3)-Cu(13)/HZSM-5 catalysts were evaluated using a concentrated mixture of HF/HNO₃/HClO₃ to digest 0.125 g of each catalyst samples to dryness in a Teflon tube to analyze copper and also utilizing Ox automated fusion instrument to fuse the combination of Lithium metaborate and Lithium tetraborate mixture with 0.1 g of each catalyst samples in a graphite crucible to analyze iron. Dilute HNO₃ was then used to dissolve the dry residue and fused product obtained respectively from the copper and iron analyses and they were analyzed with Perkin Elmer ICP-OES (Optima 5300 DV) in the geoanalytical laboratory of the Saskatchewan Research Council.

3.2.2 N₂-Adsorption/Desorption Measurement

Micrometrics ASAP 2020 instrument was used to characterize all the fresh and spent catalyst samples and their respective supports with the Brunauer-Emmett-Teller (BET) method. Each catalyst sample was degassed in a sealed tube in vacuum conditions at 250 °C for 5 h and

evacuated until a static pressure of less than 1.33 Pa was obtained. Physisorption analysis was then carried out with N₂ at -196 °C.

3.2.3 X-ray Diffraction (XRD)

X-ray diffraction patterns of all the catalyst samples and their respective supports were obtained with a monochromatic Cu K α radiation source of 0.15406 nm wavelength using an Ultima IV instrument from Rigaku Instruments. The normal scan rate of the equipment is 2° scan/min within 10–80° diffraction angle and 0.02 step size. The average crystallite size of the intense XRD peaks obtained for all the catalyst samples was calculated using Equation 3.1, which is accurate for crystallite size of 3-80 nm (Scott, 2021).

$$L = \frac{k\lambda}{\beta\cos\theta} \quad (3.1)$$

Where Scherrer constant, $k = 0.94$ for spherical crystallites with cubic symmetry; wavelength of the source of X-ray, $\lambda = 1.54$ angstrom; β = Full width at half maxima; and θ = half of the Bragg angle (Scott, 2021).

3.2.4 FTIR Spectroscopy.

A JASCO FT-IR 4100 instrument was used to identify the functional groups of the all the synthesized catalyst samples and their respective supports. For analysis, 3 mg of sample was uniformly mixed with 0.4 g of KBr pellets. Qualitative analysis of the functional groups of the catalyst samples was obtained with 32 scans of 4 cm⁻¹ nominal resolution. The IR spectra of pelletized samples were later recorded in transmission mode within 400–1400 cm⁻¹ wavenumber.

3.2.5 X-ray Photoelectron Spectroscopy (XPS)

XPS was used to study the phases of the active sites (Copper and Iron) at the surface of Fe(3)-Cu(13)/SiO₂-Al₂O₃, Fe(3)-Cu(13)/ZSM-5 and Fe(3)-Cu(13)/HZSM-5 catalyst samples. Kratos (Manchester city, United Kingdom) AXIS Supra system equipped Rowland circle monochromated source of 1486.6 eV Al K- α was used for X-ray photoelectron spectroscopy (XPS) measurements for all three synthesized catalyst samples. Three high-resolution regional scans were carried out using 0.05 eV steps with 20 eV pass energy. An accelerating voltage of 15,000 eV and an emission current of 0.015 A were used for the analysis.

3.2.6 H₂-TPR Analysis

H₂-TPR of Fe(3)-Cu(13)/SiO₂-Al₂O₃, Fe(3)-Cu(13)/ZSM-5 and Fe(3)-Cu(13)/HZSM-5 catalyst samples were conducted at 101.3 KPa using Micrometrics Auto Chem II 2920 analyzer.

10% H₂/Ar was circulated to 0.05 g of each sample in a steel tube at 50 cm³/min and the temperature was increased to 850 °C from ambient temperature at 10 °C/min. As the temperature increases, the reaction of the catalyst and hydrogen gas proceeds to produce water vapour, which was trapped through a cold trap by outlet stream circulation. The exit gas stream was channeled via a calibrated thermal conductivity detector (TCD) for the detection of varying H₂ concentrations due to catalyst reduction.

3.2.7 Pyridine FTIR

The FTIR technique was utilized to study the nature of acid sites of Fe(3)-Cu(13)/SiO₂-Al₂O₃, Fe(3)-Cu(13)/ZSM-5 and Fe(3)-Cu(13)/HZSM-5 catalyst samples and their respective supports using a wavenumber region of pyridine (1400–1700 cm⁻¹). A sample cylindrical cup in a Spectrotech diffuse reflectance in situ cell equipped with a thermocouple and zinc selenide windows was loaded with 0.01 g of each catalyst sample. These three catalyst samples and their respective supports were pretreated at 350 °C in order to remove any adsorbed water on the catalyst surface. Pyridine vapor was then passed over each catalyst sample at 100 °C for 1 hour to obtain pyridine chemisorbed samples. After adsorption of pyridine, nitrogen gas was used for the stabilization of the catalyst samples at 100 °C for 30 min with a ramping rate of 5 °C/min, then allowed to cool to ambient temperature. The samples were analyzed with a JASCO FT-IR 4100 instrument in the wavenumber range of 1400–1700 cm⁻¹ and their respective IR spectra were recorded. Brønsted/Lewis acid sites ratio of all the three catalyst samples were calculated using Equation (3.2):

$$\frac{C_B}{C_L} = \frac{\text{IMEC(B)}^{-1} \cdot \text{IT(B)}}{\text{IMEC(L)}^{-1} \cdot \text{IT(L)}} \quad (3.2)$$

Where, $\frac{C_B}{C_L}$ = ratio of concentration of Bronsted and Lewis acid sites. IMEC(B) and IMEC(L) are integrated molar extinction coefficients (cm/μmol) of Brønsted and Lewis acid sites, respectively. IT(B) and IT(L) are integrated transmittances of Brønsted and Lewis acid sites, respectively (Platon et al. 2003; Li et al. 2012).

3.2.7 CO Chemisorption

The metal dispersion and crystallite size of Fe(3)-Cu(13)/SiO₂-Al₂O₃, Fe(3)-Cu(13)/ZSM-5 and Fe(3)-Cu(13)/HZSM-5 catalyst samples were measured using the Micrometrics ASAP 2020 chemisorption system. The catalyst samples were heated to 350 °C at 10 °C/min ramp rate in the

presence of H₂. They were then held for 2 h and later cooled down to 35 °C and evaluated to a static pressure below 1.3×10^{-5} N/m². Pulses of CO were passed over the evacuated sample and the total CO uptake was measured at 35 °C. Stoichiometric factor of 0.5 mole of CO per metal atom was used for copper and iron.

3.3 Catalyst Evaluation

The catalytic reactions were carried out in a Parr stirred batch reactor. The temperature calibration of the reactor is depicted in Figure A.1. It is made in a bench top with moveable vessel mounting style. The capacity of the reactor vessel is 300 mL, with dimension of 2.5 inches diameter and 4 inches depth and the reactor is connected to a Parr 4848 reactor controller. The catalyst samples were evaluated in this Parr batch reactor. Two g of each of the catalyst samples and 40 g of oleic acid were placed in the reactor and hydrogen gas was used to pressurize the reactor to 2.07 MPa. Cu/SiO₂-Al₂O₃ and FeCu/SiO₂-Al₂O₃ catalysts were evaluated at 340 °C. The temperatures of the reaction involving support optimization studies were set at 300, 320 and 340 °C. The impeller speed and reaction time were 500 rpm and 10 h, respectively.

3.4 Product Analysis

The liquid product samples were collected at 2 h interval, filtered and diluted using chloroform as the diluent. The solution of liquid product samples was analyzed with GC (Agilent 7890A) equipped with a flame ionization detector (FID). A 30 m long DB-5 capillary column with 0.25 mm inner diameter was used. The temperature of the oven was programmed to start from 40 °C for 2 min and increased to 280 °C at 10 °C/min ramping rate with a 5 min final hold time. One μL of each product sample was injected with a split ratio of 10:1 into the column. C₆–C₂₀ aliphatic hydrocarbons were used as external standard to quantify the liquid hydrocarbons produced. The GC calibration of the liquid product is depicted in Figure A.2. The gaseous products were analyzed using an online GC equipped with FID and catalyst performance was evaluated based on oleic acid conversion and jet-fuel range hydrocarbons (C₈–C₁₆) selectivity as given below.

$$\text{Oleic acid conversion (\%)} = \left(\frac{\text{amount of oleic acid reacted}}{\text{amount of oleic acid initially taken}} \right) \times 100 \quad (3.3)$$

$$\begin{aligned} \text{Selectivity of jet – fuel range hydrocarbons (\%)} = \\ \left(\frac{\text{amount of jet–fuel range hydrocarbons}}{\text{amount of products formed}} \right) \times 100 \end{aligned} \quad (3.4)$$

Yield of jet – fuel range hydrocarbons (%) =

$$\left(\frac{\text{amount of jet-fuel range hydrocarbons}}{\text{amount of oleic acid initially taken}} \right) \times 100 \quad (3.5)$$

CHAPTER 4

Hydroprocessing of Oleic Acid for Production of Jet-Fuel Range Hydrocarbons over Cu and FeCu Catalysts

The content of this chapter has been published in catalyst journal and presented in the following conferences as cited below:

Citation:

Ayandiran AA, Boahene PE, Dalai AK, Hu Y. Hydroprocessing of oleic acid for production of jet-fuel range hydrocarbons over Cu and FeCu catalysts. *Catalysts*. 2019;9(12).

doi:10.3390/catal9121051

Conference Proceedings:

- Afees A. Ayandiran., Ajay. K. Dalai, “Novel Catalysts Development for production of Jet Fuel Range Hydrocarbons from Vegetable Oil: A review. Poster presentation at 67th Canadian Chemical Engineering Conference, Edmonton, Alberta, Canada, October 22-25, 2017.
- Afees A. Ayandiran, Ajay. K. Dalai “Hydroprocessing of oleic acid for production of jet fuel range hydrocarbons over FeCu catalysts. Poster presentation at 25th Canadian Symposium on Catalysis, Saskatoon, Saskatchewan, Canada, May 8 -11th , 2019.
- Afees A. Ayandiran, Ajay. K. Dalai, “Hydroprocessing of oleic acid for production of jet fuel range hydrocarbons over FeCu catalysts” . Oral presentation at 68th Canadian Chemical Engineering Conference, Toronto, Ontario, Canada, October 28-31, 2018.

Contribution of the Ph.D. Candidate

Synthesis, characterization and evaluation of catalyst were planned and executed by Afees A. Ayandiran in due consultation with Dr. Ajay K. Dalai and Dr. Yongfeng Hu. The manuscript was prepared and reviewed by Afees A. Ayandiran based on the guidance and suggestions provided by Dr. Ajay K. Dalai and Dr. Yongfeng Hu. Dr. Boahene Philip also assisted in reviewing the paper.

Contribution of this chapter to the overall PhD work

This chapter investigates the optimum loading of the combination of Cu and Fe required as bimetallic catalyst for hydroprocessing of oleic acid for production of jet fuel range hydrocarbons. It also investigates the required support to boost catalyst performance. The investigations

demonstrate the physicochemical characteristics of FeCu catalysts and their effect on the catalytic activity for production of jet fuel range hydrocarbons

4.1 Abstract

In the present study, a series of monometallic Cu/SiO₂-Al₂O₃ catalysts exhibited immense potential in the hydroprocessing of oleic acid to produce jet-fuel range hydrocarbons. The synergistic effect of Fe on the monometallic Cu/SiO₂-Al₂O₃ catalysts of variable Cu loadings (5–15 wt%) was ascertained by varying Fe contents in the range of 1–5 wt% on the optimized 13% Cu/SiO₂-Al₂O₃ catalyst. At 340 °C and 2.07 MPa H₂ pressure, the jet-fuel range hydrocarbons yield and selectivities of 51.8% and 53.8%, respectively, were recorded for the Fe(3)-Cu(13)/SiO₂-Al₂O₃ catalyst. To investigate the influence of acidity of support on the cracking of oleic acid, ZSM-5 (Zeolite Socony Mobil-5) and HZSM-5(Protonated Zeolite Socony Mobil-5)-supported 3% Fe-13% Cu were also evaluated at 300–340 °C and 2.07 MPa H₂ pressure. Extensive techniques including N₂ sorption analysis, pyridine- Fourier Transform Infrared Spectroscopy (Pyridine-FTIR), X-ray Diffraction (XRD), X-ray Photoelectron Spectroscopy (XPS), and H₂-Temperature Programmed Reduction (H₂-TPR) analyses were used to characterize the materials. XPS analysis revealed the existence of Cu¹⁺ phase in the Fe(3)-Cu(13)/SiO₂-Al₂O₃ catalyst, while Cu metal was predominant in both the ZSM-5 and HZSM-5-supported FeCu catalysts. The lowest crystallite size of Fe(3)-Cu(13)/SiO₂-Al₂O₃ was confirmed by XRD, indicating high metal dispersion and corroborated by the weakest metal–support interaction revealed from the TPR profile of this catalyst. CO chemisorption also confirmed high metal dispersion (8.4%) for the Fe(3)-Cu(13)/SiO₂-Al₂O₃ catalyst. The lowest and mildest Brønsted/Lewis acid sites ratio was recorded from the pyridine–FTIR analysis for this catalyst. The highest jet-fuel range hydrocarbons yield of 59.5% and 73.6% selectivity were recorded for the Fe(3)-Cu(13)/SiO₂-Al₂O₃ catalyst evaluated at 300 °C and 2.07 MPa H₂ pressure, which can be attributed to its desirable textural properties, high oxophilic iron content, high metal dispersion and mild Brønsted acid sites present in this catalyst.

4.2 Introduction

The aviation sector is a large growing sector which bridges large distances within relatively short time. The total number of international air passengers worldwide in 2018 was 4.4 billion, and this is expected to increase to 7.8 billion in 2036 with Compound Annual Growth Rate (CAGR) of 3.6% according to the prediction made by the International Air Transport Association

(IATA). The aviation sector facilitates 35% of world trade by value and it is responsible for transporting 54% of international tourists. In spite of the significance of this sector, it is being faced by challenges over the years. The worldwide aviation industry consumes about 1.7 billion barrels of conventional jet fuel annually (Wang et al., 2016). The development of the aviation industry is paralleled with increase in greenhouse gas emissions (Kieckhafer et al., 2018). According to the air transport action group (ATAG), 895 million tonnes of CO₂ was emitted by flights in 2018, which represents about 2% of human-induced emissions. As a result, aviation experts unanimously agreed on three targets that are carbon neutral growth by 2020, fifty percent greenhouse gas emission reduction by 2050 with respect to 2005 as a baseline and lastly, improvement of efficiency of fuel by 1.5% from 2009 to 2020. These are the first set of climate change targets that are streamlined to a particular sector in the world (Bwapa et al., 2017). In order to achieve these targets, different carbon footprint mitigation strategies were devised. They are technological improvements, use of aviation biofuels, airline operations improvements and market-based measures. Sgouridis et al (2011) used the Global Aviation Dynamics (GAID) model to prove that the potential contribution of aviation biofuels and market-based measures is significantly higher than the contribution of the other strategies.

Biochemical and thermochemical processes are among the technologies utilized for production of jet fuel from these biomass-based materials (Wang et al., 2016). The alternative fuels for air transport include hydroprocessed renewable jet fuels (HRJ), Fischer–Tropsch jet fuels (FTJ), liquid biohydrogen, biomethane and bioalcohol (Wang et al., 2016). Hydroprocessed renewable jet fuel has been proven to have the highest jet fuel-to-feed ratio, highest overall energy efficiency, lowest total capital investment and the lowest jet-fuel selling price (Diederichs et al., 2016). Hydroprocessed renewable jet fuels are produced from oil-based feedstocks using hydroprocessing technologies that encompass hydrotreating, hydrodeoxygenation, hydrocracking and isomerization reactions. They find application in conventional aviation turbine engines without modification and without blending with conventional petroleum-derived jet fuels. Hydroprocessed jet fuels are suitable for high altitude flights due to their high cold flow properties (Wang et al., 2016).

Copper-based catalysts are well known for their preferential selectivity for hydrogenation of C=O bond in carbonyl compounds due to the presence of the unfilled 3D electron levels of metallic copper. These catalysts are also known for their high H₂ adsorption and activation abilities

(Bykova et al., 2012). Bykova et al (2012) carried out hydrodeoxygenation over a reduced NiCu bimetallic supported catalysts and reported that high catalyst selectivity and catalyst stability were obtained as a result of the inclusion of Cu in the bimetallic catalyst. In spite of all the advantages of using a copper-based catalyst for the hydroprocessing of vegetable oils, they have low affinities for oxygen. To develop a novel catalyst with higher catalyst activity and selectivity, bimetallic catalysts are used due to their often appreciable chemical and electronic behavior as compared to their corresponding monometallic catalysts. Iron has high oxophilicity and can be used to tune the activity and selectivity of copper. Iron has the highest natural abundance, lowest price and rich redox chemistry (Kandel et al., 2014). Kandel et al (2014) performed hydrodeoxygenation of microalgal oil over the reduced iron-based catalyst. It was found that the high selectivity towards liquid alkanes was due to the Fe-O bond strength; thus providing effective reduction of the microalgal oil to form paraffins. Iron can facilitate hydroprocessing of vegetable oils through binding and subsequent activation of the oxygenates. Addition of iron to copper can also improve the surface area of copper and inhibit its sintering (Bykova et al., 2012). The supports used in the hydroprocessing of vegetable oil need to complement the activity role played by the active site phase of the catalyst. This can be achieved by synthesizing catalysts' support of high surface area and pore volume. Light hydrocarbons production can be avoided by using catalyst support of moderate Brønsted acid sites (Rabaev et al., 2015).

Alumina, silico-alumino phosphates, zeolites, zirconium oxide and mesoporous materials have been utilized by researchers for the hydroprocessing of vegetable oils (Kazuhisa et al. 2010; Deepak et al. 2011; Verma et al. 2015). Kazuhisa et al (2010) worked on the hydroprocessing of jatropha oil over a catalyst supported on ZSM-5 (23 wt% silica–alumina ratio) in a 100 mL autoclave batch reactor at 300 °C, 6.5 MPa H₂ pressure, 1 g catalyst/g feed and 12 h reaction time. An 83.8% conversion of jatropha oil, 3.06% CO₂ selectivity, 16% C₁–C₄ hydrocarbon selectivity and 80.7% C₁₀–C₂₀ hydrocarbons yield were obtained. This shows the high activity and selectivity strength of ZSM 5 zeolite-supported catalyst for liquid hydrocarbons. It also shows the cracking effects of ZSM 5, thus indicating it can also be suitable for the hydrodeoxygenation and hydrocracking of vegetable oils to produce jet-fuel hydrocarbon fractions. Mixed support of SiO₂ and Al₂O₃ has also been used for hydroprocessing of vegetable oil. Yanyong et al (2011) examined the hydroprocessing of vegetable oils over the NiMo/SiO₂, NiMo/Al₂O₃ and NiMo/SiO₂-Al₂O₃ catalysts at 350 °C and 4 MPa H₂ pressure. The catalysts supported by the mixture of silica and

alumina gave the highest and the most desirable iso/normal ratio (0.26). This shows clearly that SiO₂-Al₂O₃-supported catalysts have more preference for hydroprocessing of vegetable oils for bio-jet fuel production as compared to the Al₂O₃- and SiO₂-supported catalysts. Amorphous silica alumina support is viewed as a polymer of Al₂O₃ on a backbone of SiO₂, while crystalline ZSM-5 and HZSM materials are viewed as copolymers of Al₂O₃ and SiO₂ with capacities for ion exchange (Ali et al., 2002). These three materials have varying Brønsted acid sites concentrations. Hydroprocessing of vegetable oils for production of jet-fuel range hydrocarbon largely depends on Brønsted acid sites concentrations of the catalysts used (Rabaev et al., 2015).

In this work, the catalytic performance on the conversion of model compound of vegetable oils (oleic acid), yield and selectivity of jet-fuel range hydrocarbons were studied over the Cu/SiO₂-Al₂O₃, FeCu/SiO₂-Al₂O₃, FeCu/ZSM-5 and FeCu/HZSM-5 catalysts. These catalysts were characterized for determination of their physicochemical properties and their impacts on product selectivity. The influence of reaction temperature, contact time and catalyst acidity were also investigated.

4.3 Experimental Section

Amorphous SiO₂/Al₂O₃ (silica alumina ratio: 6.25) and Oleic acid were obtained from Sigma Aldrich (Missouri, USA). The precursors used for catalyst synthesis are CuNO₃. 2.5H₂O, FeNO₃. 9H₂O and SnCl₄. 5H₂O. FeNO₃. 9H₂O and CuNO₃. 2.5H₂O were supplied by Millipore (Canada) Ltd (Ontario, Canada) and ES company (New Jersey, USA), respectively. SnCl₄. 5H₂O was purchased from Sigma Aldrich (Missouri, USA).

Prior to synthesis, the mass of precursors required for 1 wt. % Sn, 3 wt. % Fe and 13 wt. % Cu on an amorphous silica alumina support was calculated based on the values of the molecular weight of each precursor and its respective metal content. Each precursor was dissolved in water and their resulting solution was impregnated into the support using wet and co-impregnation techniques. The mixture obtained was dried in an oven at 100 °C overnight. The dried mixture was then calcined in flowing air at a temperature of 450 °C, heating rate of 1 °C/min for 6 h. The resulting sample from calcination was reduced with hydrogen gas flowing at 50 ml/min at a reduction temperature of 400 °C and heating rate of 1 °C/min for 4 h. The reduced catalyst was then passivated in a flow of 1% O₂/N₂ of 50 ml/min flow rate at room temperature for 1 h.

PerkinElmer Optima 5300DV inductively coupled plasma-optical emission spectrometry (ICP-OES) instrument was used to evaluate the mass composition of Sn, Fe and Cu in the catalyst. The

mass composition of Cu in the catalyst was evaluated through the digestion of 0.125 g of the catalyst in a concentrated HClO₃/HNO₃/HF mixture. The mixture of LiBO₂ and Li₂B₄O₇ was fused with 0.1 g of the catalyst sample for the evaluation of the mass composition of Sn and Fe. N₂ physisorption technique was utilized to determine textural properties of the 1 wt. % Sn promoted Fe(3)-Cu(13)/SiO₂-Al₂O₃ catalyst with the aid of a Micromeritics ASAP 2000 instrument. The catalyst was degassed at 250 °C for 5 h and then evacuated until pressure less than 10 μmHg was attained. Barrett-Joyner-Halenda (BJH) model was used for the evaluation of pore volume and pore diameter of the catalyst. The specific surface area of the catalyst was determined using the Brunauer-Emmett-Teller (BET) technique. Bruker Vertex 70v vacuum Fourier transform infrared (FTIR) spectrometer was used to determine the nature of the catalyst acid sites. The Bronsted/Lewis acid site ratio of the catalyst was then evaluated using equation 4.1.

$$\frac{C_B}{C_L} = \frac{IT(B)}{IT(L)} \cdot \frac{IMEC(B)^{-1}}{IMEC(L)^{-1}} \quad (4.1)$$

Where, C_B/C_L is the ratio of Bronsted and Lewis acid sites concentration. IT(L) and IT(B) are the integrated transmittances of Lewis and Bronsted acid sites, respectively. IMEC(L) and IMEC(B) are integrated molar extinction coefficients (cm/μmol) of Lewis and Bronsted acid sites, respectively (Planton et al. 2003; Li et al. 2012).

The 1 wt. % Sn promoted trimetallic catalyst was evaluated in a 0.3 litre Parr reactor for oleic acid hydroprocessing for production of jet fuel range hydrocarbons and operating conditions were varied between 300-340 °C reaction temperature, 1.4-2.8 MPa H₂ pressure, 2-8 wt. % catalyst concentration and 6-10 h reaction time. For each reaction run, 2 g catalyst sample and 40 g oleic acid were loaded in the Parr reactor. The liquid product was analyzed by flame ionization detector equipped gas chromatograph (Agilent 7890A) with a 0.25 mm internal diameter and 30 m long DB 5 capillary column. The temperature of the oven was raised from 40 to 280 °C at a heating rate of 10 °C/min. The oven temperature was held at 280 °C for 5 mins. 1 μL of product sample was injected into the column using a 10:1 split ratio. The carrier gas used was helium.

4.4 Results and Discussion

4.4.1 N₂- Adsorption/Desorption Measurement

The N₂- adsorption/desorption isotherms of all the silica–alumina-supported catalysts and its support are shown in Figure A.3. For all the profiles shown in Figure A.3, at relatively low pressure, no significant adsorption was observed for the support and the catalysts showed the formation of monolayer of adsorbed molecules of nitrogen gas. Significant adsorption at high

relative pressure as shown in Figure A.3 indicates adsorption in mesoporous materials (Leofanti et al., 1998).

The profiles of the support ($\text{SiO}_2\text{-Al}_2\text{O}_3$) and the monometallic catalysts exhibit type IV isotherms indicating that the support and the catalysts are mesoporous. Despite different loadings of iron, the profiles of all the $\text{FeCu/SiO}_2\text{-Al}_2\text{O}_3$ catalysts exhibit type IV isotherm indicating mesoporosity (Leofanti et al., 1998). The pore diameters of the catalysts as shown in Table 4.1 for all the silica–alumina-supported catalysts and its support confirmed the type IV isotherm in Figure A.3 The pore diameters were 4.4–5.7 nm indicating mesoporous nature of material. Out of all the monometallic catalysts, $\text{Cu(13)/SiO}_2\text{-Al}_2\text{O}_3$ catalyst samples have the largest pore diameter of 5.3 nm. Pore diameter decreases with increase in iron loading (1–5 wt%) as shown in Table 4.1. This trend can be ascribed to pore blockage.

Table 4.1. Textural properties of catalyst samples and their respective supports.

Sample ID	BET Surface Area (m^2/g)	Micropore Volume (cm^3/g)	Mesopore Volume (cm^3/g)	Total Pore Volume (cm^3/g)	Pore Diameter (nm)	Crystallite Size (nm)
$\text{SiO}_2\text{-Al}_2\text{O}_3$	660	0.00	0.94	0.94	5.7	-
ZSM	393	0.17	0.07	0.24	2.4	-
HZSM	321	0.12	0.08	0.20	2.5	-
$\text{Cu(5)/SiO}_2\text{-Al}_2\text{O}_3$	623	-	0.94	0.94	5.2	7.3
$\text{Cu(10)/SiO}_2\text{-Al}_2\text{O}_3$	611	-	0.81	0.81	5.2	7.6
$\text{Cu(13)/SiO}_2\text{-Al}_2\text{O}_3$	455	-	0.81	0.80	5.3	8.7
$\text{Cu(15)/SiO}_2\text{-Al}_2\text{O}_3$	510	-	0.60	0.60	5.0	8.7
$\text{Fe(1)-Cu(13)/SiO}_2\text{-Al}_2\text{O}_3$	458	-	0.58	0.58	5.1	24.0
$\text{Fe(2)-Cu(13)/SiO}_2\text{-Al}_2\text{O}_3$	483	-	0.59	0.59	4.9	18.1
$\text{Fe(3)-Cu(13)/SiO}_2\text{-Al}_2\text{O}_3$	446	-	0.50	0.50	4.5	5.9
$\text{Fe(5)-Cu(13)/SiO}_2\text{-Al}_2\text{O}_3$	430	-	0.47	0.47	4.4	8.3
$\text{Fe(3)-Cu(13)/ZSM-5}$	266	0.10	0.06	0.16	2.4	33.8
$\text{Fe(3)-Cu(13)/HZSM-5}$	193	0.09	0.01	0.10	2.1	29.1

The N_2 - adsorption/desorption isotherms of the three catalysts ($\text{Fe(3)-Cu(13)/SiO}_2\text{-Al}_2\text{O}_3$, $\text{Fe(3)-Cu(13)/HZSM-5}$ and $\text{Fe(3)-Cu(13)/ZSM-5}$) and their respective supports ($\text{SiO}_2\text{-Al}_2\text{O}_3$, HZSM and ZSM-5 zeolite) are shown in Figure A.4. The profiles of $\text{SiO}_2\text{-Al}_2\text{O}_3$ support and $\text{Fe(3)-Cu(13)/SiO}_2\text{-Al}_2\text{O}_3$ catalyst exhibit type-IV isotherms. This indicates that the catalysts are mesoporous. Unlike $\text{Fe(3)-Cu(13)/SiO}_2\text{-Al}_2\text{O}_3$ catalyst and its respective support, Fe(3)-

Cu(13)/HZSM-5 and Fe(3)-Cu(13)/ZSM-5 and their respective supports, show no significant adsorption capacity within the relative pressure of 0–0.8. Low nitrogen adsorption occurs at very high relative pressure ($p/p_0 > 0.8$), indicating a mixed type I–type IV isotherm. It shows the presence of both micro- and mesoporosity in the two catalyst samples and their respective supports (Leofanti et al., 1998).

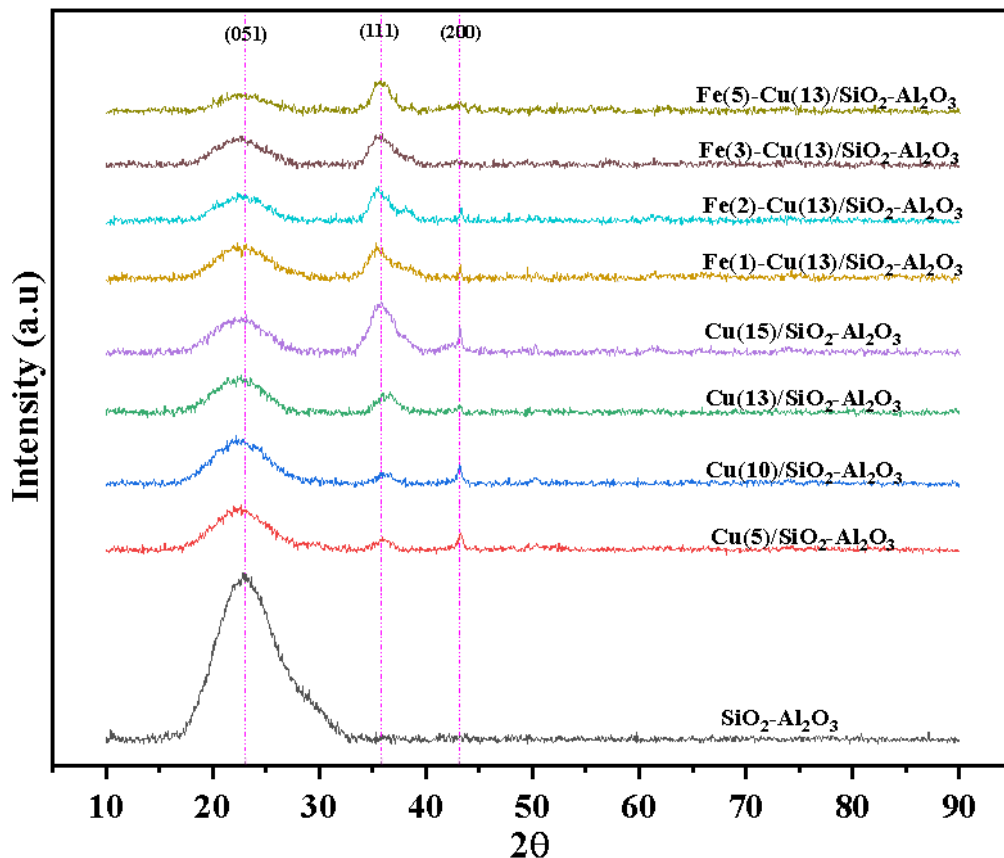


Figure 4.1. Wide angle XRD patterns of $\text{SiO}_2\text{-Al}_2\text{O}_3$, $\text{Cu}(5)/\text{SiO}_2\text{-Al}_2\text{O}_3$, $\text{Cu}(10)/\text{SiO}_2\text{-Al}_2\text{O}_3$, $\text{Cu}(13)/\text{SiO}_2\text{-Al}_2\text{O}_3$ and $\text{Cu}(15)/\text{SiO}_2\text{-Al}_2\text{O}_3$, $\text{Fe}(1)\text{-Cu}(13)/\text{SiO}_2\text{-Al}_2\text{O}_3$, $\text{Fe}(2)\text{-Cu}(13)/\text{SiO}_2\text{-Al}_2\text{O}_3$, $\text{Fe}(3)\text{-Cu}(13)/\text{SiO}_2\text{-Al}_2\text{O}_3$ and $\text{Fe}(5)\text{-Cu}(13)/\text{SiO}_2\text{-Al}_2\text{O}_3$ catalysts.

The textural properties of the three catalysts, ($\text{Fe}(3)\text{-Cu}(13)/\text{SiO}_2\text{-Al}_2\text{O}_3$, $\text{Fe}(3)\text{-Cu}(13)/\text{HZSM-5}$ and $\text{Fe}(3)\text{-Cu}(13)/\text{ZSM-5}$), and their respective supports ($\text{SiO}_2\text{-Al}_2\text{O}_3$, HZSM-5 and ZSM-5), are also shown in Table 4.1. The $\text{Fe}(3)\text{-Cu}(13)/\text{SiO}_2\text{-Al}_2\text{O}_3$ catalyst and its support have only mesoporous volumes, while other samples have both mesoporous and microporous volumes. The pore volume of all the supports decreases after metals loading due to blockage of the pores. Of all

the catalyst samples, Fe(3)-Cu(13)/SiO₂-Al₂O₃ has the largest surface area, pore volume and pore diameter.

4.4.2 XRD Analysis

The XRD patterns of the silica–alumina-supported catalysts and its support are shown in Figure 4.1. The 23° diffraction peak on the diffuse XRD pattern of silica alumina support coincides with the literature and the broadness of the peaks shows the material is amorphous (Morrettia et al. 1999; Ishihara et al. 2010; Saber et al. 2014; Toyoma et al 2016; Shalaby et al. 2018). The two peaks at 36° and 43° diffraction angles are ascribed to copper (I) oxide (Chen et al., 2016). The intensity of the peaks of copper (I) oxide at a 36° diffraction angle increases with copper loading. Diffraction peaks of copper (II) oxide, copper metal, iron oxides and iron were not observed due to their high dispersion on the support. The 42.5° diffraction angle peak attributed to copper (I) oxide in the diffractogram of Fe(3)-Cu(13)/SiO₂-Al₂O₃ catalyst is the most diffuse peak (Chen et al., 2016). The decrease in the crystallite size of Cu₂O in Fe(1)-Cu(13)/SiO₂-Al₂O₃, Fe(2)-Cu(13)/SiO₂-Al₂O₃ and Fe(3)-Cu(13)/SiO₂-Al₂O₃ with iron loading indicates the promotional effect of iron on the dispersion of copper (see Table 4.1). Of all the silica–alumina-supported bimetallic catalysts, Fe(3)-Cu(13)/SiO₂-Al₂O₃ catalyst has the lowest Cu₂O crystallite size of 5.9 nm. This indicates its potential of being active for hydroprocessing of oleic acid for production of jet-fuel range hydrocarbons (C₈–C₁₆).

The XRD patterns of the Fe(3)-Cu(13)/SiO₂-Al₂O₃, Fe(3)-Cu(13)/HZSM-5 and Fe(3)-Cu(13)/ZSM-5 catalyst samples and their respective supports are shown in Figure 4.2. The X-ray light incident in a periodically arranged crystalline materials scatters in a specific direction and results in high intensity narrow peaks, while the X-ray light incident in amorphous materials scatters in random directions and gives broad peaks. In Figure 4.2, the discrete X-ray diffraction patterns of HZSM-5 and ZSM-5 supports are sharp Bragg peaks. This shows that these two materials have high degree of crystallinity with long range order. The X-ray diffraction patterns of HZSM-5 and ZSM-5 coincide with that reported in the literature (Tao et al. 2003; Sanchez et al. 2017). The broad Bragg peak at 23° diffraction angle on the diffuse XRD pattern of amorphous silica alumina shows that it is amorphous and it also coincides with that reported in the literature (Toyoma et al 2016). The X-ray diffraction patterns of Fe(3)-Cu(13)/HZSM-5 and Fe(3)-Cu(13)/ZSM-5 show clearly the phases of Cu nanoparticles with the 23° sharp peak confirming the supports. In all the XRD patterns of FeCu/HZSM-5 and Fe(3)-Cu(13)/ZSM-5 catalysts, the

Bragg peaks at 43° , 51° and 74° diffraction angles, respectively, are ascribed to the presence of Cu nanoparticles (Betancourt-Galindo et al., 2014). These three characteristic diffraction peaks correspond to the (111), (200) and (220) planes of face-centred cubic structure of copper. The peaks at 36° and 42.5° in the diffractogram of Fe(3)-Cu(13)/SiO₂-Al₂O₃ catalyst are attributed to the presence of copper (I) oxide (Chen et al., 2016). The absence of the diffraction peaks of the reduced and oxidized phases of iron in all the samples can be ascribed to the fact that iron may be either present in its noncrystalline phase or in minute quantities below XRD sensitivity.

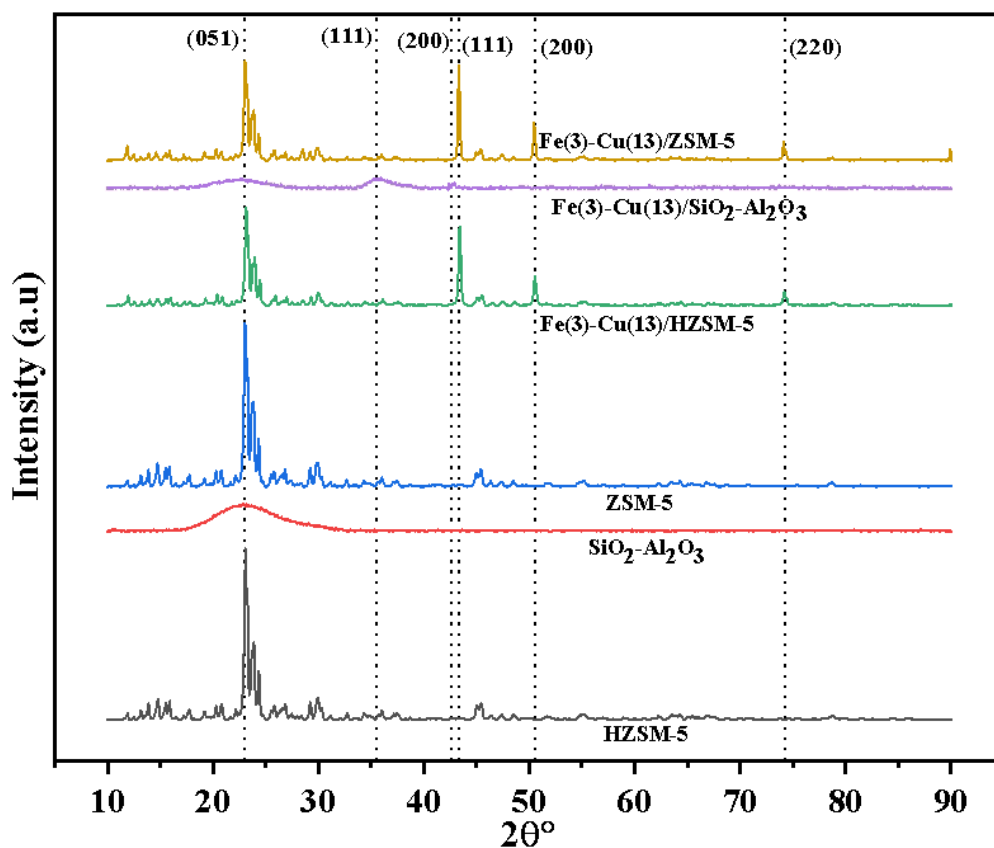


Figure 4.2. XRD patterns of SiO₂-Al₂O₃, ZSM-5 and HZSM-5 supports; Fe(3)-Cu(13)/SiO₂-Al₂O₃, Fe(3)-Cu(13)/ZSM-5 and Fe(3)-Cu(13)/HZSM catalysts.

From the N₂- adsorption/desorption measurement, the BET surface area of the silica–alumina support is the highest followed by the ZSM-5 support and HZSM-5 support. The catalyst, Fe(3)-Cu(13)/SiO₂-Al₂O₃ with the highest surface area, pore diameter and pore volume has the lowest copper phase crystallite size.

4.4.3 Inductively Coupled Plasma-Optical Emission Spectrometry (ICP-OES) and CO Chemisorption Analyses

The actual loadings of iron and copper in Fe(3)-Cu(13)/SiO₂-Al₂O₃, Fe(3)-Cu(13)/ZSM-5 and Fe(3)-Cu(13)/HZSM-5 catalyst samples evaluated using the ICP-OES shows that they are approximately the same as the targeted loading, if rounded up to the nearest whole number. The exact actual loadings of iron and copper of these three catalyst samples in terms of their weight percentage were used in their CO chemisorption analysis. The crystallite size and percentage dispersion surface area of Cu and Fe metals were calculated using the CO chemisorption method and tabulated in Table 4.2. The metals crystallite size increases in the order of Fe(3)-Cu(13)/SiO₂-Al₂O₃ < Fe(3)-Cu(13)/ZSM-5 < Fe(3)-Cu(13)/HZSM-5. Fe(3)-Cu(13)/SiO₂-Al₂O₃ catalyst has the lowest metals crystallite size as observed from both CO chemisorption analysis and XRD peaks. The Scherrer equation was used to calculate the crystallite size of the copper phase detected from X-ray diffractograms of the catalysts. Cu was detected in the Fe(3)-Cu(13)/ZSM-5 and Fe(3)-Cu(13)/HZSM-5 catalysts with metal crystallite sizes of 33.8 nm and 29.1 nm, respectively, while Cu₂O was detected in Fe(3)-Cu(13)/SiO₂-Al₂O₃ catalyst with a crystallite size of 5.9 nm. All the reduced and oxidized phases of iron were not detected in the XRD patterns of the catalysts. These undetected iron phases were detected from XPS and TPR as discussed in later sections. Metals dispersion of the catalyst decreases with increase in their crystallite size as shown in Table 4.2. Metal dispersion of the three catalysts increases with the surface area of their respective support shown in Table 4.1. This trend can be attributed to increase in the proportion of catalysts' surface atoms with respect to the bulk catalysts. Fe(3)-Cu(13)/SiO₂-Al₂O₃ catalyst has the highest metal dispersion and largest surface area as compared to Fe(3)-Cu(13)/ZSM-5 and Fe(3)-Cu(13)/HZSM-5 catalysts.

4.4.4 Fourier Transform Infra-Red Analysis

The molecular structure of Fe(3)-Cu(13)/SiO₂-Al₂O₃, Fe(3)-Cu(13)/ZSM-5 and Fe(3)-Cu(13)/HZSM-5 catalysts and their respective supports was analyzed by the FTIR technique in the absorption region of 400–1400 cm⁻¹, as shown in Figure 4.3. The absorption band detected at 439 cm⁻¹ wavenumber can be ascribed to Si-O bending. The framework vibration at 537 cm⁻¹ wavenumber on the ZSM-5 and HZSM-5 support are characteristics of five membered rings tetrahedron shaped MFI zeolites. The absorption detected at 791 cm⁻¹, 1065 cm⁻¹ and 1210 cm⁻¹ wavenumbers can be ascribed to the external symmetric stretch, internal asymmetric stretch and

external asymmetric stretch, which are typical for extremely siliceous materials (Hosseinpour et al. 2017; Shalaby et al. 2018). The peaks were more intense in ZSM-5 and HZSM because of their higher silica–alumina ratio as compared to that of the silica–alumina support. There was a slight peak shift to a higher wavenumber at 537 cm^{-1} after Cu and Fe impregnation on HZSM-5 in the framework vibration ascribed to five membered rings tetrahedron shaped MFI zeolites. There was also slight shift of peaks to a higher wavenumber at 1065 cm^{-1} after Cu and Fe impregnation on ZSM-5 and HZSM-5 in the absorption band ascribed to internal asymmetric stretch of extremely siliceous materials. These shifts of FTIR peaks after impregnation of Cu and Fe are due to change in bond length of the aluminosilicate frameworks in the catalyst samples (Hosseinpour et al. 2017; Shalaby et al. 2018).

Table 4.2. ICP-OES and CO chemisorption analyses of catalyst samples.

Catalyst Samples	ICP-OES		Metals Dispersion (%)	Metallic	Metallic	Metals Crystallite Size (nm)
	Cu (wt. %)	Fe (wt.%)		Surface Area (m^2/g Sample)	Surface Area (m^2/g metal)	
Fe(3)-Cu(13)/SiO ₂ -Al ₂ O ₃	13.0	2.5	8.4	8.1	54.3	8.4
Fe(3)-Cu(13)/ZSM-5	13.1	3.1	7.6	7.6	46.7	9.8
Fe(3)-Cu(13)/HZSM-5	13.4	3.2	6.3	6.5	38.4	11.9

4.4.5 X-ray Photoelectron Spectroscopy Analysis (XPS)

The XPS spectra of the Fe(3)-Cu(13)/SiO₂-Al₂O₃, Fe(3)-Cu(13)/ZSM-5 and Fe(3)-Cu(13)/HZSM-5 catalyst samples were fitted for both Cu2p and Fe2p using the CasaXPS software as shown in Figure 4.4. The analysis confirmed the presence of iron and copper in their oxides and reduced states in all the three catalyst samples (Biesinger et al. 2010; Xiao et al. 2012; Gao et al. 2013; Feng et al. 2016; Manikandan et al. 2016; Shen et al. 2016). Cu2p_{1/2} and Cu2p_{3/2} XPS peaks were observed at 935–937 eV and 954–956 eV respectively, while Fe2p_{1/2} and Fe2p_{3/2} XPS peaks were observed at 721–723 eV and 708–713 eV respectively. The weak satellite peak at 945 eV binding energy on the XPS spectra of Fe(3)-Cu(13)/HZSM and Fe(3)-Cu(13)/ZSM catalysts

confirms the presence of Cu_2O , while the strong satellite peak at the similar binding energy on the XPS spectra of Fe(3)-Cu(13)/ $\text{SiO}_2\text{-Al}_2\text{O}_3$ can be attributed to Cu^{2+} phase (He et al., 2011). The atomic compositions of the metal oxides and reduced metals obtained from the XPS spectra fitting were tabulated in Table 4.3. All the three catalyst samples consist of significant atomic composition of copper and iron in their oxide state, owing to the passivation of the surface of the catalysts during their synthesis. The results also show that all the catalyst samples consist of Fe_2O_3 in larger quantities as compared to FeO at the surface. The highest surface atomic composition of oxophilic iron metal was observed in the FeCu/ $\text{SiO}_2\text{-Al}_2\text{O}_3$ catalyst as revealed from XPS fitting. The varying composition of metals and their oxides in all the catalysts can be ascribed to their different metal–support interactions.

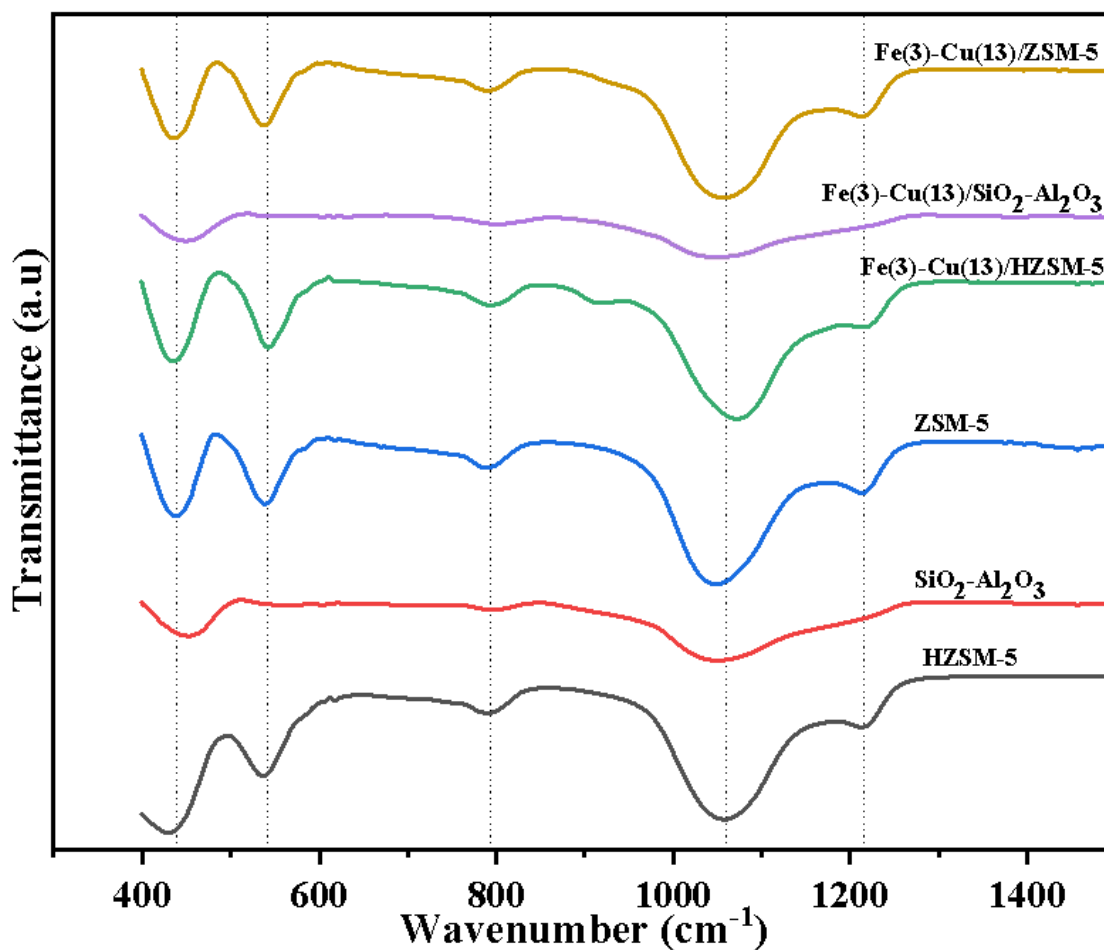


Figure 4.3. FTIR spectra of $\text{SiO}_2\text{-Al}_2\text{O}_3$, ZSM-5 and HZSM-5 supports; Fe(3)-Cu(13)/ $\text{SiO}_2\text{-Al}_2\text{O}_3$, Fe(3)-Cu(13)/ZSM-5 and Fe(3)-Cu(13)/HZSM catalysts.

4.4.6 H₂-TPR Analysis

The H₂-TPR profiles of the Fe(3)-Cu(13)/SiO₂-Al₂O₃, Fe(3)-Cu(13)/HZSM-5 and Fe(3)-Cu(13)/ZSM-5 catalysts are shown in Figure 4.5. The profiles confirmed the findings from XRD and XPS analyses that despite reduction of the catalyst samples during synthesis, they still consist of oxides of Cu. The H₂ uptake from the TPR result is in the order of Fe(3)-Cu(13)/SiO₂-Al₂O₃ > Fe(3)-Cu(13)/ZSM-5 > Fe(3)-Cu(13)/HZSM-5 as shown in Table 4.4. The reduction peak temperature at 207 °C, 289 °C and 321 °C in the respective profiles of Fe(3)-Cu(13)/SiO₂-Al₂O₃, Fe(3)-Cu(13)/ZSM-5 and Fe(3)-Cu(13)/HZSM-5 are ascribed to the reduction of copper oxides to copper while the hump above 300 °C in all the three TPR profiles are attributed to reduction of iron oxides to iron (Xiao et al., 2012). The reduction peak temperature from the TPR profiles and the crystallite size of the catalysts obtained from CO chemisorption analysis are in the same order of Fe(3)-Cu(13)/SiO₂-Al₂O₃ < Fe(3)-Cu(13)/ZSM-5 < Fe(3)-Cu(13)/HZSM-5. Low reduction peak temperature and low crystallite size indicate weak metal–support interaction, therefore the Fe(3)-Cu(13)/SiO₂-Al₂O₃ catalyst has the weakest metal–support interaction and highest metal dispersion (Manikandan et al. 2016; Shen et al. 2016).

4.4.7 Pyridine FTIR Analysis

Pyridine, ammonia and acetonitrile can be used to determine the Brønsted and Lewis acid sites of the catalysts. In this work, pyridine was used as molecular probe and it shows a clear distinction between the Brønsted and Lewis acid sites. Moreover, the kinetic diameter of pyridine is 0.57 nm which is lower than the 2.1–5.7 nm pore size of the catalysts (Barzetti et al., 1996). Catalysts of high Brønsted/Lewis acidity ratio favours cracking and is also not selective for dehydrogenation (Ma et al., 2018). Cracking is desired for hydroprocessing of oleic acid for production of jet-fuel range hydrocarbons and dehydrogenation is undesirable. Pyridine FTIR spectra and Brønsted/Lewis acid sites ratio of Fe(3)-Cu(13)/SiO₂-Al₂O₃, Fe(3)-Cu(13)/ZSM-5 and Fe(3)-Cu(13)/HZSM-5 catalysts were shown in Figure S3 and Figure 6, respectively. The Brønsted/Lewis acid sites ratio increases in the order of Fe(3)-Cu(13)/SiO₂-Al₂O₃ < Fe(3)-Cu(13)/ZSM-5 < Fe(3)-Cu(13)/HZSM-5 as shown in Figure A.5. Fe(3)-Cu(13)/HZSM-5 and Fe(3)-Cu(13)/ZSM-5 catalysts have higher Brønsted/Lewis acid sites ratio as compared to the Fe(3)-Cu(13)/SiO₂-Al₂O₃ catalyst. This indicates that the MFI zeolite catalysts are richer in Brønsted acid sites. Fe(3)-Cu(13)/HZSM-5 catalyst have higher Brønsted/Lewis acid sites ratio in comparison with Fe(3)-Cu(13)/ZSM-5 due to the protonation of the ZSM-5 support.

Brønsted/Lewis sites ratio of the catalyst as shown in Figure A.5 has significant influence on selectivity of jet-fuel range hydrocarbons as discussed in the later section.

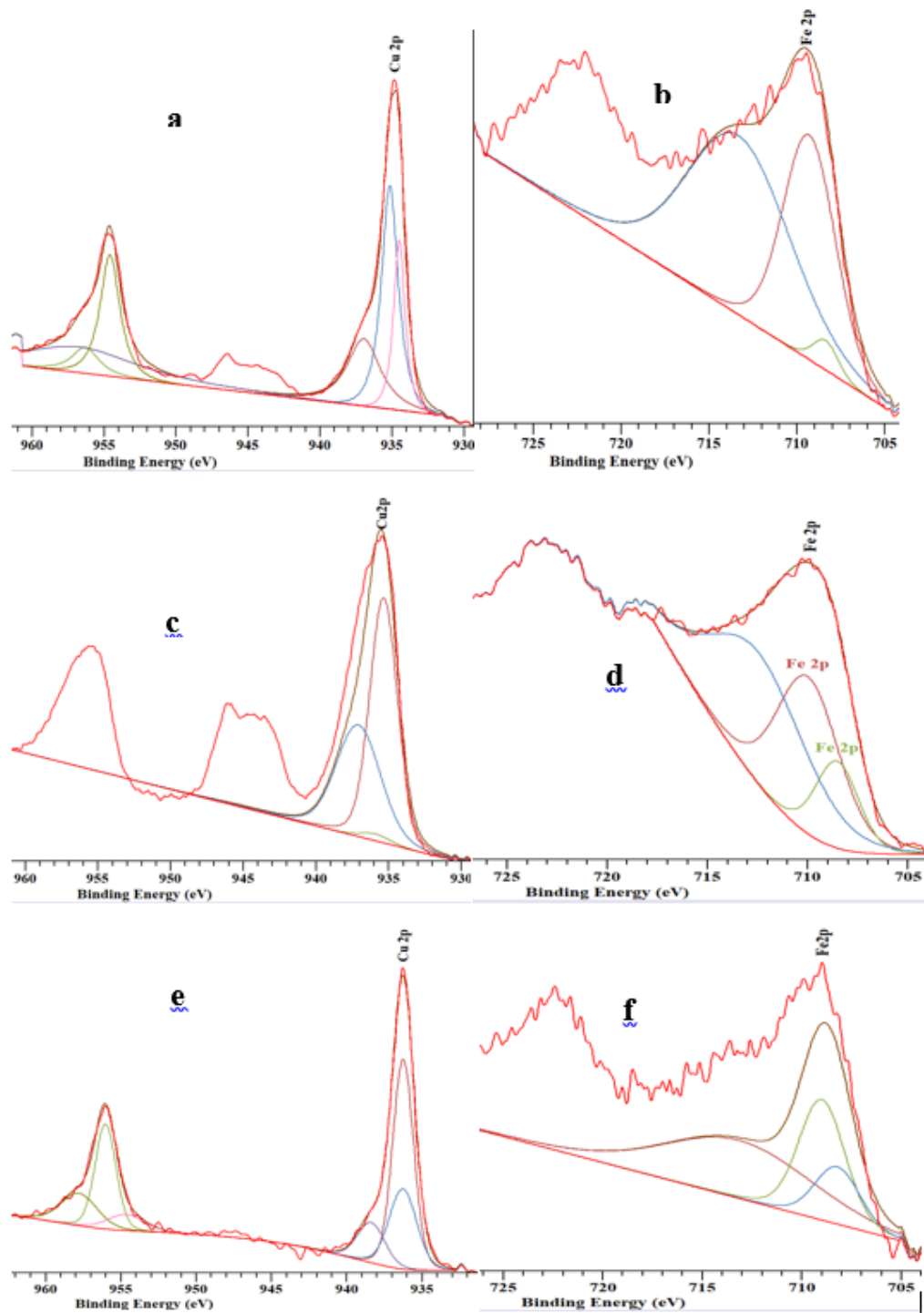


Figure 4.4. Cu2p and Fe2p XPS spectra of (a,b) Fe(3)-Cu(13)/HZSM (c,d) Fe(3)-Cu(13)/SiO₂-Al₂O₃ (e,f) Fe(3)-Cu(13)/ZSM-5 catalysts.

Table 4.3. Cu_{2p_{3/2}} and Fe 2p_{3/2} values for Fe(3)-Cu(13)/SiO₂-Al₂O₃, Fe(3)-Cu(13)/ZSM-5 and Fe(3)-Cu(13)/HZSM catalysts.

Catalysts	Component	Binding Energy of Cu or Fe 2p _{3/2} (eV)	Atomic Composition (%)
Fe(3)-Cu(13)/HZSM	Cu ₂ O	935	24.3
	Cu	936	47.4
	CuO	937	28.3
	Fe	708	2.4
	FeO	709	38.1
	Fe ₂ O ₃	713	58.5
Fe(3)-Cu(13)/SiO ₂ -Al ₂ O ₃	Cu ₂ O	935	57.1
	Cu	936	1.7
	CuO	937	41.2
	Fe	708	25.9
	FeO	709	35.6
	Fe ₂ O ₃	713	38.5
Fe(3)-Cu(13)/ZSM	Cu ₂ O	935	31.4
	Cu	936	52.9
	CuO	937	15.7
	Fe	708	15.5
	FeO	709	33.3
	Fe ₂ O ₃	713	51.2

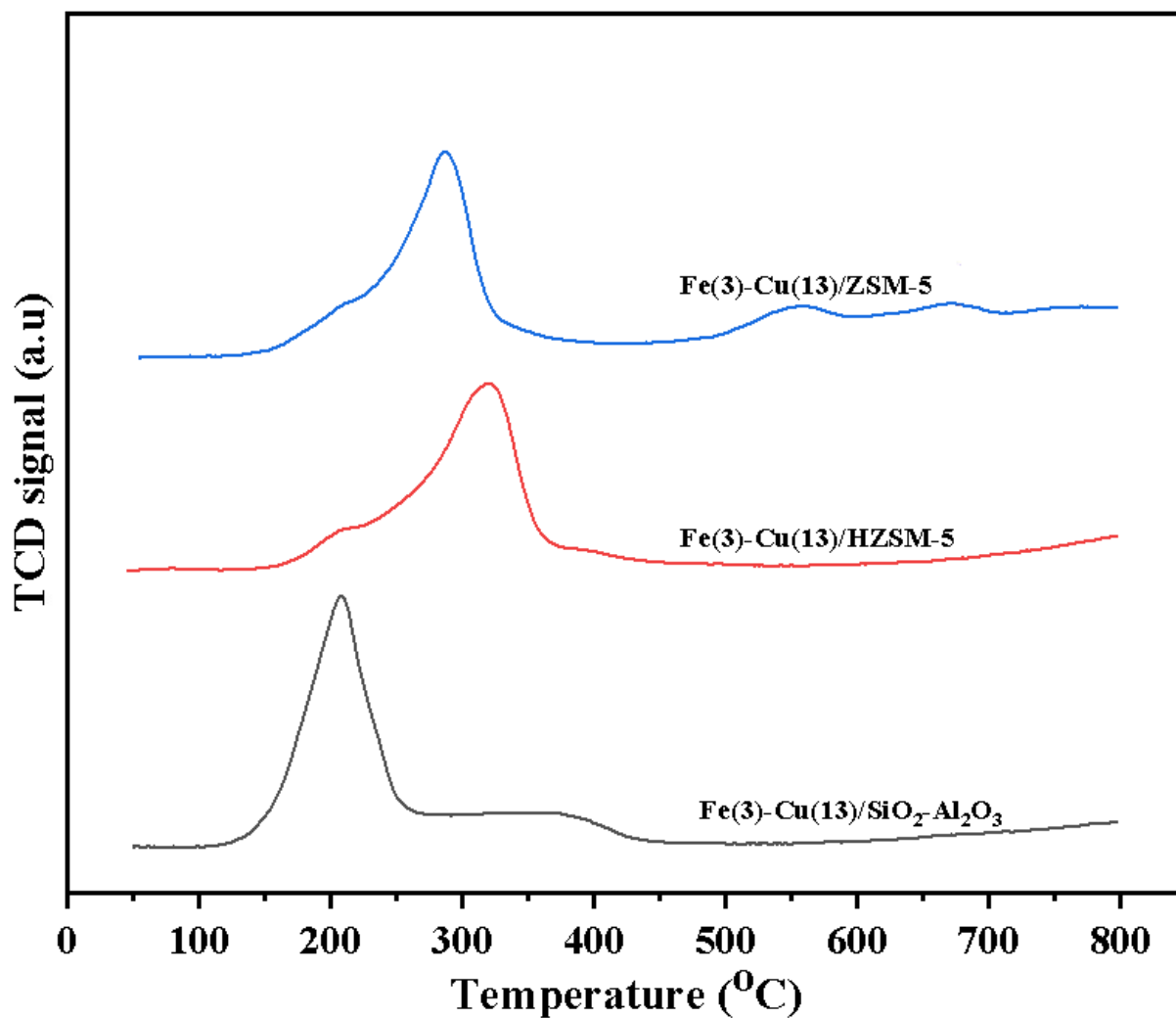


Figure 4.5. TPR profiles of Fe(3)-Cu(13)/SiO₂-Al₂O₃, Fe(3)-Cu(13)/ZSM and Fe(3)-Cu(13)/HZSM catalysts.

Table 4.4. H₂ uptake and reduction peak temperatures of catalyst samples.

Catalyst Samples	Reduction Peak Temperature (°C)	H ₂ Uptake (mmol g ⁻¹ cat)
Fe(3)-Cu(13)/SiO ₂ -Al ₂ O ₃	207	3.1
Fe(3)-Cu(13)/ZSM	289	2.6
Fe(3)-Cu(13)/HZSM	321	1.6

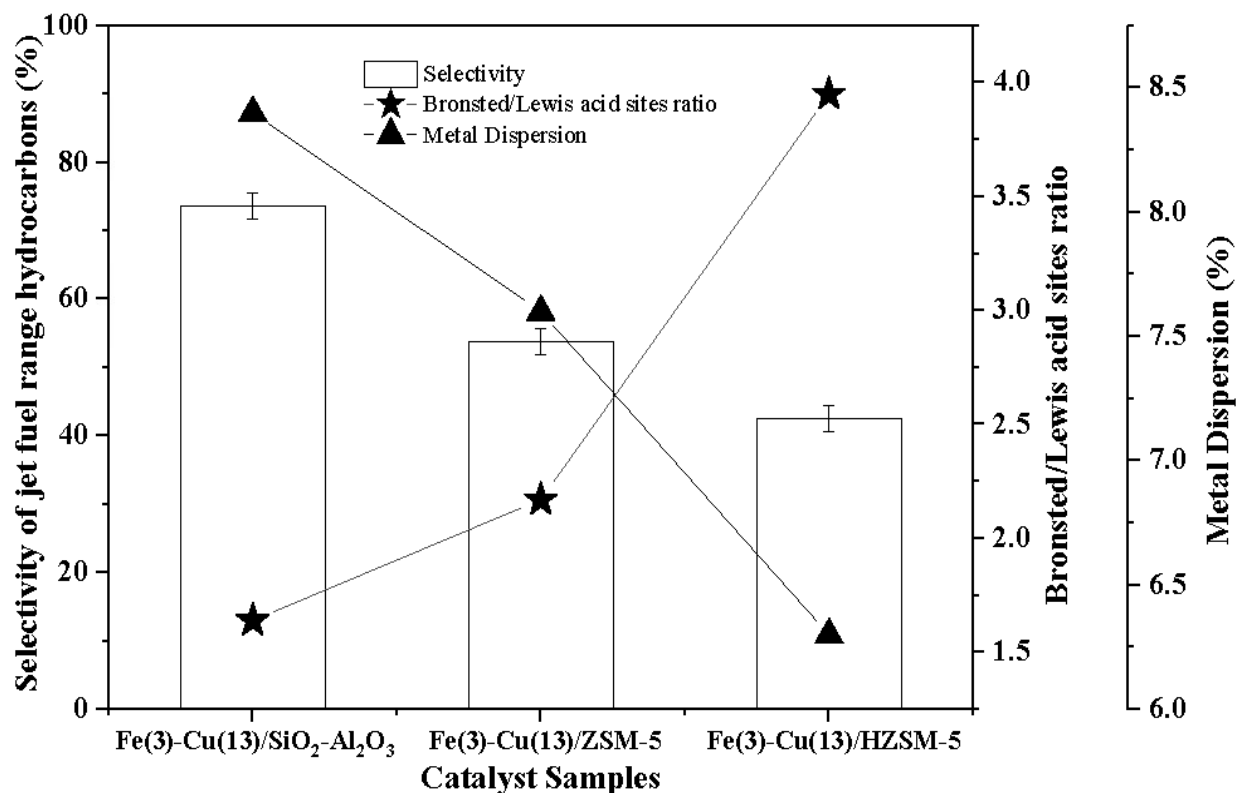


Figure 4.6. Selectivity of jet fuel hydrocarbons at 300 °C and 2.07 MPa H₂ pressure over the Brønsted/Lewis acid sites ratio and metal dispersion of Fe(3)-Cu(13)/SiO₂-Al₂O₃, Fe(3)-Cu(13)/ZSM-5 and Fe(3)-Cu(13)/HZSM-5 catalysts.

4.4.8 Catalyst Evaluation

The products obtained from the hydroprocessing reaction were analyzed based on oleic acid conversion, yield and selectivity of jet-fuel range hydrocarbons. The results obtained from the gas chromatography (GC) analysis show that reaction time, temperature and catalysts have significant effects on the conversion of oleic acid, yield and selectivity of the jet-fuel range hydrocarbons. The error % for all the result was within $\pm 5\%$. Figure 4.7 shows the results obtained from the evaluation of Cu(5)/SiO₂-Al₂O₃, Cu(10)/SiO₂-Al₂O₃, Cu(13)/SiO₂-Al₂O₃ and Cu(15)/SiO₂-Al₂O₃ catalysts at 340 °C, 2.07 MPa hydrogen pressure and 5% catalyst/feed ratio. The effects of reaction times (2–10 hours) on the conversion of oleic acid is shown in Figure 4.7.

The conversion of oleic acid increases with time for all the four catalysts. The highest oleic acid conversion obtained was 78.4% at 10 hours from the evaluation of Cu(13)/SiO₂-Al₂O₃ catalyst. The effects of reaction time (2–10 hours) on the selectivity of jet-fuel range hydrocarbons are shown in Figure 4.7. The highest selectivity of jet-fuel range hydrocarbons obtained was 41.9% respectively at 6 hours. Unlike conversion of oleic acid, which increases with time, the selectivity of jet-fuel range hydrocarbons initially increases and later decreases with reaction time due to subsequent cracking of the jet-fuel range hydrocarbons to lighter hydrocarbons shown in Table A.1. Oleic acid consists of macromolecules requiring catalyst of high pore size for easy internal diffusion. Cu(13)/SiO₂-Al₂O₃ performs better than the other three monometallic catalysts due to its high pore diameter (5.3 nm), which implies high accessibility of oleic acid and hydrogen to the active site (copper) of the catalyst.

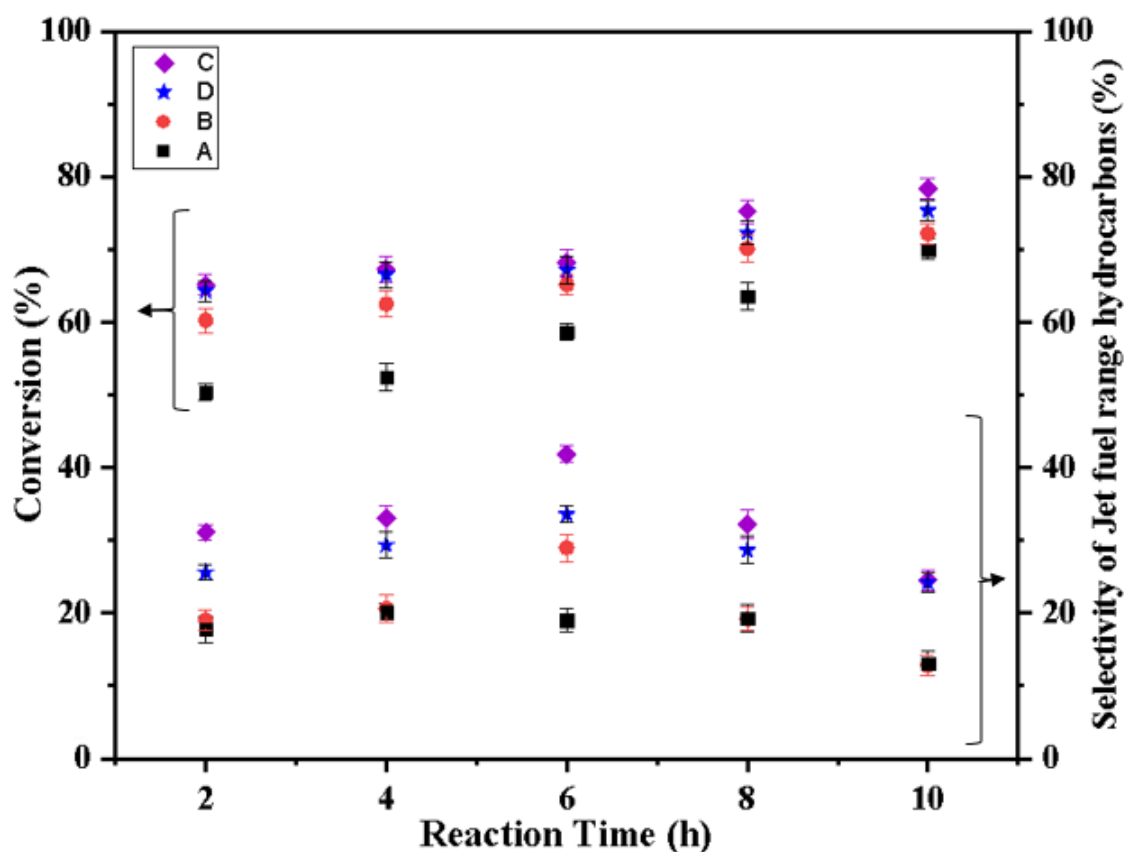


Figure 4.7. Conversion of oleic acid and selectivity of jet fuel hydrocarbons at different temperatures and 2.07 MPa H₂ pressure over the (A) Cu(5)/SiO₂-Al₂O₃, (B) Cu(10)/SiO₂-Al₂O₃, (C) Cu(13)/SiO₂-Al₂O₃ and (D) Cu(15)/SiO₂-Al₂O₃ catalysts.

The effects of reaction time (2–10 hours) on oleic acid conversion and selectivity of jet-fuel range hydrocarbons over the FeCu/SiO₂-Al₂O₃ catalysts are shown in Figure 4.8. The conversion of oleic acid increases with time for all the catalysts. The highest oleic acid conversion obtained was 98% at 10 hours from the evaluation of Fe(3)-Cu(13)/SiO₂-Al₂O₃ catalyst. The highest selectivity of jet-fuel range hydrocarbons obtained was 53.8% at 10 hours. The better performance of Fe(3)-Cu(13)/SiO₂-Al₂O₃ catalyst is due to its smaller crystallite size and high dispersion of copper and iron metals and high reducibility of metals as compared to the other three catalysts.

The effects of reaction times (2–10 h) and temperature (300–340 °C) on oleic acid conversion, yield and selectivity of jet-fuel range hydrocarbons over the Fe(3)-Cu(13)/SiO₂-Al₂O₃, Fe(3)-Cu(13)/HZSM-5 and Fe(3)-Cu(13)/ZSM-5 catalysts are shown in Figures 4.9–4.11 and Table 4.5. The product distribution of C₈–C₁₆ is also shown in Table A.2. The conversion of oleic acid increases with reaction time and temperature for all the three catalyst samples. The conversion approximately stabilizes between 8 to 10 h for Fe(3)-Cu(13)/SiO₂-Al₂O₃ catalyst at 320–340 °C, Fe(3)-Cu(13)/ZSM catalyst at 300–340 °C and, Fe(3)-Cu(13)/HZSM catalyst at 320–340 °C.

The highest yield and selectivity of jet fuel hydrocarbons were recorded for Fe(3)-Cu(13)/SiO₂-Al₂O₃ catalyst at 300 °C as shown in Figure 4.11 and Table 4.5. The total number of surface atoms of Cu and Fe per the total number of atoms present in the catalyst increases with surface area. Catalysts of high Brønsted/Lewis acid site ratio favours cracking, while oligomerization and dehydrogenation are favoured by catalysts of low Brønsted/Lewis acid sites ratio (Ma et al., 2018). The internal diffusion calculation was carried out using the Weisz–Prater criterion as shown in Appendix B (Fogler et al., 2016). The Weisz–Prater parameter for this reaction was 3.6×10^{-7} which is much less than 1 indicating that the internal diffusion in catalyst particles is absent. The experimental data show that with reaction time, more lighter hydrocarbons (C₅–C₇) were produced from jet-fuel range hydrocarbons (C₈–C₁₆) due to deep and mild cracking. This may be due to acidic nature of the catalysts used in this study. Hydroprocessing reactions of fatty acids, triglycerides and vegetable oils require catalysts of mild Brønsted acid sites to produce jet-fuel range hydrocarbons. Catalysts of high Brønsted sites have higher tendency of producing hydrocarbons that are lighter than the jet-fuel range hydrocarbons (Rabaev et al., 2015). Catalysts of low Brønsted acid sites favor only the hydrodeoxygenation reaction with no sufficient cracking strength. The Fe(3)-Cu(13)/SiO₂-Al₂O₃ catalyst has mild Brønsted/Lewis acid sites ratio as proven

from Figure 4.6. The relationship between the metal dispersion, Brønsted/Lewis acid sites ratio and selectivity of jet-fuel range hydrocarbons at 300 °C and 2.07 MPa H₂ pressure over the Fe(3)-Cu(13)/SiO₂-Al₂O₃, Fe(3)-Cu(13)/ZSM-5 and Fe(3)-Cu(13)/HZSM-5 catalysts are shown in Figure 4.6. Fe(3)-Cu(13)/HZSM-5 catalyst has the lowest metal dispersion and Brønsted/Lewis acid sites ratio and the lowest selectivity of jet-fuel range hydrocarbons, while the Fe(3)-Cu(13)/SiO₂-Al₂O₃ catalyst has the highest metal dispersion and Brønsted/Lewis acid sites ratio and the highest selectivity of jet-fuel range hydrocarbons. The productivity of Fe(3)-Cu(13)/SiO₂-Al₂O₃, Fe(3)-Cu(13)/ZSM-5 and Fe(3)-Cu(13)/HZSM-5 catalysts in terms of g jet fuel/g catalyst/h and g jet fuel/m² metals surface area/g catalyst are shown in Table S3. The Fe(3)-Cu(13)/SiO₂-Al₂O₃ catalyst is the most productive catalyst, with 1.0 g jet fuel/g catalyst/h and 2.6 g jet fuel/m² metals surface area/g catalyst. The Fe(3)-Cu(13)/SiO₂-Al₂O₃ catalyst is the most promising when the entire temperature range (300–340 °C) is considered. This can be attributed to the relatively low Brønsted/Lewis acid sites ratio (Rabaev et al., 2015), high Cu and Fe metals dispersion, high pore volume, specific surface area of the Fe(3)-Cu(13)/SiO₂-Al₂O₃ catalyst and high surface composition of oxophilic iron metal observed from XPS fitting.

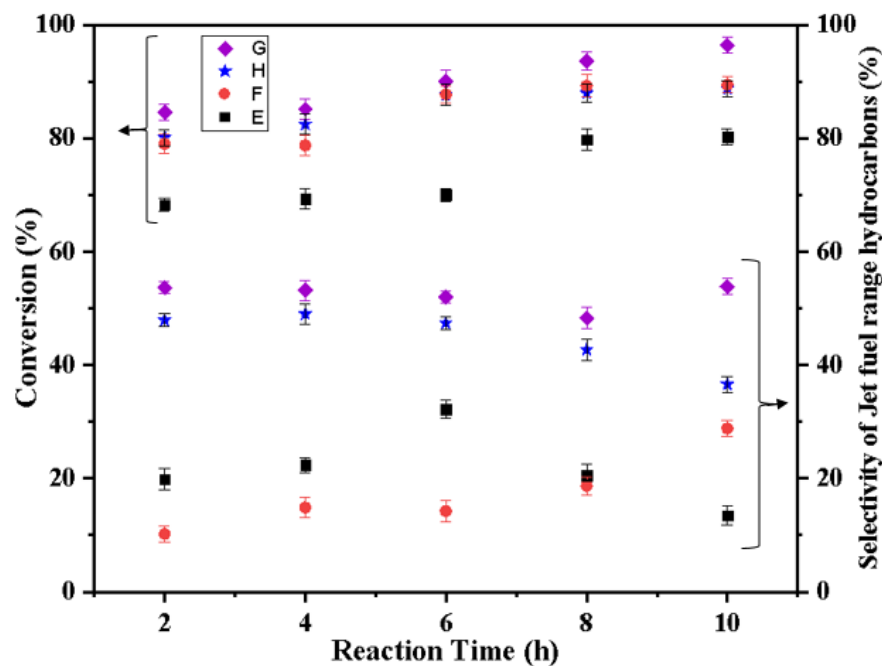


Figure 4.8. Conversion of oleic acid and selectivity of jet fuel hydrocarbons at different temperatures and 2.07 MPa H₂ pressure over the (E) Fe(1)-Cu(13)/SiO₂-Al₂O₃, (F) Fe(2)-Cu(13)/SiO₂-Al₂O₃, (G) Fe(3)-Cu(13)/SiO₂-Al₂O₃ and (H) Fe(5)-Cu(13)/SiO₂-Al₂O₃ catalysts.

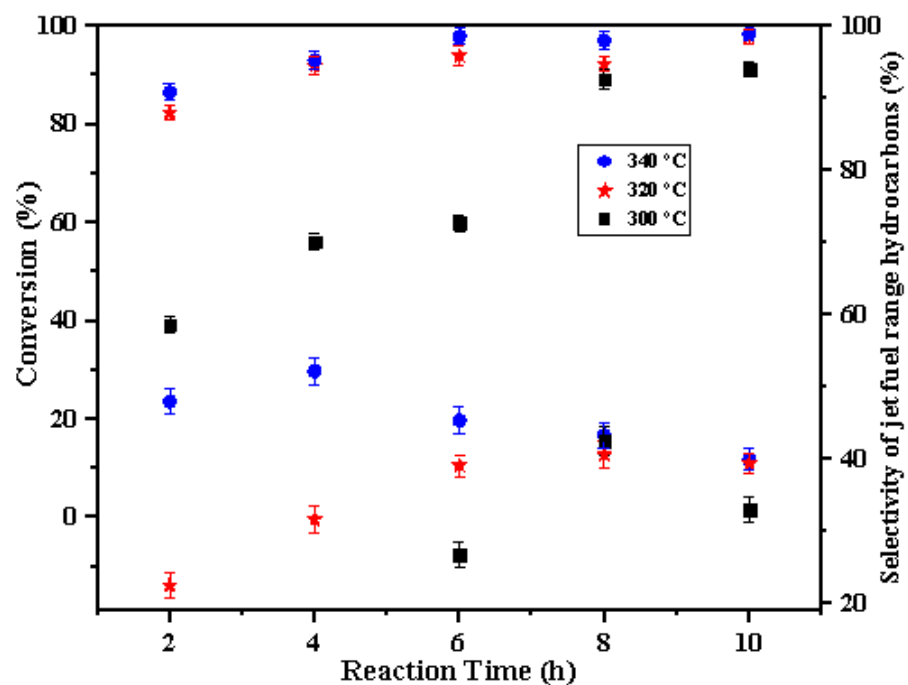


Figure 4.9. Conversion of oleic acid and selectivity of jet fuel hydrocarbons at different temperatures and 2.07 MPa H₂ pressure over the Fe(3)-Cu(13)/HZSM-5 catalyst.

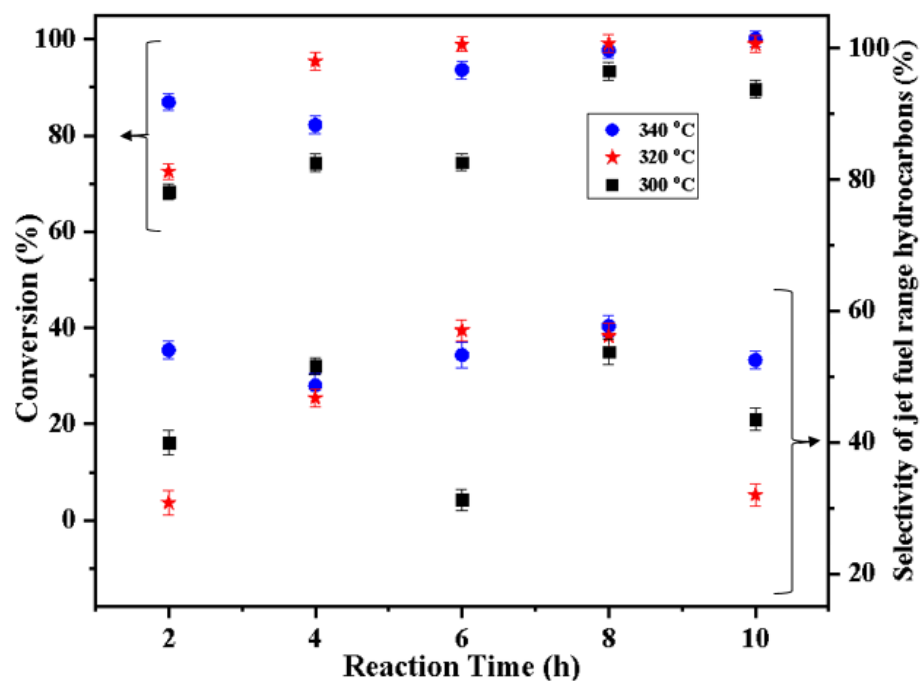


Figure 4.10. Conversion of oleic acid and selectivity of jet fuel hydrocarbons at different temperatures and 2.07 MPa H₂ pressure over the Fe(3)-Cu(13)/ZSM-5 catalyst.

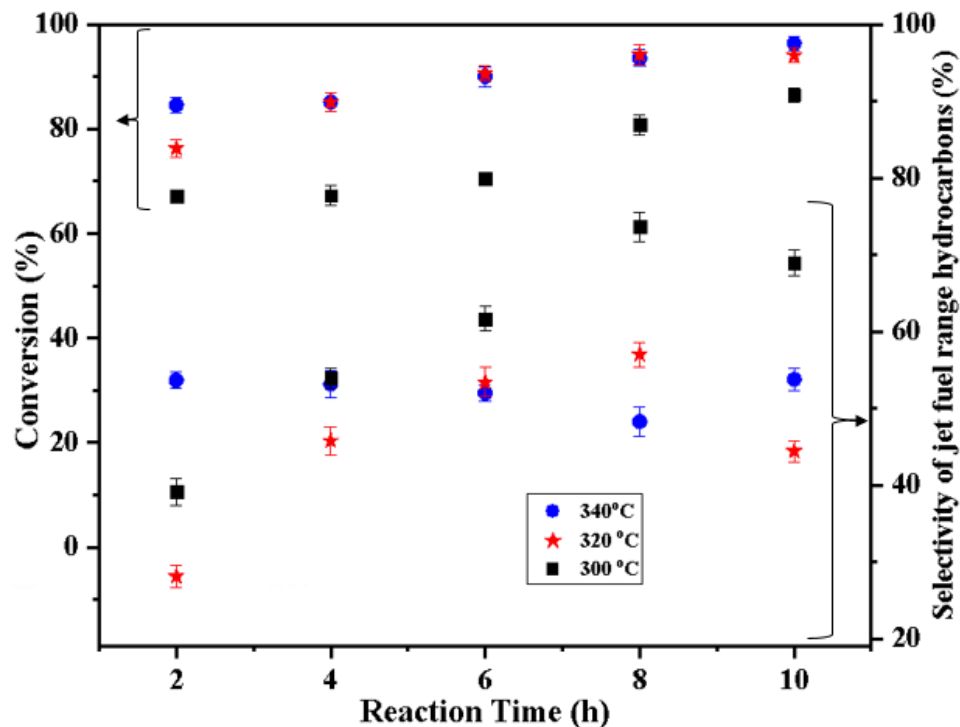


Figure 4.11. Conversion of oleic acid and selectivity of jet fuel hydrocarbons at different temperatures and P_{H_2} : 2.07 MPa H_2 pressure over the Fe(3)-Cu(13)/SiO₂-Al₂O₃ catalyst.

Table 4.5. Yield of C₈–C₁₆ hydrocarbons at t: 2–10 hours; T: 300–340 °C, and P_{H_2} : 2.07 MPa H_2 pressure.

Catalyst	Temperature (°C)	Residence Time (h)				
		2	4	6	8	10
Fe(3)-Cu(13)/SiO ₂ -Al ₂ O ₃	300	26.3	36.3	43.5	59.5	59.7
	320	21.5	39.0	48.4	53.7	41.8
	340	45.4	45.3	45.2	45.2	51.8
Fe(3)-Cu(13)/ ZSM	300	27.3	38.4	23.3	50.2	39.1
	320	22.3	44.6	56.4	55.7	32.4
	340	47.0	40.0	49.9	56.4	52.5
Fe(3)-Cu(13)/ HZSM-5	300	4.6	8.5	14.7	38.0	30.1
	320	19.2	29.5	38.3	39.5	38.9
	340	39.6	48.0	42.64	40.0	39.2

4.5 Conclusions

In summary, copper metal with optimized loading on silica alumina support was suitable for hydroprocessing of oleic acid for production of jet-fuel range hydrocarbons. The best monometallic catalyst performance with 41.9% selectivity of jet-fuel range hydrocarbons (C_8-C_{16}) was achieved at 340 °C, 2.07 MPa H_2 pressure and 6 hours reaction time over the catalyst with the largest pore size of 5.3 nm (Cu(13)/ $SiO_2-Al_2O_3$).

Optimization studies of iron promotional effects for hydroprocessing of oleic acid for production of jet-fuel range hydrocarbons on the Cu(13)/ $SiO_2-Al_2O_3$ catalyst showed more promising results in comparison with the monometallic copper catalysts due to effects of iron loading in lowering metal crystallite size indicating increase in metal dispersion. The best catalyst performance with 51.8% yield and 53.8% selectivity of jet-fuel range hydrocarbons was achieved over the iron-promoted copper catalyst with the lowest crystallite size (Fe(3)-Cu(13)/ $SiO_2-Al_2O_3$) at 340 °C, 2.07 MPa and 10 h of reaction time.

Support optimization studies on HZSM-5, ZSM-5 and $SiO_2-Al_2O_3$ supports reveal that Fe(3)-Cu(13)/ $SiO_2-Al_2O_3$ catalyst gives the best catalyst performance with 59.5% yield and 73.6% selectivity of jet-fuel range hydrocarbons. This promising performance was attributed to its large pore diameter, large pore volume and large surface area; low crystallite size and weak metal–support interaction from H_2 -TPR analysis, indicating, high metal dispersion from CO chemisorption analysis, high oxophilic iron content from XPS fitting and mild Brønsted acid sites from pyridine FTIR analysis.

CHAPTER 5

Hydroprocessing of oleic acid for the production of aviation turbine fuel range hydrocarbons over bimetallic Fe-Cu/SiO₂-Al₂O₃ catalysts promoted by Sn, Ti and Zr

The content of this chapter has been published in molecular catalysis journal as cited below:

Citation:

Ayandiran AA, Boahene PE, Nanda S, Dalai AK, Hu Y. Hydroprocessing of oleic acid for the production of aviation turbine fuel range hydrocarbons over bimetallic Fe-Cu/SiO₂-Al₂O₃ catalysts promoted by Sn, Ti and Zr. *Molecular Catalysis Journal* 5 (2021) 111358-111367.

Contribution of the Ph.D. Candidate

Preparation, characterization and screening of catalyst were planned and carried out by Afees A. Ayandiran in due consultation with Dr. Ajay K. Dalai and Dr. Yongfeng Hu. The manuscript was drafted and reviewed by Afees A. Ayandiran based on the guidance and suggestions provided by Dr. Ajay K. Dalai and Dr. Yongfeng Hu. Dr. Boahene Philip and Dr. Sonil Nanda also assisted in discussion phase and in reviewing the paper.

Contribution of this chapter to the overall PhD work

This chapter investigates the promoting effects of Sn, Ti and Zr on bimetallic Fe-Cu/SiO₂-Al₂O₃ catalysts for hydroprocessing of oleic acid for production of jet fuel range hydrocarbons. It also investigates the optimum loading of tin required to boost catalyst performance for production of jet fuel range hydrocarbons

5.1 Abstract

In this work, the synergistic effects of 1 wt.% Ti, 1 wt.% Zr, and Sn in the range of 0.5-2 wt.% on Fe(3)-Cu(13)/SiO₂-Al₂O₃ catalyst were ascertained through extensive characterization and their subsequent evaluation for the production of aviation turbine fuel (ATF) range hydrocarbons (C₈-C₁₆) via hydroprocessing of oleic acid. The largest surface area (571 m²/g) and pore volume (0.65 cm³/g) were obtained from the N₂ physisorption analysis of 1 wt.% Sn-promoted catalyst (E). Cu₂O and CuO were identified in the X-ray diffractograms (XRD) of all the catalysts except for catalyst E, which revealed only the peaks of Cu₂O owing to the small particle size of CuO below the threshold of detection of XRD. X-ray photoelectron spectroscopy (XPS) analysis revealed the presence of both oxidized and reduced phases of Cu, Fe, Ti, Zr and Sn in their respective catalysts, with the highest and lowest atomic compositions of reduced Fe

and CuO, respectively, detected in catalyst E; corroborating findings from XRD analyses. The relatively homogeneous dispersion of phases present in catalyst E (revealed by its smallest crystallite size of 5.1 nm) was also evidenced by the weakest metal-support interaction from the H₂-TPR analysis of the same catalyst. Hydroprocessing of oleic acid using catalyst E at T=320°C, H₂ pressure = 2.1 MPa, and time = 8 h, resulted in the the highest ATF range hydrocarbons selectivity of 76.8% and yield of 71.7% due to its high metal dispersion, desirable textural properties and high oxophilic reduced iron content.

5.2 Introduction

The significance of the aviation sector cannot be overemphasized, as it is responsible for the transportation of 54% of all international tourists and over 35% of world trade by value (ATAG, 2020). In 2018, nearly 4.4 billion passengers commuted and traveled through the global aviation sectors. Despite its importance, the development of the sector is associated with emissions of greenhouse gases. In 2018, over 895 megatonnes of CO₂ were emitted by the aviation industry at a global scale, whereas 12% and 2% of CO₂ emissions were recorded from the transportation sectors and anthropogenic sources, respectively (Wang and Tao, 2016). These greenhouse gas emissions are a leading cause of global warming, ocean acidification and climate change (Wang and Tao, 2016). For an effective reduction of the aviation industry's CO₂ footprint, leaders in the sector reached a consensus on long-term goals of attaining 50% drop in emissions by 2050 compared to 2005 levels. According to the agreement of the Aviation Environmental Protection Committee of the International Civil Aviation Organization, the development of sustainable aviation fuels is the most effective way in realizing the goals (Sgouridis et al. 2011; ICAO, 2018). Sustainable aviation fuels can be produced via hydroprocessing of oil-based feedstocks, upgrading of bio-oil synthesized from pyrolysis or hydrothermal liquefaction of liquid cellulose biomass, refining of the syncrude produced from syngas via Fischer-Tropsch synthesis, hydrodeoxygenation and alkylation of depolymerized lignin produced from lignocellulose biomass, anaerobic fermentation of hydrolyzed sugar, and also via hydrogenation of oligomerized proteins produced from alcohol dehydration (Wei et al., 2019). Of all the technologies utilized for bio-aviation turbine fuels, hydroprocessing of oil-based feedstocks has proven to have the highest overall energy efficiency, lowest aviation turbine fuel (ATF) selling price and lowest total capital investment (Diederichs et al., 2016).

Hydrodeoxygenation, hydrocracking, isomerization reactions are the hydroprocessing technologies used for the production of hydroprocessed renewable ATF from vegetable oils. Of all the oil-based feedstocks utilized for the production of ATF range hydrocarbons (C_8 - C_{16}), the non-edible oils are preferred to avert food *versus* fuel crisis caused by edible oils. Jatropha, green seed canola oil, Karanja oils, etc. are some examples of inedible oils with oleic acid as their main fatty acid components (Mohammad et al. 2013; Duan et al. 2020).

Copper-based catalysts are known for their high hydrogen activation capacities and high selectivity for hydrogenolysis of C=O and C-O bonds (Lup et al., 2018). Despite the unique qualities of Cu-containing catalysts for triglycerides hydroprocessing, their main drawback is low oxophilicity. Iron has high oxophilicity, which is essential for the abstraction of oxygen from the C-O and C=O bonds of triglycerides (Lup et al., 2018). Iron can also promote the dispersion and surface area of copper-based catalysts (Marimuthu et al., 2015; Yue et al., 2020).

Kandel et al (2014) evaluated the iron-based catalyst for hydroprocessing of microalgal triglycerides to obtain a high yield of liquid paraffins due to high iron oxophilicity. Hydroprocessing of oleic acid over Cu and FeCu catalysts for the production of ATF range hydrocarbons was carried out in our previous work in which copper loading optimization and the promotional effects of iron were studied (Ayandiran et al., 2019). The catalyst with 3 wt.% and 13 wt.% loadings of iron and copper, respectively gave the most promising ATF range hydrocarbons selectivity of 73.6%. This promising result was due to the decrease in the crystallite size evaluated from the X-ray diffraction (XRD) peaks of phases of copper from 24 nm to 5.9 nm, which implies an increase in dispersion as loading of iron was increased from 1wt.% to 3 wt.% (Ayandiran et al., 2019). Ti, Sn and Zr are highly oxophilic metals with high affinities for C=O and C-O bonds in fatty acids and triglycerides resulting in an effective abstraction of oxygen from these bonds (Lup et al., 2018). These three metals can also promote the textural promoters of Cu-based catalysts (Hu et al. 2007; Kandel et al. 2014; Zou et al. 2016; Xue et al. 2019).

The role played by catalysts' active sites are complemented using support with optimized Brønsted acid sites to achieve a balance between the production of hydrocarbons lower than C_8 and those that are higher than C_{16} . The supports with high specific surface areas and pore diameters are also required for triglycerides feedstocks because of their large molecular and kinetic diameters. SiO_2 - Al_2O_3 support has been reported to have these required qualities (Ayandiran et al., 2016). This mixed metal oxide support matrix was reported to have moderate Brønsted acid sites

and textural properties required for the production of ATF range hydrocarbons (Ayandiran et al., 2016). Yayong et al (2011) evaluated catalysts with silica, alumina and silica-alumina supports for hydroprocessing of vegetable oil and observed that the highest selectivity was accomplished with the silica-alumina supported catalyst.

In this work, the hydroprocessing of a model compound of vegetable oils (i.e. oleic acid) over Cu(13)-Fe(3)/SiO₂-Al₂O₃ catalysts promoted by Sn, Ti and Zr were studied for the production of ATF range hydrocarbons. The physicochemical properties and structural chemistry of the synthesized catalyst samples were determined via extensive catalyst characterization and the effects of reaction time, reaction temperature and catalysts' properties on the selectivity of ATF range hydrocarbons and oleic acid conversion were thoroughly investigated.

5.3 Experimental Section

The support material (amorphous SiO₂-Al₂O₃, silica/alumina ratio: 6.3) and the feedstock (oleic acid) used in this study were procured from Sigma-Aldrich Canada Ltd. (Oakville, Ontario, Canada). The metal precursors used including copper (II) nitrate hemi-pentahydrate (CuNO₃·2.5H₂O), iron (III) nitrate nonahydrate (Fe(NO₃)₃·9H₂O), titanium chloride (TiCl₄), zirconyl chloride octahydrate (ZrOCl₂·8H₂O) and tin (IV) chloride pentahydrate (SnCl₄·5H₂O) were purchased from Sigma-Aldrich Canada Ltd. and Fischer Scientific (Ontario, Canada).

In a typical preparation of the promoted tri-metallic catalyst, the base catalyst [Fe(3)Cu(13)/SiO₂-Al₂O₃] was promoted with approximately 1 wt.% of either Ti, Zr or Sn via sequential impregnation, intermittent drying and calcination steps, and denoted as C, D, and E. In addition, catalysts F and G were prepared in a similar manner by loading 0.5 wt.% and 2 wt.% Sn, respectively, on the base catalyst. The support material (silica-alumina) and the base catalyst [Fe(3)-Cu(13)/SiO₂-Al₂O₃] are named as A and B, respectively. The base catalyst was prepared by following the synthesis protocols described in our previous work (Ayandiran et al., 2016). Also, catalysts C, D and E were prepared by impregnating the required amounts of their respective Ti, Zr, or Sn precursor solutions to achieve the targeted 1 wt.% loading followed by drying at 100°C overnight prior to calcination at 450°C in a muffle furnace at 1°C/min for 6 h. The calcined sample was reduced using a 50 cm³/min flow of H₂ gas at 400°C by heating at 1°C/min for 4 h and passivated in 50 cm³/min flow of 1% O₂/N₂ at room temperature for 1 h. Catalyst E was selected from the three catalyst samples based on the result of their evaluation. Based on the result obtained from the evaluation of catalysts C, D and E for production of ATF range hydrocarbons via

hydroprocessing of oleic acid, catalysts F and G were also synthesized for effective optimization of tin loading.

The textural properties of the catalyst samples were determined using the N₂ physisorption technique. A Micromeritics ASAP 2000 (Micromeritics Instrument Corporation, Norcross, USA) was used to evaluate the physisorption isotherms of all the samples. Degassing of catalyst samples was carried out for 5 h at 250°C followed by evacuation until attaining a pressure of less than 10 µmHg. Brunauer-Emmett-Teller (BET) technique was utilized to calculate the surface area of each catalyst sample through N₂ physisorption at -196°C. The pore diameter and pore volume of the catalyst samples were evaluated using the Barrett-Joyner-Halenda (BJH) model.

The wide-angle X-ray diffractograms (XRD) of each catalyst sample and the SiO₂-Al₂O₃ support were obtained using a D8 ADVANCE XRD (Bruker AXS, Karlsruhe, Germany) equipped with CuK α radiation of 0.1541 nm wavelength. Each sample was scanned within a 10-80° diffraction angle (2 θ) at a rate of 0.05°/s. The peak of the phases detected was quantified for the determination of crystallite size using the Scherrer equation as explained in our previous work (Ayandiran et al., 2016).

The functional groups and the nature of surface acidic sites of the prepared catalysts were determined using a Vertex 70v vacuum Fourier transform infrared (FTIR) spectrometer (Bruker AXS, Karlsruhe, Germany) for FTIR and pyridine-FTIR analyses in a region of 400-1600 cm⁻¹. The surface atomic concentrations of the catalyst samples were identified using a Kratos AXIS Supra XPS system equipped with a monochromatic Al K α X-ray source (Kratos Analytical Ltd, Manchester, U.K.), located at the Saskatchewan Structural Sciences Centre in Saskatoon, Canada. The XPS spectra were deconvoluted using the CasaXPS software for the qualitative and subsequent quantification of the identified species.

The mass compositions of the active sites of the catalysts were analyzed in the Geo-analytical laboratory of Saskatchewan Research Council (SRC) using a PerkinElmer Optima 5300 DV inductively coupled plasma-optical emission spectrometry (ICP-OES) instrument (SpectraLab Scientific Inc., Markham, Canada). Iron, tin, titanium and zirconium in the various samples were analyzed by fusing the mixture of LiBO₂ and Li₂B₄O₇ with 0.1 g each of the catalyst samples. The copper metal in all the catalyst samples was analyzed via acid digestion of 0.125 g of each sample using a concentrated HF/HNO₃/HClO₃ acid mixture.

A thermal conductivity detector (TCD) equipped Micromeritics AutoChem 2950 HP chemisorption analyzer (Micromeritics, Norcross, GA, USA) was used for the H₂ temperature-programmed reduction (H₂-TPR) analysis by heating each catalyst samples in a 50 cm³/min H₂/Ar flow from 25-700°C at a heating rate of 10°C/min. A detailed explanation of the preparation of samples and analysis methods for BET, XRD, FTIR, pyridine-FTIR, XPS, ICP-OES and H₂-TPR is also explained in our previous work (Ayandiran et al., 2016).

The evaluation of the catalysts was performed in a 0.3 L Parr batch reactor. Approximately 40 g of oleic acid and 2 g of each catalyst sample were mixed in the reactor and pressurized with 2.1 MPa H₂. To exclude the influence of external mass transfer, an agitation test was initially carried out over 1 wt.% Sn-supported catalyst at 2.1 MPa H₂ pressure, 320°C and 8 h of reaction time to determine the minimum impeller speed required to prevent segregation of oleic acid, H₂ gas and the catalyst. For the main catalyst screening, the five catalysts were evaluated at 300, 320 and 340°C of reaction temperatures, 500 rpm impeller speed and 10 h of reaction time. Reusability test was carried out over the most promising catalyst by washing the used catalyst in acetone for removal of residual oil impurities and subjected to the same drying, calcination, reduction and passivation procedure as done for the fresh catalysts. The used catalyst was reused for additional six reaction cycles of 8 h reaction time each.

Chloroform was used to dilute the liquid product samples after filtration. An Agilent 7890A gas chromatography (GC) equipment (Agilent Technologies, Santa Clara, USA) equipped with a flame ionization detector (FID) was used to analyze the diluted product samples. A 0.25 mm inner diameter and 30 m long DB-5 capillary column was used. The oven temperature of the GC was increased to 280°C from 40°C at 10°C/min heating rate and 5 min of holding time at 280°C. Each product sample of 1 µL was injected with a 10:1 split ratio in the DB-5 column. The liquid products were quantified using an external standard consisting of C₅-C₁₉ hydrocarbons. The selectivity of the ATF range hydrocarbons (C₈-C₁₆) and oleic acid conversion was evaluated as explained in our previous work (Ayandiran et al., 2016).

5.4 Results and discussion

5.4.1 Characterization of support and catalysts

The targeted loadings of metals on catalysts B, C, D, E, F and G were confirmed by the actual loading in wt.% obtained from ICP-OES analysis as shown in Table 5.1. The actual loadings of copper, iron, titanium, zirconium and tin in their respective catalyst were approximately the

same as the target loading if the percentage loadings are approximated to the nearest whole number.

Table 5.1: ICP-OES analysis of catalyst samples

Catalyst samples	Cu	Fe	Ti	Zr	Sn
	wt.%				
Fe(3)-Cu(13)/SiO ₂ -Al ₂ O ₃ (B)	13.0	2.5	-	-	-
Ti(1)-Fe(3)-Cu(13)/SiO ₂ -Al ₂ O ₃ (C)	13.2	3.1	1.1	-	-
Zr(1)-Fe(3)-Cu(13)/SiO ₂ -Al ₂ O ₃ (D)	13.1	3.2	-	0.9	-
Sn(1)-Fe(3)-Cu(13)/SiO ₂ -Al ₂ O ₃ (E)	13.3	3.3	-	-	1.1
Sn(0.5)-Fe(3)-Cu(13)/SiO ₂ -Al ₂ O ₃ (F)	13.2	3.1	-	-	0.5
Sn(2)-Fe(3)-Cu(13)/SiO ₂ -Al ₂ O ₃ (G)	13.1	3.2	-	-	1.9

The N₂-physisorption isotherms of support A and catalysts B to G are depicted in Fig. 5.1. Remarkable adsorption capacities were observed at high relative pressure in all the isotherms. This indicates that the materials are mesoporous (Leofanti et al., 1998). Type IV isotherm was exhibited by all the catalyst samples and support indicating they are mesoporous materials.

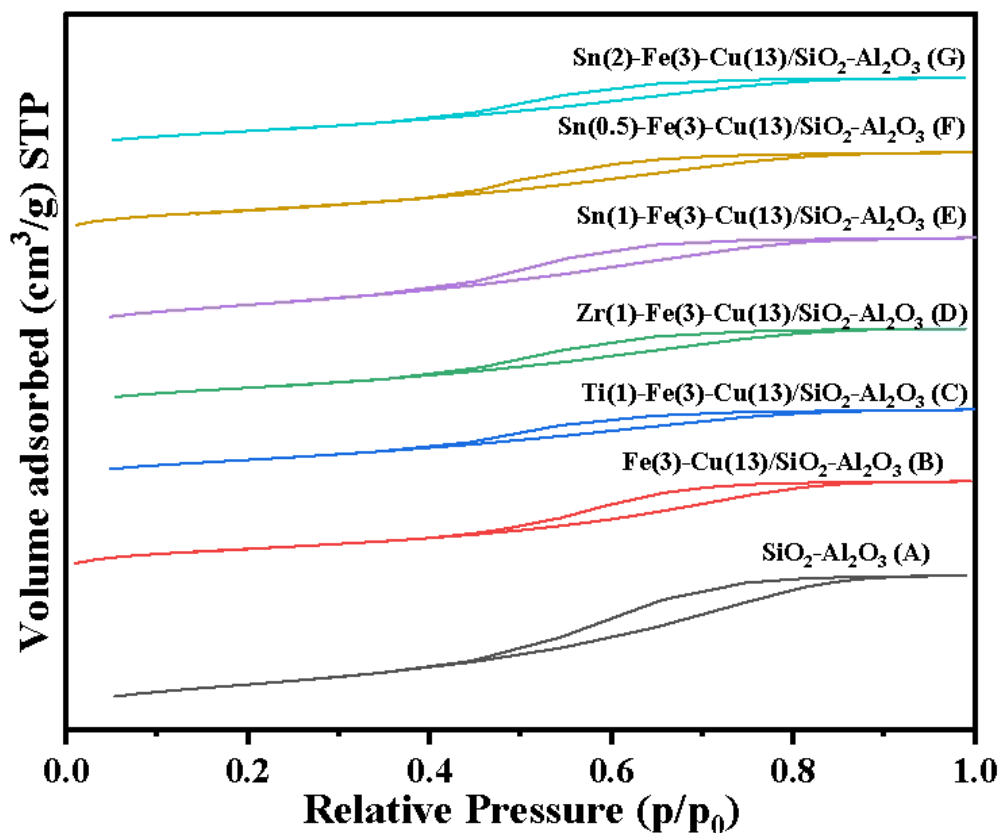


Figure 5.1: N₂-adsorption isotherms of support, base catalyst and Ti, Zr and Sn supported catalysts

The textural properties of support A and catalysts B to G are shown in Table 5.2. The average pore diameters of all the catalyst samples were above 4 nm; giving indication about the existence of textural mesoporosity in the prepared catalysts. The pore diameter and pore volume of SiO₂-Al₂O₃ support decreased after metal loading as shown for all the catalyst samples in Table 5.2 due to the anchorage of the respective metal oxide species with surface hydroxyl groups present on the pore wall of the support. The textural properties of the trimetallic catalysts in comparison with its bimetallic counterpart showed that the incorporation of titanium, tin and zirconium enhanced the dispersion of Fe and Cu on the surface of their respective catalyst via synergistic effects of the metals. In addition, the adherence of the promoter metals with the Fe and Cu species resulted in the formation a crystallites of smaller particles sizes on the SiO₂-Al₂O₃ support, which is responsible for the increase in the total surface area of the trimetallic catalysts. For instance, the 1 wt.% Sn-supported catalyst has a higher surface area and pore volume of 571 m²/g and 0.65 cm³/g, respectively, as compared to its Zr and Ti-incorporated supported catalysts. The latter catalysts have pore volumes of 0.55 cm³/g and 0.54 cm³/g, respectively, with approximately the same surface area of 465 m²/g. The surface area and pore volume of the Sn-promoted trimetallic catalyst increased from 465 m²/g and 0.54 cm³/g to 571 m²/g and 0.65 cm³/g as the loading of tin was increased from 0.5 wt.% to 1 wt.%; thus, indicating that the incorporation of Sn better enhanced the synergy between Fe and Cu and subsequently the dispersion of these metallic species on the SiO₂-Al₂O₃ support. On the other hand, the surface area and pore volume of the Sn-promoted trimetallic catalysts respectively decreased from 571 m²/g and 0.65 cm³/g to 452 m²/g and 0.51 cm³/g as the loading of Sn was increased from 1 wt.% to 2 wt.%. The observed negative trend indicates that at 2 wt.% Sn loading, the high loading of Sn may have resulted in the creation of crystallites of bigger particle sizes; leading to the agglomeration and subsequent partial plugging of catalyst pores (Marimuthu et al. 2015; Zou et al. 2016).

The phases and crystallographic structures of support A and catalysts B to G are depicted in the XRD patterns in Fig. 5.2. All the catalysts and the support have broad 2 θ diffraction peaks at 23° Bragg angle, which is typical for amorphous silica-alumina structures (Saber et al., 2014). The 2 θ diffraction peaks at 36° and 43° in all the catalyst samples can be ascribed to the existence of the cubic structure of Cu₂O, while the weak 2 θ peaks at 38° suggests the presence of monoclinic structure of CuO in catalysts B to G (Dubale et al., 2016). The absence of characteristic diffraction peak of CuO in the XRD spectrum of catalyst E indicates that the crystallite sizes present in this

material have small particle sizes below the detection limits of XRD or in non-crystalline form. The absence of Bragg peaks of iron, titanium, zirconium and tin in all the diffractograms of all the catalyst samples shows that they are either in an amorphous state or in a small concentration below the detection limit of XRD.

Table 5.2: Textural properties of catalyst samples

Samples	Specific surface area (m ² /g)		Pore volume (cm ³ /g)		Pore diameter (nm)		Crystallite size (nm)
	Fresh catalyst	Used catalyst	Fresh catalyst	Used catalyst	Fresh catalyst	Used catalyst	Fresh catalyst
SiO ₂ -Al ₂ O ₃ (A)	660	-	0.94	-	5.0	-	-
Fe(3)-Cu(13)/SiO ₂ -Al ₂ O ₃ (B)	434	-	0.59	-	4.2	-	6.4
Ti(1)-Fe(3)-Cu(13)/SiO ₂ -Al ₂ O ₃ (C)	443	441	0.49	0.48	4.3	4.2	7.2
Zr(1)-Fe(3)-Cu(13)/SiO ₂ -Al ₂ O ₃ (D)	465	462	0.55	0.55	4.4	4.3	7.2
Sn(1)-Fe(3)-Cu(13)/SiO ₂ -Al ₂ O ₃ (E)	571	571	0.65	0.64	4.4	4.3	5.1
Sn(0.5)-Fe(3)-Cu(13)/SiO ₂ -Al ₂ O ₃ (F)	465	464	0.54	0.54	4.2	4.2	7.4
Sn(2)-Fe(3)-Cu(13)/SiO ₂ -Al ₂ O ₃ (G)	452	450	0.51	0.50	4.3	4.2	6.3

The mean crystallite sizes of CuO and Cu₂O phases evaluated from the XRD patterns of all the catalyst samples are shown in Table 5.2. The crystallite size of catalyst B increased from 6.4 nm to 7.2 nm after impregnation of both 1 wt.% Ti and 1 wt.% Zr. The impregnation of 1 wt.% Sn resulted in a decrease in the crystallite size of the base catalyst from 6.4 nm to 5.1 nm. The crystallite size of the 0.5, 1 and 2 wt.% of tin-promoted catalysts were 7.1 nm, 5.1 nm and 6.3 nm, respectively. Catalyst E had the lowest average crystallite size when compared with other tin, titanium and zirconium promoted catalysts. This implies that this catalyst would have the highest metal dispersion. In comparison with the textural properties obtained from N₂ physisorption analysis, catalyst E had the highest surface area (571 m²/g), highest pore volume (0.65 cm³/g) and lowest average crystallite size (5.1 nm).

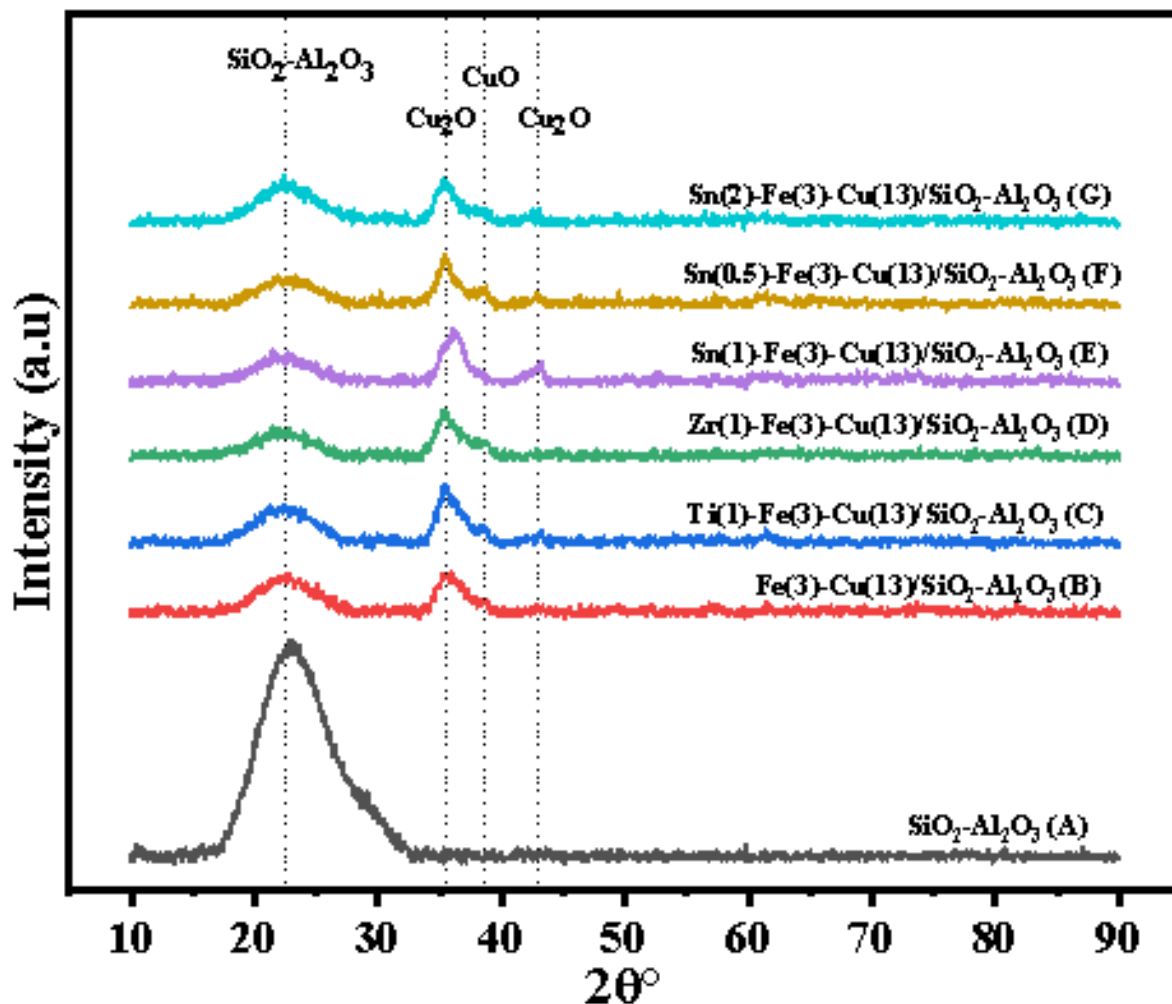


Figure 5.2: XRD patterns of support, base catalyst and Ti, Zr and Sn supported catalysts

CasaXPS software was used to deconvolute Cu 2p, Fe 2p, Sn 3d, Ti 2p and Zr 3d in catalysts C, D, E, F and G as depicted in Fig. 5.3. The oxidized and reduced phases of copper, iron, zirconium, tin and titanium were identified in catalyst samples. The XPS peaks of Cu 2p_{1/2}, Fe 2p_{1/2}, Sn 3d_{5/2}, Zr 3d_{5/2} and Ti 2p_{3/2} were observed at 931-935 eV, 706-712 eV, 482-487 eV, 177-181 eV and 455-458 eV, respectively. The oxidized and reduced phases of all the metals in all the catalyst samples were quantified in terms of atomic compositions and presented in Table 5.3. Cu₂O phases have the highest atomic compositions in the copper phases of all the catalyst samples. This corroborates the intense Cu₂O diffraction peak observed in the XRD diffractograms of all the catalysts in Fig. 5.2. The atomic composition of the CuO phase obtained from the XPS fitting of catalyst E was 9.6%. This was the lowest in comparison with other catalyst samples. This

confirmed the observation from its XRD patterns, i.e. a small quantity below the XRD detection limit. Catalyst F has the lowest atomic composition of oxophilic reduced Fe (25.5%), while the highest atomic composition of reduced Fe of 56.4% was recorded from the XPS deconvolution of catalyst E (Mayer et al. 1995; Guillot et al. 2001; Roustilla et al. 2003; Xiao et al. 2012; Gao et al. 2013; Wang et al. 2014; Dubale et al. 2016; Manikandan et al. 2016). This observation explains the superior hydroxygenation performance of catalyst E in the hydroprocessing of oleic acid as compared to its counterpart.

The functional groups present in support A and catalysts B to G are depicted in the FTIR transmittance region between 400 and 1600 cm^{-1} (Fig. 5.4). The 453 cm^{-1} , 800 cm^{-1} and 1053 cm^{-1} absorption bands are attributed to SiO_2 linkages bending (Si–O) vibrations, $\text{SiO}_2\text{–Al}_2\text{O}_3$ linkages vibration (Al–O–Si) and stretching of silica linkages (Si–O), respectively (Hosseinpour et al. 2017; Shalaby et al. 2018). The intensity of absorption bands ascribed to silica linkages is in the order of support A > bimetallic catalyst B > trimetallic catalysts due to the ratio of the content of silica-alumina in all the samples. There was no shift in the wavenumber of the Si–O bend, Si–O stretch and Al–O–Si vibration after metals impregnation indicating no appreciable change in the length of Si–O and Al–O–Si bonds in the silica-alumina framework (Hosseinpour et al. 2017; Shalaby et al. 2018).

The profiles of H_2 -TPR of catalyst B to G are depicted in Fig. 5.5. The reduction peaks in all the profiles can be attributed to the CuO reduction, while the hump above 350°C is attributed to iron oxides reduction to reduced iron (Xiao et al., 2012). The revelations from XRD and XPS analyses that catalyst samples contain copper oxides despite the reduction of all the samples during catalysts preparation are confirmed from the TPR profile of the catalyst samples. The peak temperature of reduction from the profiles of the TPR of the catalyst samples is in the order of catalyst F > C > D > G > E as shown in Fig. 5.5 and Table 5.4. This is akin to the trend of crystallite size of catalysts shown in Table 5.2. Low crystallite size indicates high metal dispersion, while low reduction TPR peaks indicate a weak metal–support interaction (Sheng et al., 2016). H_2 uptake from TPR analysis of the catalyst samples is shown in Table 5.4. The highest H_2 uptake was reported for catalyst G and attributed to the electronic state of the active sites as shown in Table 5.3. Catalyst G has a high atomic composition of iron oxides and copper oxides as compared to the other four catalysts.

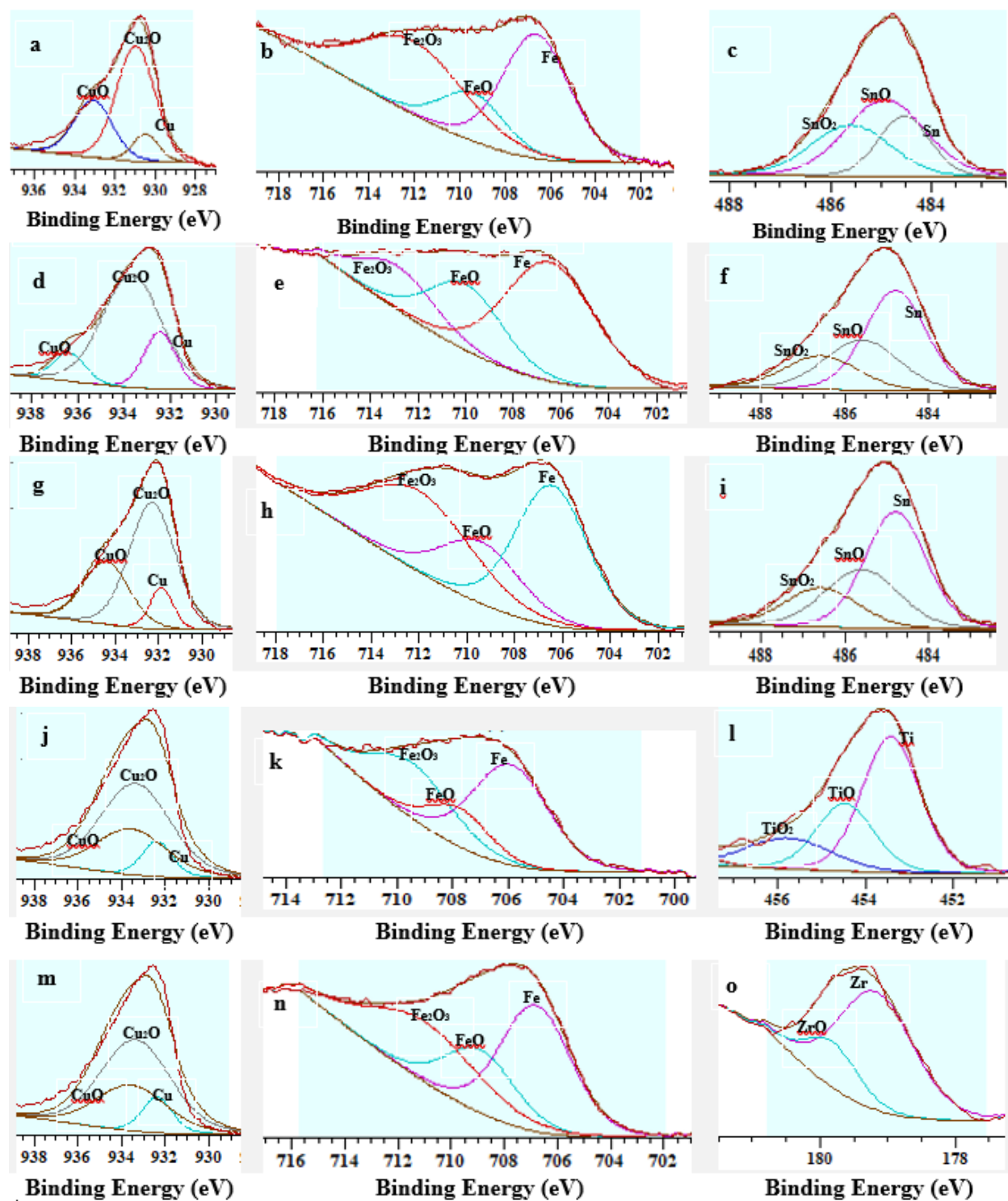


Figure 5.3: XPS spectra of 0.5 wt.% Sn (a-c), 1 wt.% Sn (d-f), 1 wt.% Sn (g-i), 1 wt.% Ti (j-l) and 1 wt.% Zr (m-o) supported catalysts

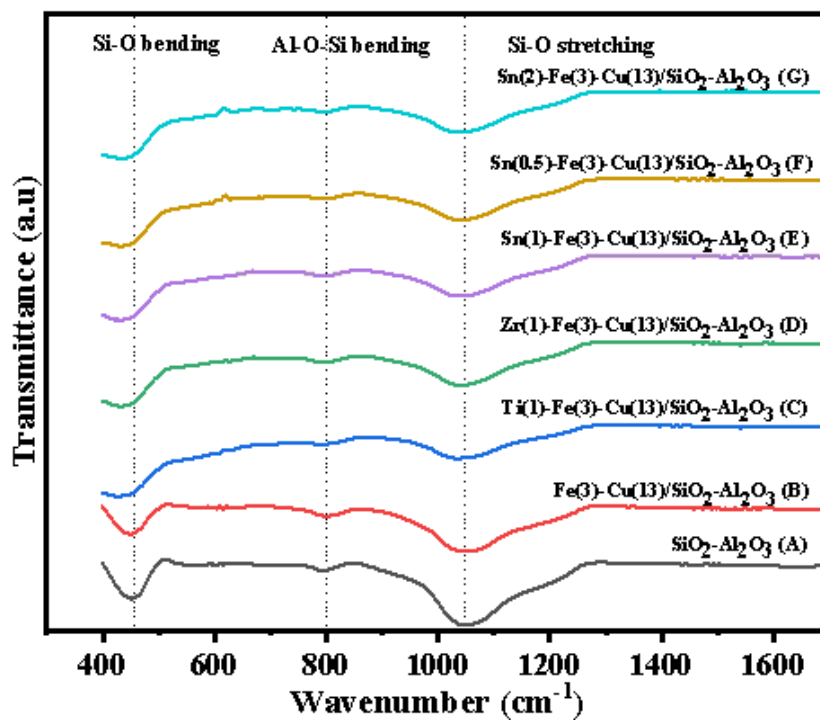


Figure 5.4: FTIR spectra of support, base catalyst and Ti, Zr and Sn supported catalysts

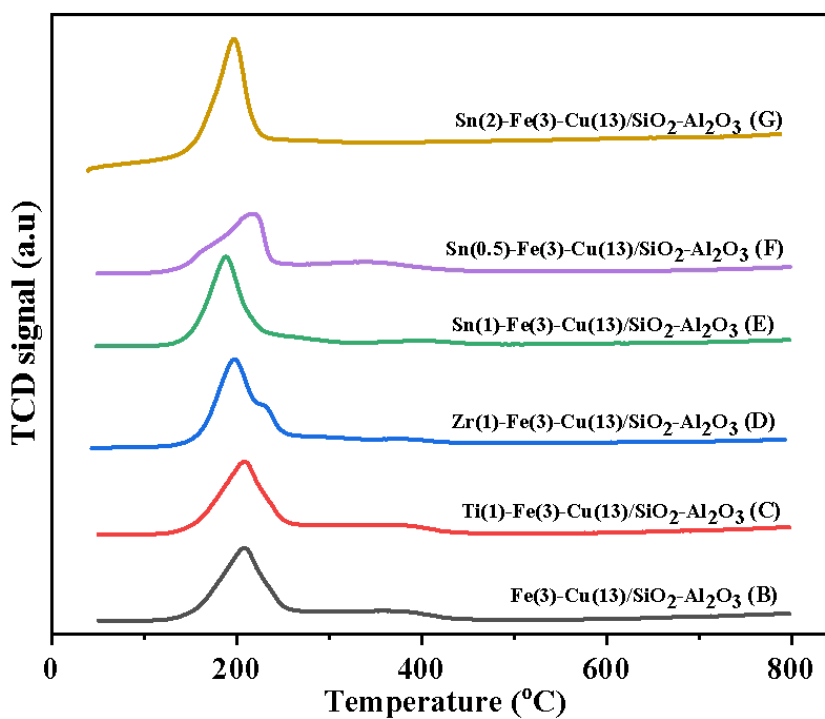


Figure 5.5: TPR profiles of base catalyst and Ti, Zr and Sn supported catalysts

Table 5.3: XPS deconvolution results of catalyst samples

Catalyst samples	Atomic composition (%)						
	Cu	Cu ₂ O	CuO	Fe	FeO	Fe ₂ O ₃	Other metals
Ti(1)-Fe(3)-Cu(13)/SiO ₂ -Al ₂ O ₃ (C)	10.0	60.0	30.0	52.4	31.1	16.5	Ti: 54.2, TiO: 27.1, TiO ₂ : 18.7
Zr(1)-Fe(3)-Cu(13)/SiO ₂ -Al ₂ O ₃ (D)	45.2	41.5	13.3	44.4	22.2	33.4	Zr: 78.8, ZrO: 21.2
Sn(1)-Fe(3)-Cu(13)/SiO ₂ -Al ₂ O ₃ (E)	19.3	71.1	9.6	56.4	26.0	17.6	Sn: 49.8, SnO: 30.1, SnO ₂ : 20.1
Sn(0.5)-Fe(3)-Cu(13)/SiO ₂ -Al ₂ O ₃ (F)	9.7	60.2	30.1	43.4	16.1	40.5	Sn: 35.5, SnO: 38.5, SnO ₂ : 25.7
Sn(2)-Fe(3)-Cu(13)/SiO ₂ -Al ₂ O ₃ (G)	9.9	60.1	30.0	42.5	20.9	36.6	Sn: 36.2, SnO: 24.1, SnO ₂ : 39.7

Table 5.4: H₂ uptake and reduction peak temperatures of catalyst samples

Catalyst samples	Reduction peak temperature (°C)	H ₂ uptake (mmol/g.cat)
Fe(3)-Cu(13)/SiO ₂ -Al ₂ O ₃ (B)	207	3.1
Ti(1)-Fe(3)-Cu(13)/SiO ₂ -Al ₂ O ₃ (C)	208	3.2
Zr(1)-Fe(3)-Cu(13)/SiO ₂ -Al ₂ O ₃ (D)	196	3.4
Sn(1)-Fe(3)-Cu(13)/SiO ₂ -Al ₂ O ₃ (E)	191	3.5
Sn(0.5)-Fe(3)-Cu(13)/SiO ₂ -Al ₂ O ₃ (F)	216	3.1
Sn(2)-Fe(3)-Cu(13)/SiO ₂ -Al ₂ O ₃ (G)	194	3.7

Lewis and Brønsted acid sites of catalyst samples were determined by using acetonitrile, ammonia or pyridine as a molecular probe. A clear distinction between Lewis and Brønsted sites was achieved with the application of pyridine as a molecular probe, as described elsewhere (Barzetti et al., 1996). Catalysts with high ratios of Brønsted/Lewis acidity are selective for cracking, but they do not favor dehydrogenation (Ma et al., 2018). For the production of ATF range hydrocarbons via oleic acid hydroprocessing, cracking is required to produce carbon compounds within the C₈-C₁₆ aviation turbine fuel range hydrocarbons (Ayandiran et al., 2019). The Lewis acidity of a metal ion has a direct relationship with its electronegativity and oxidation state (Boffa et al., 1994). Using Pauling's scale of electronegativity, the order of electronegativity of tin, titanium and zirconium promoters is Sn > Ti > Zr. The Lewis acidity of catalyst G as shown in Table 5.5 is the highest as compared to catalyst C and D. The low Lewis acidity of catalyst E and F are attributed to its low atomic composition of SnO₂ component as revealed from XPS

deconvolution in Table 5.3. The low Brønsted acidity of the catalysts as compared to the silica-alumina support is attributed to a slight replacement of the Brønsted acid sites on the catalyst surface. The ratio of Brønsted/Lewis acidity was obtained from the pyridine-FTIR spectra of the catalysts as explained in our previous work (Ayandiran et al., 2019). The ratios of Brønsted/Lewis acidity obtained from the pyridine-FTIR analysis were within a short range of 2-2.8 as shown in Table 5.5 because SiO₂-Al₂O₃ support has more impact on the acidity of the catalyst than the loaded metals. The highest ratio of Brønsted/Lewis acidity of 2.8 was recorded for catalyst E.

The optimum impeller speed was determined with agitation speed within the range of 300-600 rpm at 320°C for 8 h under 2.1 MPa H₂ pressure over catalyst E as shown in Table 5.6. An increase in the selectivity of ATF range hydrocarbons and oleic acid conversion from 300-500 rpm impeller speed and its later stability from 500 to 600 rpm indicate that mass transfer control becomes less significant. The selectivity of ATF range hydrocarbons and oleic acid conversion reached their peak at 500 rpm. Therefore, increasing the agitation speed beyond 500 rpm was not required for the reaction.

5.4.2 Catalytic evaluation

Catalyst evaluation was carried out in triplicates. The mean and standard error of selectivity of aviation turbine fuel range hydrocarbons and oleic acid conversion obtained from the hydroprocessing of oleic acid within 8 h of reaction time and 300-340°C over catalyst C, D and E are shown in Fig. 6-8. The selectivity of aviation turbine fuel range hydrocarbons over catalyst E, F and G are shown in Table 5.7. The oleic acid conversion recorded from the evaluation of catalyst C increased from 2 h to 8 h (Fig. 5.6). At 320°C and 340°C, it stabilized at about 95% and 96%, respectively. The highest aviation turbine fuel range hydrocarbons selectivity recorded over catalyst C as shown in Fig. 6 was 60.5% at 340°C and 6 h. In the case of catalyst D, the conversion of oleic acid increased with reaction time from 2 h to 8 h (Fig. 5.7). At 320°C and 340°C, it stabilized at about 92% and 93%, respectively. The highest aviation turbine fuel range hydrocarbons selectivity recorded from the evaluation of catalyst D as shown in Fig. 5.7 was 70.1% at 340°C and 6 h. The highest selectivity of aviation turbine fuel range hydrocarbons achieved with the evaluation of catalyst F was 53.3 % as shown in Table 5.7 at 320°C and 6 h. The low selectivity of aviation turbine fuel range hydrocarbons obtained over catalyst F is attributed to its low crystallite size evaluated from its XRD pattern and relatively strong metal-support interaction indicated from TPR analysis. The highest selectivity of aviation turbine fuel range hydrocarbons

recorded from the evaluation of catalyst G for hydroprocessing reaction was 73.9% after 4 h (Table 5.7). The hydroprocessing of oleic acid over catalyst E gave its highest oleic acid conversion at 97% after 8 h of reaction time and 340°C of the reaction temperature as depicted in Fig. 5.8. The highest aviation turbine fuel range hydrocarbons selectivity recorded with this catalyst E was 76.8% after 8 h at 320°C, i.e. the most selective catalyst for aviation turbine fuel range hydrocarbons is the 1 wt.% tin-promoted catalyst.

It is noteworthy to mention that Sn promotes oxygen abstraction from oleic acid in the form of hydrogenolysis of C–O and C=O bonds. That notwithstanding, an excess of Sn can inhibit cracking (Zavelev et al., 2020). The increase in the selectivity of aviation turbine fuel range hydrocarbons from 47.6 wt.% to 76.8% due to an increase in loading of Sn promoter from 0.5 wt.% to 1 wt.% Sn at 320°C, 2.1 MPa H₂ pressure and 8 h reaction time as shown in Table 5.7 are attributed to the increase in the power of hydrogenolysis of the C–O and C=O bonds of oleic acid. The decrease in the selectivity of aviation turbine fuel range hydrocarbons from 76.8% to 54.1% due to an increase in the loading of Sn-promoter from 1 wt.% to 2 wt.% at 320 °C, 2.1 MPa H₂ pressure and 8 h reaction time are ascribed to inhibition of cracking of oleic acid (C₁₈) to aviation turbine fuel range hydrocarbons (C₈-C₁₆) due to excess loading of Sn promoter.

The hydrocarbon distributions in the liquid product obtained from the evaluation of catalyst C, D, E, F and G at 320°C in 8 h are shown in Table 5.8. Catalyst E recorded the highest yield of 71.7% due to its high BET surface area of 571 m²/g, the high pore volume of 0.65 cm³/g, greater oxophilic reduced iron of 56.4%, the lower crystallite size of 5.1 nm and weak metal–support interaction, thus indicating efficient metal dispersion. Catalyst E has the highest yield of C₅-C₇ hydrocarbons of 11.6% and the lowest yield of C₁₇-C₁₈ hydrocarbons of 10.1% as shown in Table 5.5 due to its relatively high ratio of Brønsted/Lewis acid sites of 2.8 from pyridine-FTIR analysis, which favors cracking (Ayandiran et al., 2019). The hydrocarbon distributions in terms of individual hydrocarbons from C₈-C₁₆ are shown in Table 5.9.

The percentage composition of the aromatics in the product was also analyzed for each of the catalyst samples at 320°C in 8 h (Table 5.8). Low aromatic contents were obtained in the range of 0.9-2% for all the catalyst samples. Catalyst E has the lowest aromatic content (0.9%) while catalyst B has the highest aromatic content (2%). This trend can be ascribed to their Brønsted/Lewis acidity ratio. Catalysts with a low ratio of Brønsted/Lewis acidity favor the production of aromatics (Ruling et al., 2015).

Table 5.5: Amount of Brønsted and Lewis acid sites from pyridine-FTIR analysis

Samples	Lewis acid sites ($\mu\text{mol/g}$)	Bronsted acid sites ($\mu\text{mol/g}$)	Brønsted/Lewis acid sites ratio
SiO ₂ -Al ₂ O ₃ (A)	16.7	43.5	2.6
Ti(1)-Fe(3)-Cu(13)/SiO ₂ -Al ₂ O ₃ (C)	16.5	43.0	2.6
Zr(1)-Fe(3)-Cu(13)/SiO ₂ -Al ₂ O ₃ (D)	16.0	43.2	2.7
Sn(1)-Fe(3)-Cu(13)/SiO ₂ -Al ₂ O ₃ (E)	15.5	43.4	2.8
Sn(0.5)-Fe(3)-Cu(13)/SiO ₂ -Al ₂ O ₃ (F)	15.9	42.9	2.7
Sn(2)-Fe(3)-Cu(13)/SiO ₂ -Al ₂ O ₃ (G)	16.9	33.8	2.0

Table 5.6: Effect of impeller speed on oleic acid conversion and selectivity of jet fuel range hydrocarbons at 320°C and 2.1 MPa H₂ pressure over 1 wt.% Sn supported catalyst

Impeller Speed (rpm)	Oleic acid conversion (%)	Selectivity of jet fuel range hydrocarbons (%)
300	90±2	74±2
400	91±1	75±1
500	93±1	77±1
600	93±2	77±1

Fig. 5.9 illustrates the relationship between the crystallite size of each catalyst and their aviation turbine fuel range hydrocarbons yield at 320°C and 6 h. 0.5 wt.% tin-promoted trimetallic catalyst had the highest crystallite size (7.4 nm) and gave the lowest yield of aviation turbine fuel range hydrocarbons (35%). On the other hand, 1 wt.% tin-promoted catalyst has the lowest crystallite size (5.1 nm) and the highest yield of aviation turbine fuel range hydrocarbons (72%). The yield of aviation turbine fuel range hydrocarbons of the base catalyst B was improved with the use of 1 wt.% each of Ti, Zr and Sn as promoters from 53.7% to 54.7%, 61.1% and 71.7%, respectively. The evaluation of 0.5 and 1 wt.% of tin-promoted trimetallic catalyst gave 35% and 50.4% yield of aviation turbine fuel range hydrocarbons, respectively. The promising performance of optimized 1 wt.% Sn was attributed to its low crystallite size, weak metal-support interactions as well as its desirable textural properties. The evaluation of catalyst F and E gives 35% and 50.4% yield of aviation turbine fuel range hydrocarbons, respectively.

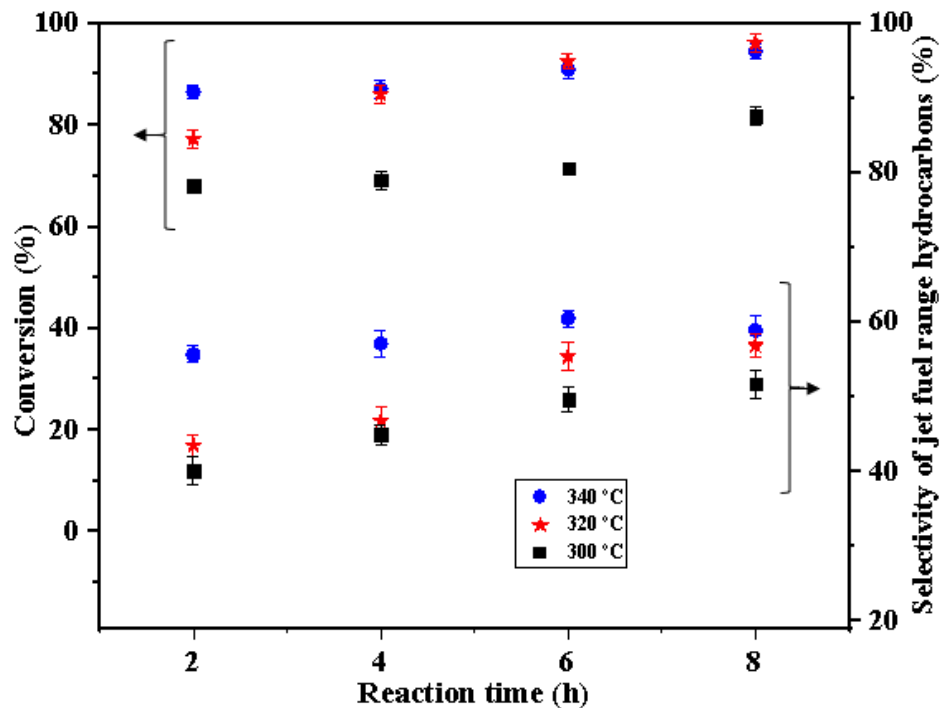


Figure 5.6: Oleic acid conversion and selectivity of jet fuel range hydrocarbons at 300-340°C and 2.1 MPa H₂ pressure over 1 wt.% Ti-supported catalyst

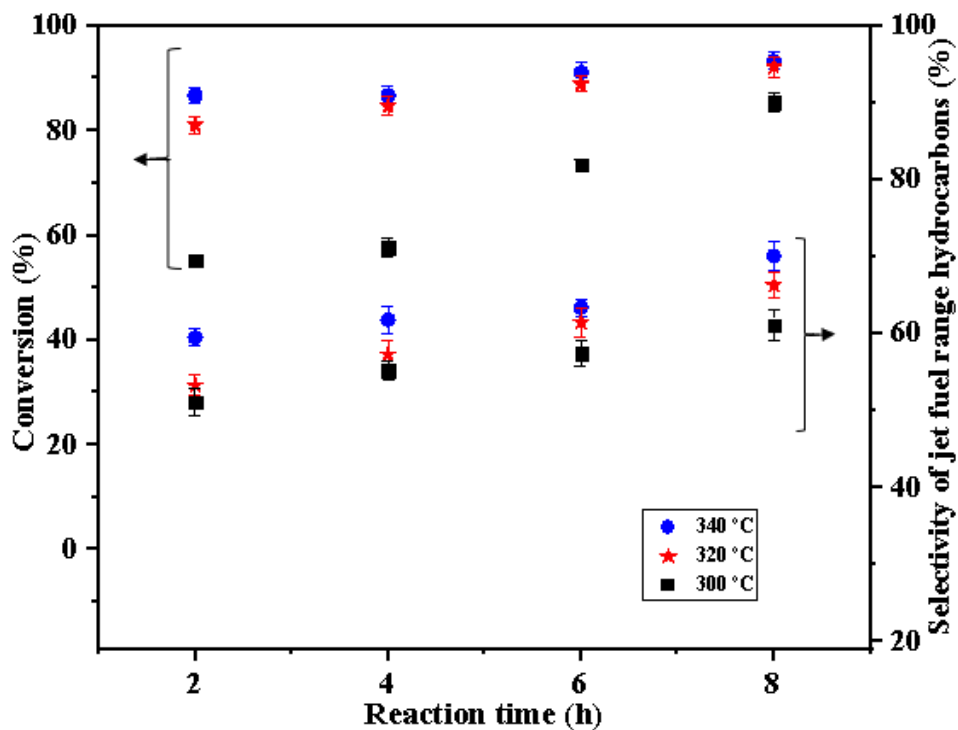


Figure 5.7: Oleic acid conversion and selectivity of jet fuel range hydrocarbons at 300-340°C and 2.1 MPa H₂ pressure over 1 wt.% Zr-supported catalyst

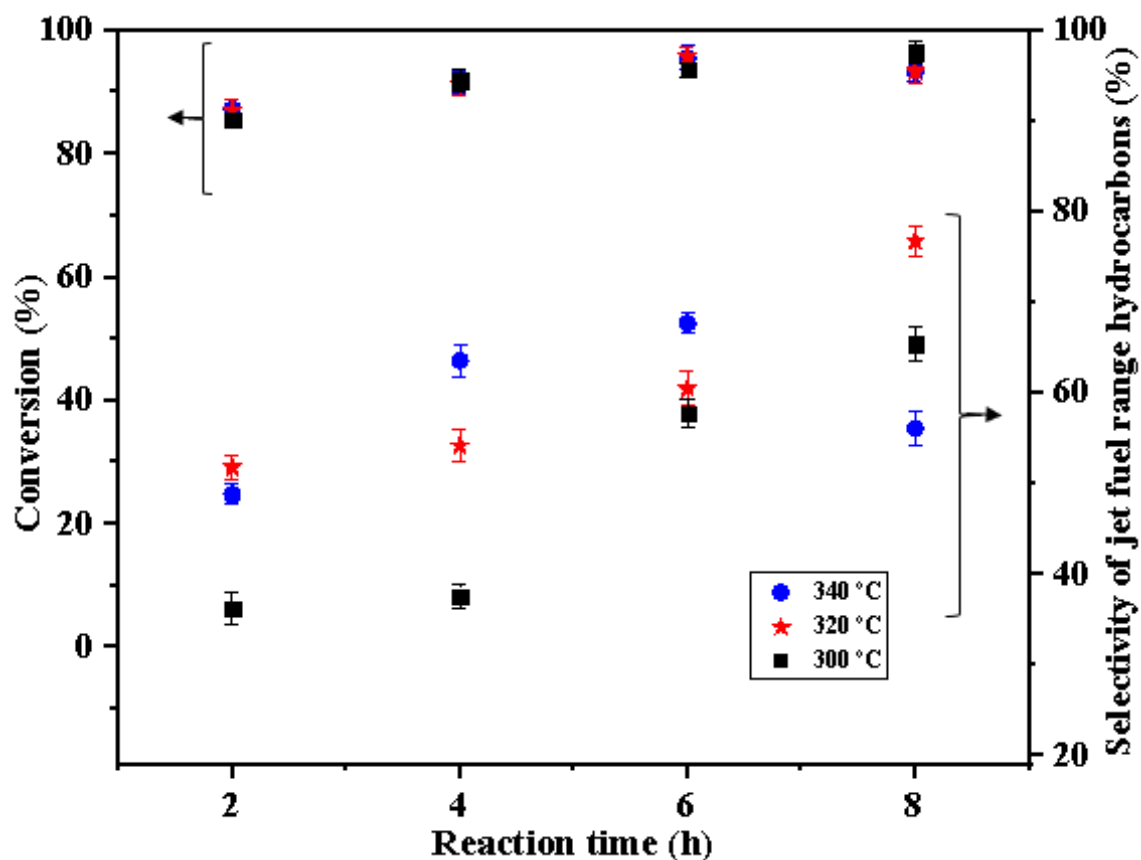


Figure 5.8: Oleic acid conversion and selectivity of jet fuel range hydrocarbons at 300-340°C and 2.1 MPa H₂ pressure over 1 wt.% Sn-supported catalyst

Table 5.7: Selectivity of C₈–C₁₆ hydrocarbons at different temperatures (300-340°C) and reaction time (2-8 h) under 2.1 MPa H₂ pressure

Catalyst Samples	Temperature (°C)	Reaction time (h)			
		2	4	6	8
Sn(0.5)-Fe(3)-Cu(13)/SiO ₂ -Al ₂ O ₃ (F)	300	20.7	21.2	28.5	25.5
	320	30.2	34.3	53.3	47.6
	340	35.2	40.4	42.2	35.3
Sn(1)-Fe(3)-Cu(13)/SiO ₂ -Al ₂ O ₃ (E)	300	36.2	37.6	57.7	65.4
	320	51.2	54.2	60.5	76.8
	340	48.8	63.6	67.7	56.1
Sn(2)-Fe(3)-Cu(13)/SiO ₂ -Al ₂ O ₃ (G)	300	64.7	65.2	54.7	47.3
	320	69.2	70.8	66.2	54.1
	340	72.4	73.9	69.5	54.1

Table 5.8: Product distribution of hydrocarbons at 320°C in 8 h under 2.1 MPa H₂ pressure

Catalyst samples	C ₅ -C ₇	C ₈ -C ₁₆ (jet fuel range hydrocarbons)	C ₁₇ -C ₁₈	Aromatics
	Yield (%)			
Fe(3)-Cu(13)/SiO ₂ -Al ₂ O ₃ (B)	6.7	53.7	34.1	2.0
Ti(1)-Fe(3)-Cu(13)/SiO ₂ -Al ₂ O ₃ (C)	9.9	54.7	31.6	1.6
Zr(1)-Fe(3)-Cu(13)/SiO ₂ -Al ₂ O ₃ (D)	10.8	61.1	20.3	1.5
Sn(1)-Fe(3)-Cu(13)/SiO ₂ -Al ₂ O ₃ (E)	11.6	71.7	10.1	0.9
Sn(0.5)-Fe(3)-Cu(13)/SiO ₂ -Al ₂ O ₃ (F)	10.9	35.0	27.7	1.5
Sn(2)-Fe(3)-Cu(13)/SiO ₂ -Al ₂ O ₃ (G)	7.5	50.4	35.3	1.9

Table 5.9. Selectivity of C₈-C₁₆ hydrocarbons at 320°C in 8 h under 2.1 MPa H₂ pressure

Catalysts	Product Distribution (%)								
	C ₈	C ₉	C ₁₀	C ₁₁	C ₁₂	C ₁₃	C ₁₄	C ₁₅	C ₁₆
Ti(1)-Fe(3)-Cu(13)/SiO ₂ -Al ₂ O ₃ (C)	6.1	5.6	4.9	6.9	7.1	8.1	5.8	6.8	5.6
Zr(1)-Fe(3)-Cu(13)/SiO ₂ -Al ₂ O ₃ (D)	7.6	7.2	6.8	7.8	7.6	7.2	6.5	7.4	8.3
Sn(1)-Fe(3)-Cu(13)/SiO ₂ -Al ₂ O ₃ (E)	7.5	8.6	9.0	8.5	9.5	7.4	9.2	8.2	8.9
Sn(0.5)-Fe(3)-Cu(13)/SiO ₂ -Al ₂ O ₃ (F)	5.1	5.4	6.3	4.8	6.2	5.1	6.7	5.2	2.8
Sn(2)-Fe(3)-Cu(13)/SiO ₂ -Al ₂ O ₃ (G)	5.4	6.5	6.3	5.8	5.4	6.3	5.3	6.8	6.3

It should be noted that Cu⁺ in the active site of the catalyst has a high strength of adsorption and activation of hydrogen and carboxyl compounds. Of all the five catalysts, 1 wt.% Sn-promoted catalyst has the highest atomic composition of Cu₂O (71.1%) as indicated from XPS deconvolution results of the catalyst as shown in Table 5.3. Hence, the high yield of aviation turbine fuel range hydrocarbons over 1 wt.% Sn-promoted catalysts are also attributed to its high atomic composition of Cu₂O revealed from XPS analysis.

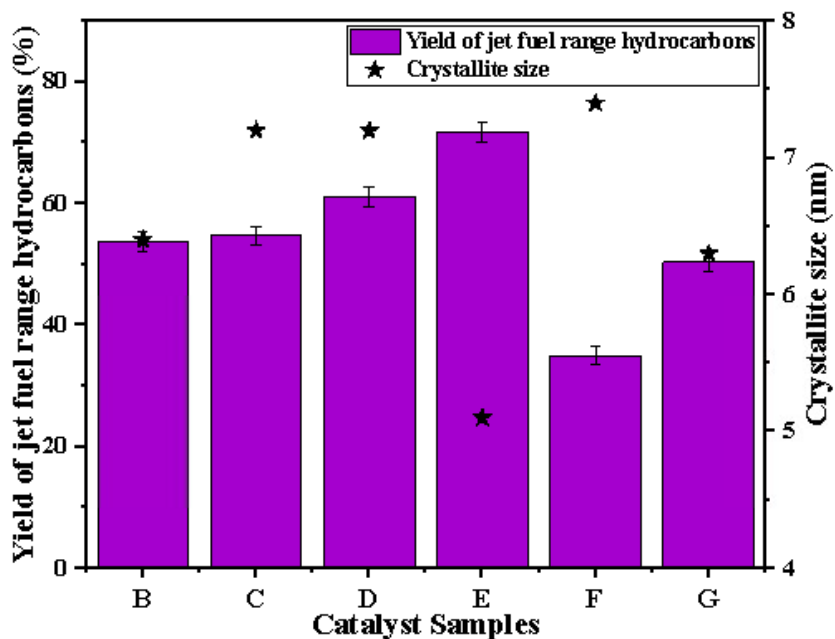


Figure 5.9: Yield of jet fuel range hydrocarbons at 320°C, 8 h and 2.1 MPa H₂ pressure over crystallite size of base catalyst (B), 1 wt.% Ti (C), 1 wt.% Zr (D), 1 wt.% Sn (E), 0.5 wt.% Sn (F) and 2 wt.% Sn (G) supported catalyst

Catalyst productivity was calculated in terms of the grams of jet fuel per gram of catalyst per hour as shown in Table 5.10. This was calculated to determine the performance of all the catalysts per unit mass of catalyst and unit time. Of all the 1 wt.% Ti, Zr and Sn supported catalysts, the lowest productivity was recorded at 300°C over 1 wt.% Ti. The performance of 1 wt.% Ti-supported catalyst was attributed to its low BET surface area of 443 m²/g and low pore volume of 0.49 cm³/g as compared to the BET surface area and pore volume of 1 wt.% Sn and 1 wt.% Zr supported catalysts. The low catalyst productivity of 1 wt.% Ti supported catalyst when compared to the performance of 1 wt.% Zr and 1 wt.% Sn-promoted catalysts were attributed to its relatively strong metal–support interaction indicated from TPR analysis. The 1 wt.% Sn-supported catalyst has the highest catalyst productivity of 1.6 g jet fuel/(g catalyst)/h when compared to the performance of 1 wt.% Ti and 1 wt.% Zr. This promising performance is attributed to its relatively high pore volume, high BET surface area and weak metal–support interaction indicated from TPR analysis. The catalyst productivity of all the tin-promoted trimetallic catalysts in terms of grams of jet fuel per gram of catalyst per hour at 320°C was in the order of catalyst F < G < E. The high productivity of 1 wt.% Sn-supported catalyst is attributed to its relatively weak metal–support interaction, high pore volume and high surface area.

Table 5.10: Catalysts productivity towards C₈-C₁₆ hydrocarbons at 300-340°C in 8 h under 2.1 MPa H₂ pressure

Catalyst samples	Temperature (°C)	g jet fuel/g catalyst/h
Ti(1)-Fe(3)-Cu(13)/SiO ₂ -Al ₂ O ₃	300	0.9
	320	1.2
	340	1.2
Zr(1)-Fe(3)-Cu(13)/SiO ₂ -Al ₂ O ₃	300	1.1
	320	1.3
	340	1.4
Sn(1)-Fe(3)-Cu(13)/SiO ₂ -Al ₂ O ₃	300	1.4
	320	1.6
	340	1.1
Sn(0.5)-Fe(3)-Cu(13)/SiO ₂ -Al ₂ O ₃	300	0.4
	320	0.8
	340	0.6
Sn(2)-Fe(3)-Cu(13)/SiO ₂ -Al ₂ O ₃	300	0.9
	320	1.1
	340	1.1

The longevity test was carried out over the promising catalyst, 1 wt.% Sn-supported catalyst in a 150 h long-duration reaction. The reusability test was done with an additional six reaction cycles of 8 h reaction time each. The hydroprocessing reaction was conducted at the operating condition with the highest catalytic performance (320°C and 2.1 MPa of H₂ pressure). Fig. 10 illustrates the time dependence of the selectivity of aviation turbine fuel range hydrocarbons and oleic acid conversion, while Fig. 5.11 shows the reusability test of the catalyst in terms of oleic acid conversion and selectivity of aviation turbine fuel range hydrocarbons. The two figures depicted no considerable change in the activity and selectivity of the promising catalyst after 150 h reaction time and after six reaction cycles of 8 h reaction time each. This shows that the 1 wt.% Sn-supported catalyst has high stability during the HDO reaction. The stability of 1 wt.% Sn-promoted catalyst can be attributed to the insignificant change in the textural properties of the used catalyst as shown in Table 5.2.

The comparison of the performance of 1 wt.% Sn-supported catalyst with other catalysts used for the production of aviation turbine fuel range hydrocarbons is shown in Table 5.11. Feng et al (2019) evaluated an ultrathin Ni/ZSM-5 catalyst for the production of aviation turbine fuel range hydrocarbons via oleic acid hydroprocessing to obtain 41.4% yield of aviation turbine fuel

range hydrocarbons at 250°C. Scaldaferrri et al. (2019) reported a 58% yield of aviation turbine fuel range hydrocarbons with the application of niobium phosphate (NbOPO₄) catalyst. and Kim et al (2017) and Chang et al (2019) obtained 51 and 55% yield of aviation turbine fuel range hydrocarbons, respectively over Ni/meso- γ zeolite and Pt/nano- β -zeolite catalysts. In our previous work, a bimetallic catalyst consisting of 13 wt.% Cu and 3 wt.% Fe supported on SiO₂-Al₂O₃ was evaluated for hydroprocessing of oleic acid to obtain a 60% yield of aviation turbine fuel hydrocarbon. In this present study, 72% yield of aviation turbine fuel range hydrocarbons was realized from the screening of a trimetallic catalyst consisting of 1 wt.% Sn, 13 wt.% Cu and 3 wt.% Fe supported on SiO₂-Al₂O₃. The 1 wt.% Sn-supported catalyst had the highest selectivity and yield of aviation turbine fuel. It appears to be the most productive catalyst in terms of the mass of aviation turbine fuel range hydrocarbons produced per g of catalyst and 1 h of reaction time; hence very attractive for scale-up and practical pilot plant applications for the HDO of oleic acid and waste vegetable oils.

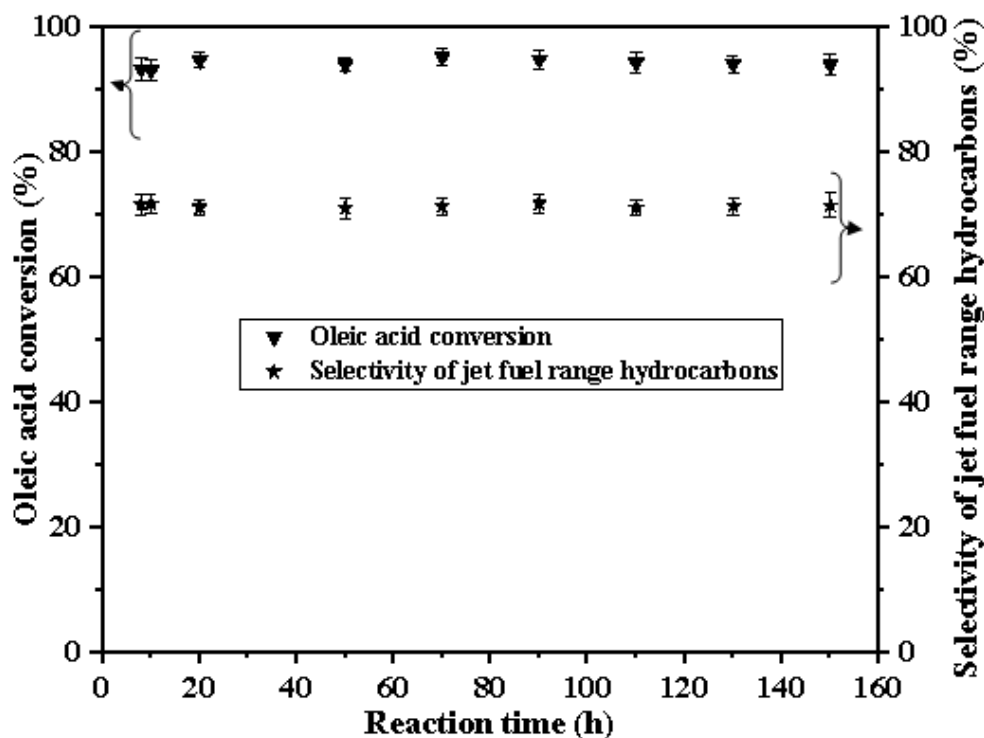


Figure 5.10: Longevity test showing Oleic acid conversion and selectivity of jet fuel range hydrocarbons at 320°C, 8-150 h and 2.1 MPa H₂ pressure over 1 wt.% Sn supported catalyst

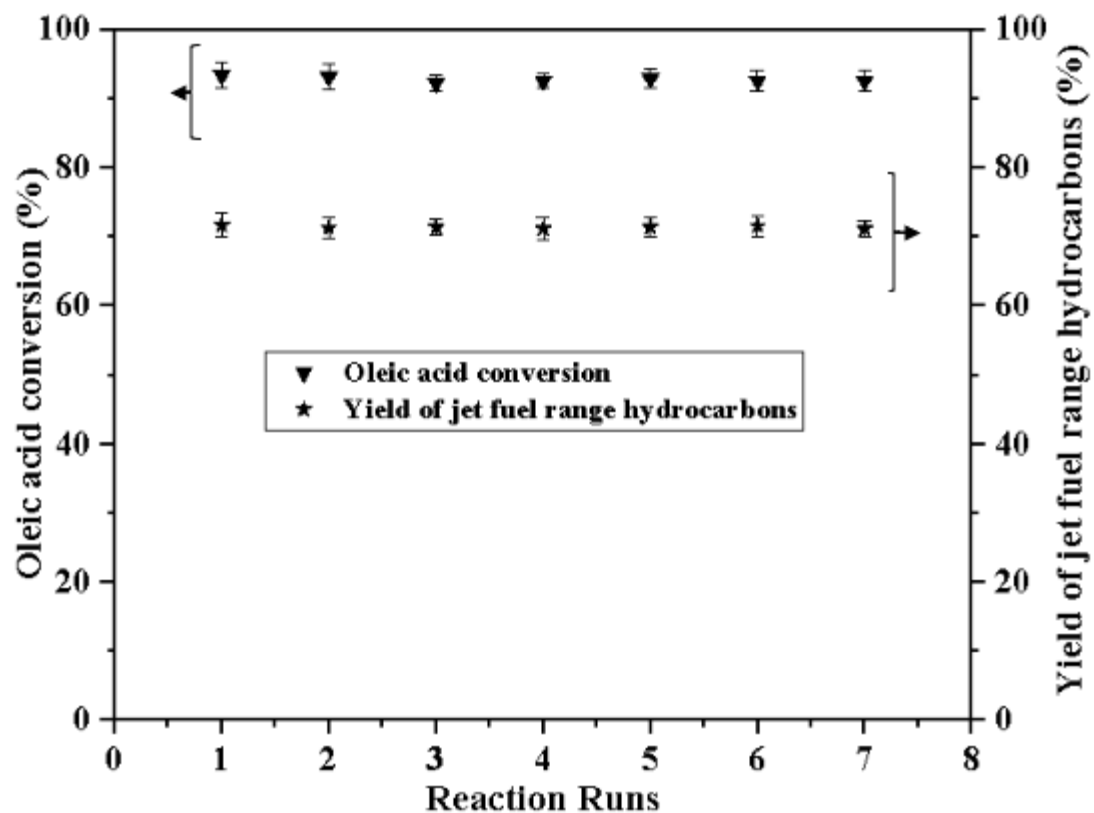


Figure 5.11: Reusability test showing Oleic acid conversion and yield of jet fuel range hydrocarbons at 320°C, 7 reaction runs and 2.1 MPa H₂ pressure over 1 wt.% Sn supported catalyst

Table 5.11: Comparison of the performance of 1 wt.% Sn-supported catalyst with other catalysts evaluated for jet fuel range hydrocarbons from literature

Catalysts	Reaction temperature (°C)	Yield (%)	References
Ni/ZSM-5	250	41.4	Feng et al., 2019
NbOPO ₄	300	58	Scaldeferri et al., 2019
Ni/meso-γ zeolite	275	51	Cheng et al., 2019
Pt/nano-β zeolite	250	55	Kim et al., 2017
Fe(3)-Cu(13)/SiO ₂ -Al ₂ O ₃	300	60	Ayandiran et al., 2019
Sn(1)-Fe(3)-Cu(13)/SiO ₂ -Al ₂ O ₃	320	72	This study

5.5 Conclusions

In summary, the properties of Fe(3)-Cu(13)/SiO₂-Al₂O₃ were improved with 0.5, 1 and 2 wt.% of Sn and 1 wt.% Ti and Zr. The surface areas of 465, 571, 452, 443 and 465 m²/g were

obtained from the N₂-physisorption analysis of 0.5 wt. % Sn, 1 wt. % Sn, 2 wt.% Sn, 1 wt.% Ti and 1 wt.% Zr promoted catalysts, respectively. The crystallite sizes of 7.2 nm each were determined from the XRD analysis of catalyst 1 wt.% Ti and 1 wt.% Zr promoted catalysts, while 5.1, 7.4 and 6.3 nm were obtained as crystallite sizes for catalyst E, F and G, respectively. Catalyst E had the largest BET surface area, lowest crystallite size and the highest pore volume (0.65 cm³/g). The 1 wt.% tin-promoted trimetallic catalyst showed the lowest reduction peak temperature indicating weak metal–support interaction and high metal dispersion corroborating its crystallite size observations. Cu₂O phase was detected in the XRD diffractograms of all the five trimetallic catalyst samples, while the CuO phase was also detected in all the trimetallic catalyst samples except for catalyst E. All the reduced and oxidized phase of Cu, Fe, Ti, Sn, Zr were detected in their respective catalyst from XPS analysis with 1% Sn having the highest atomic composition of oxophilic reduced iron.

Among the five trimetallic catalysts studied, the 1 wt.% Sn-promoted catalyst exhibited the highest catalyst performance of 76.8% and 71.7% selectivity and yield of aviation turbine fuel range hydrocarbons, respectively. The optimum 1 wt.% Sn-promoter loading on Fe(3)-Cu(13)/SiO₂-Al₂O₃ gave the highest selectivity and yield of aviation turbine fuel range hydrocarbons, hence, being the most promising catalyst. The performance of this highly promising catalyst was due to its weak metal–support interaction and low crystallite size indicating high metal dispersion, high specific surface area, high pore volume and high oxophilic reduced iron determined from XPS analysis.

CHAPTER 6

Hydroprocessing of oleic acid for production of jet fuel range hydrocarbons over Sn(1)-Fe(3)-Cu(13)/SiO₂-Al₂O₃ catalyst: process parameters optimization, kinetics and thermodynamic study

The content of this chapter has been published in Asian Pacific Journal of Chemical Engineering as cited below:

Citation:

Ayandiran, AA, Boahene, PE, Dalai, AK, Hu, Y. Hydroprocessing of oleic acid for production of jet fuel range hydrocarbons over Sn(1)-Fe(3)-Cu(13)/SiO₂-Al₂O₃ catalyst: Process parameters optimization, kinetics, and thermodynamic study. *Asia-Pac J Chem Eng.* 10(2021)2621-2634.

Contribution of the Ph.D. Candidate

Synthesis, Characteristics and Evaluation of Catalyst, Optimization of process parameters, kinetics and thermodynamics were carried out by Afees A. Ayandiran in due consultation with Dr. Ajay K. Dalai and Dr. Yongfeng Hu. The manuscript was drafted and reviewed by Afees A. Ayandiran based on the guidance and suggestions provided by Dr. Ajay K. Dalai and Dr. Yongfeng Hu. Dr. Boahene Philip also assisted in reviewing the paper.

Contribution of this chapter to the overall PhD work

This chapter investigates the process parameters optimization, kinetics and thermodynamics over Sn(1)-Fe(3)-Cu(13)/SiO₂-Al₂O₃ catalyst for hydroprocessing of oleic acid for production of jet fuel range hydrocarbons.

6.1 Abstract

Hydroprocessing of vegetable oil to high quality jet fuel range hydrocarbons (HRJ) plays a significant role in the development of completely interchangeable substitute for conventional petroleum-derived jet fuel and has drawn the attention of aviation experts due to its capacity to mitigate greenhouse gas emissions associated with the aviation industry. The limited performance of 1 wt. % Sn promoted Fe(3)-Cu(13)/SiO₂-Al₂O₃ catalyst in our previous study has been attributed to the successive consideration of one variable at a time in its evaluation. Maximization of oleic acid conversion and selectivity of jet fuel range hydrocarbons from hydroprocessing of oleic acid over 1 wt. % Sn promoted Fe(3)-Cu(13)/SiO₂-Al₂O₃ catalyst with the best combination of the process parameters involved via multivariate approach and evaluation of kinetic and

thermodynamic activation parameters is the focus of this study. Reduced cubic oleic acid conversion model and reduced quadratic jet fuel range hydrocarbons selectivity model of high significance levels, adequate precision and high correlation coefficient were developed. Reaction temperature of 339.5 °C, 1.6 MPa H₂ pressure, 6.2 wt.% catalyst concentration and 8.0 h reaction time were optimum process parameters that can maximize oleic acid conversion and selectivity of jet fuel range hydrocarbons at 98.2 % and 82.2 %, respectively. This process was found to be endothermic, irreversible and non-spontaneous with 45.8kJ/mol activation enthalpy of reaction, 0.25kJ/mol entropy of reaction and the reaction's Gibb's free energy of 198.8kJ/mol at 340 °C. The minimum energy required for the reaction to take place was evaluated as 50.7kJ/mol.

6.2 Introduction

The aviation industry is a rapidly expanding sector, which connects businesses, cultures and people across the world. The world airlines transported 4.5 billion passengers and consumed 365 billion litres of jet fuel across the globe in 2019 (ATAG, 2020). In spite of the enormous significance of the aviation industry, its development has strong correlation with increase in the emission of greenhouse gases. In 2019, air transportation emitted 915 megatonnes of CO₂ globally (ATAG, 2020). These CO₂ emissions are the main cause of global climate change and ocean acidification. The international air transport association (IATA) targeted a long-term goal of 50% reduction of net carbon footprint from 2005 to 2050 for mitigation of greenhouse gas emissions (ICAO, 2020). According to the international civil aviation organization (ICAO), the development and deployment of renewable aviation fuels is the most effective emission-reduction strategies for achieving the long-term goal (ICAO, 2020, Sgourids et al., 2010). Bio-jet fuel researchers have explored different technologies for production of sustainable aviation fuels (Doliente et al., 2020). They include OTJ (oil to jet fuel), GTJ (gas to jet fuel), ATJ (alcohol to jet fuel) and STJ (sugar to jet fuel) (Doliente et al., 2020). Technoeconomic and life cycle analyses of jet fuel production have proven that the conversion of oil to jet fuel range hydrocarbons via hydroprocessing has the lowest jet fuel selling price and lowest green gas emissions, respectively (Diederichs et al. 2016; Wei et al. 2019). Karanja, vestita fruit, greenseed canola and jatropha oils can be used as feedstocks for hydroprocessed renewable jet fuel (Mohammad et al., 2013). These oils are non-edible oils with oleic acid as their main fatty acid component.

Numerous catalysts have been utilized for hydroprocessing of vegetable oils for production of jet fuel range hydrocarbons. Copper containing catalysts are renowned for their promising

selectivity for C=O bond hydrogenation (Manikandan et al. 2016; Ye et al. 2018). Copper based catalysts have high adsorption and activation capacity for hydrogen (Ipek et al. 2020). Bykoeva et al. (2011) performed hydroprocessing reaction over NiCu supported catalysts. The authors reported high catalyst selectivity and ascribed it to the presence of copper in the bimetallic NiCu supported catalyst. In spite of all the merits in the application of copper containing catalysts for hydroprocessing of vegetable oils and fatty acids, they have low oxophilicity (Laudenschleger et al., 2020). In order to complement the qualities of copper, metals of high oxophilicity are added to copper. The addition of high oxophilic iron as a promoter can improve the activity and selectivity of Cu based catalyst (Manikandan et al. 2016; Ayandiran et al. 2019).

Iron is known for its low price, natural abundance and rich redox chemistry. Kandel et al. (2014) carried out hydroprocessing of microalgal triglycerides over reduced Fe-based catalyst. The author reported high selectivity of liquid paraffins and attributed it to the strength of Fe-O bond in the reduced Fe based catalyst evaluated. The surface area and stability of copper catalysts can also be improved by tin (Ayandiran et al., 2020). Copper and iron loadings were optimized for oleic acid hydroprocessing for production of jet fuel range hydrocarbons in our previous work (Ayandiran et al., 2019). The role played by catalysts' active sites are complemented using support with optimized Bronsted acid sites in order to achieve a balance between production of hydrocarbons lower than C₈ and those that are higher than C₁₆. Supports of high surface area are also required for triglycerides feedstock because of its high molecular and kinetic diameters. SiO₂-Al₂O₃ support has been reported to have these required qualities (Ayandiran et al., 2019). It was reported to have moderate Bronsted acid sites and textural properties required for production of aviation turbine fuel range hydrocarbons (Ayandiran et al., 2019). The result of catalyst loading optimization in our previous work revealed 3 wt. % Fe - 13 wt.% Cu catalyst supported on silica alumina as the most promising catalyst with 74 % selectivity of jet fuel range hydrocarbons. The promotional effects of Sn on 3 wt. % Fe - 13 wt.% Cu catalyst supported on silica alumina were also studied in our subsequent work for production of aviation turbine fuel range hydrocarbons (Ayandiran et al., 2021).

A catalyst with 1 wt. % Sn, 3 wt. % Fe and 13 wt. % Cu supported on silica-alumina gives the most promising selectivity (77 %) of jet fuel range hydrocarbons. The promising results are attributed to the crystallite size of its copper phase, high surface area and weak metal support

interaction (Ayandiran et al., 2020). Higher selectivity of jet fuel range hydrocarbons was achieved due to the promotional effects of Sn.

The activity and selectivity of catalysts in catalytic reactions are function of the approach used in the variation of the reactions' operating parameters (Kim et al., 2017). The influence of independent variables (factors) on dependent variables (responses) is usually investigated using the univariate approach. The approach involves analyzing one variable at a time by keeping other independent variables constant. Production of hydroprocessed renewable jet fuel while varying temperature, time, hydrogen pressure or catalyst concentration has been carried solely using univariate approach (Kim et al. 2017; Konwar et al. 2020; Lin et al. 2020; Mirzayanti et al. 2020; Mederos et al. 2021). Analysis of more than one variable at a time using multivariate approach enables understanding of simultaneous relationship among the independent variables. Evaluation of catalyst for production of hydroprocessed renewable jet fuel using multivariate approach has not been reported in the literature.

Experimental design using response surface methodology (RSM) optimizes dependent variables by collecting statistical and mathematical techniques that can be applied for modeling and analysis of problems in which dependent variables are influenced by several independent variables. It employed first-order model for linear systems and model of higher degree of polynomial for systems with curvature. The models are employed to predict the responses and hence investigate the statistical significance of the independent variables and their interactions (Montgomery, 2001; Madadi et al. 2019; Zhang et al. 2019; Nde et al. 2020; Yahya et al. 2020). The proposed reaction pathways that give the best fit with the experimental data will be determined from kinetic modelling. From the kinetic modelling, the extent of the desired and undesired reactions will be evaluated. The hydrocracking and hydroisomerization stages are associated with the side reactions, hence kinetic modelling of hydroprocessing of vegetable oil for jet fuel production is very important (Mohit et al., 2016).

In this work, optimization study of the effects of reaction temperature, reaction time, catalyst concentration and hydrogen pressure on oleic acid conversion and selectivity of jet fuel range hydrocarbons during the evaluation of 1 wt. % Sn promoted trimetallic catalyst for oleic acid hydroprocessing was carried using an efficient face-centered central composite response surface methodology design. Kinetic study of oleic acid hydroprocessing for production of jet fuel range hydrocarbons over 1 wt. % Sn promoted trimetallic catalyst was also carried out.

6.3 Experimental design for modelling and optimization studies

In this work, response surface methodology using a face-centered central composite 3-level and 4-factor design was utilized for optimization of conversion of oleic acid and selectivity of jet fuel range hydrocarbons during oleic acid hydroprocessing. The effects of four operational parameters on conversion of oleic acid and selectivity of jet fuel range hydrocarbons were also investigated. Face-centered central composite design was used as compared to the rotatable central composite design in order to investigate the effect of the entire region of process operability (Anderson et al., 2017). In our previous work, reaction temperature (300-340 °C) and time (2-10 h) have been optimized by changing single variable at a time with promising catalyst performance. In terms of selectivity of jet fuel range hydrocarbons, these were 320 °C and 8 h of reaction time, and for oleic acid conversion, these were 340 °C and reaction time of 10 h. 2.1 MPa H₂ pressure and 5 % catalyst concentration were kept constant throughout our previous work. Hence, the selection of levels for the four factors in this work was based on our previous work (Ayandiran et al., 2020). Hydrogen pressure and catalyst concentration were operating parameters and were varied by Lin et al (2020). Temperature (300-340 °C), reaction time (6-10 h), catalyst concentration (2-8 wt. %) were the independent variables chosen in the present study. The dependent variables are oleic acid conversion and selectivity of jet fuel range hydrocarbons. Table 6.1 shows the level of the parameters considered for the central composite design scheme. 320 °C, 8 h, 2.1 MPa H₂ and 5 wt. % are the respective centre values selected for reaction temperature, reaction time, hydrogen pressure and catalyst concentration. Equation 6.1 was used to calculate the required experimental runs for the central composite design, where n_c is the number of centre points, n_r is the required number of experimental runs and k is the number of factors (independent variables).

$$n_r = 2^k + 2k + n_c \quad (6.1)$$

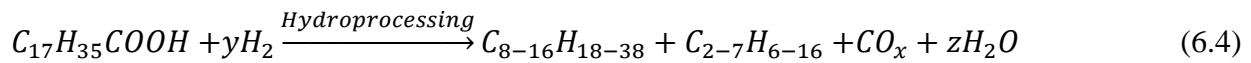
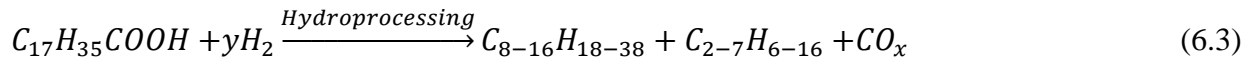
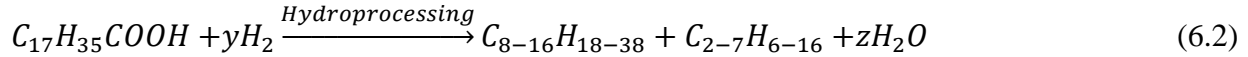
Using three independent variables ($k=3$) with ($n_c=3$), 27 experimental runs were considered. The triplicates at the centre points were utilized to calculate the experimental error. Version 12 of Design-Expert (Stat Ease Incorporation, Minneapolis, USA) was used to carry out the design of experiment. The face-centered central composite design was used to design the experiment, and data were fitted to different models to obtain a regression equation.

Table 6.1. Process Parameters and levels used for face-centered central composite design

Factors	Process Parameters	Levels		
		1	2	3
A	Temperature, T (°C)	300	320	340
B	Reaction Time, t (h)	6	8	10
C	Catalyst concentration, C (wt. %)	2	5	8
D	H ₂ Pressure, P (MPa)	1.4	2.1	2.8

6.4 Reaction kinetics and thermodynamic activation parameters

Investigation of kinetic study of oleic acid hydroprocessing over Sn(1)-Fe(3)-Cu(13)/SiO₂-Al₂O₃ catalyst was carried out. The H₂ pressure was maintained above its stoichiometric amount in order to have a complete reaction with high oleic acid conversion and also for avoidance of backward reaction. The parallel reactions involved in oleic acid hydroprocessing is shown in Equation 6.2 and 6.3, while the global reaction is shown in Equation 6.4 (Jeczminek et al., 2014)



Where, C₈₋₁₆H₁₈₋₃₈ are jet fuel range hydrocarbons; C₂₋₇H₆₋₁₆ are light hydrocarbons; and CO_x are carbon oxides

With the use of excess H₂, which favours the forward reaction towards the production of jet fuel range hydrocarbons, all the products can be neglected in the rate equation. Hence, the kinetic rate of the reaction will be a pseudo first order reaction as derived in Equation 6.6 from Equation 6.5

$$r' = \frac{-d[C_{17}H_{35}COOH]}{dt} = k'[C_{17}H_{35}COOH][H]^y \quad (6.5)$$

$$r' = \frac{-d[C_{17}H_{35}COOH]}{dt} = k[C_{17}H_{35}COOH] \quad (6.6)$$

$k = k'[H]^y$ is the reaction rate constant

$$\frac{d[C_{17}H_{35}COOH]}{[C_{17}H_{35}COOH]} = -kdt \quad (6.7)$$

$$[C_{17}H_{35}COOH] = [(C_{17}H_{35}COOH)_o](1 - 0.01X) \quad (6.8)$$

Where, $(C_{17}H_{35}COOH)_o$ is the initial oleic acid concentration and X is oleic acid conversion (%)

$$\frac{d[(C_{17}H_{35}COOH)_o](1-0.01X)}{[(C_{17}H_{35}COOH)_o](1-0.01X)} = -kdt \quad (6.9)$$

$$\int_0^X \frac{d[(C_{17}H_{35}COOH)_o](1-0.01X)}{[(C_{17}H_{35}COOH)_o](1-0.01X)} = -k \int_0^t dt \quad (6.10)$$

$$[\ln[(C_{17}H_{35}COOH)_o](1 - 0.01X)]_0^X = [-kt]_0^t \quad (6.11)$$

$$\ln[(C_{17}H_{35}COOH)_o](1 - 0.01X) - \ln[(C_{17}H_{35}COOH)_o] = -kt \quad (6.12)$$

$$\ln \frac{[(C_{17}H_{35}COOH)_o](1-0.01X)}{[(C_{17}H_{35}COOH)_o]} = -kt \quad (6.13)$$

$$\ln[1 - 0.01X] = -kt \quad (6.14)$$

The rate constant, k is evaluated by plotting $-\ln(1-0.01X)$ versus t at 300-340 °C reaction temperatures at optimum H₂ pressure and optimum catalyst concentration. The pre-exponential factor or Arrhenius constant (A) and energy of activation of the hydroprocessing reaction are obtained from the plot of $\ln k$ versus $1/T$ using the Arrhenius equation.

$$k = Ae^{-\frac{E_A}{RT}} \quad (6.15)$$

$$\ln k = \ln A - \frac{E_A}{RT} \quad (6.16)$$

Where A is the pre-exponential factor

R is the universal molar gas constant (8.314 J/mol K)

T is the absolute temperature in Kelvin

k is the kinetic rate constant

The thermodynamic activation parameters (ΔS , ΔH and ΔG) for hydroprocessing of oleic acid were calculated using Eyring-Polanyi and Gibbs free energy equations in 6.17 and 6.18.

$$\ln \left(\frac{k}{T} \right) = -\frac{\Delta H}{R} \frac{1}{T} + \ln \frac{K_B}{h} + \frac{\Delta S}{R} \quad (6.17) \text{ (Nur et al., 2020)}$$

Where k= rate constant

T= absolute temperature

ΔH = activation enthalpy of reaction

ΔS = activation entropy of reaction

K_B = Boltzman constant= 1.38×10^{-23} J/K

h= Planck constant= 6.62×10^{-34} Js

$$\Delta G = \text{Gibbs free energy of reaction} = \Delta H - T\Delta S \quad (6.18)$$

6.5 Result and discussion

6.5.1 Modelling and optimization of hydroprocessing of oleic acid

The oleic acid conversion (X) and selectivity of jet fuel range hydrocarbon (S) as a function reaction temperature (T), H₂ pressure (P), catalyst concentration (C), and reaction time (t) are shown in Table 6.2. The reaction temperature, H₂ pressure, catalyst concentration and reaction time were varied within 300-340 °C, 1.4- 2.8 MPa, 2-8 wt. % and 6-10 h. Considering all the four process parameters and their corresponding levels, the highest oleic acid conversion obtained was 98.1 % at 340 °C, 1.4 MPa, 8 wt. % catalyst concentration and 10 h reaction time. Similarly, the highest selectivity of jet fuel range hydrocarbons obtained was 79.7 % at 320 °C, 2.1 MPa, 5 wt. % catalyst concentration and 8 h reaction time. The conversion of oleic acid generally increased with temperature from 300 °C to 340 °C at the same H₂ pressure, catalyst concentration and reaction time because absolute temperature has a direct relationship with average kinetic energy. Hence, the average kinetic energy of the reaction increased due to temperature increase. The rate of collision of oleic acid and hydrogen on the surface of the Sn(1)-Fe(3)-Cu(13)/SiO₂-Al₂O₃ catalyst increased due to increase in its average kinetic energy and hence leads to increase in the conversion of oleic acid. This trend in the conversion of oleic acid is in tandem with what was observed by different researchers during hydroprocessing reactions (Li et al., 2012). A different trend was observed for selectivity of jet fuel range hydrocarbons with increase in temperature due to production of hydrocarbons lower than jet fuel range hydrocarbons (C₈-C₁₆). Higher selectivity values were achieved at 320 °C reaction temperature due to mild Bronsted/Lewis acidity ratio of the evaluated Sn(1)-Fe(3)-Cu(13)/SiO₂-Al₂O₃ catalyst.

As stated earlier, face-centered central composite design was utilized to design experiments with 27 reaction runs in order to develop regression models that will predict oleic acid conversion and selectivity of jet fuel range hydrocarbons from selected range of temperature, H₂ pressure, catalyst concentration and reaction time with satisfactory correlation coefficient, adequate precision, acceptable standard error and variance inflation factor. In order to comprehend the correlation between the two responses (oleic acid conversion and selectivity of jet fuel range hydrocarbons) and the four earlier stated process parameters, a regression model was developed by fitting experimental data in Table 6.2 to linear, two-factor interaction, quadratic and cubic models. The adequacy of the models was verified by comparing their correlation coefficient, sequential p-value and lack of fit p-value for each of the two responses. The outcome of the model

adequate verification for the face-centered central composite design for oleic acid conversion and selectivity of jet fuel range hydrocarbons is presented in Tables 6.3 and 6.4, respectively. A model with a low probability value (p-value <0.05) and lack of fit p-value that is greater than 0.05 is known to be significant (Anderson et al. 1974; Anderson et al. 2008).

Table 6.2: Face-centered central composite design matrix with four operational parameters, corresponding levels and responses for hydroprocessing of oleic acid

Run	Temperature, T(°C)	H ₂ Pressure, P(MPa)	Catalyst concentration, C (%)	Reaction time, t (h)	Oleic acid Conversion, X (%)	Selectivity of jet fuel range hydrocarbons, S (%)
1	300	2.8	2	6	74.5	48.6
2	340	1.4	8	6	93.4	70.8
3	300	2.1	5	8	89.5	70.4
4	320	2.1	5	8	93.4	79.7
5	320	2.8	5	8	96.1	70.1
6	340	2.8	2	10	86.7	43.6
7	300	2.8	8	10	90.5	41.2
8	340	2.8	2	6	80.4	39.5
9	340	2.1	5	8	96.5	78.2
10	300	2.8	8	6	87.3	50.4
11	340	2.8	8	10	94.3	40.8
12	340	2.8	8	6	97.8	63.6
13	340	1.4	2	10	88.3	45.6
14	340	1.4	8	10	98.1	59.2
15	320	1.4	5	8	85.4	77.4
16	300	1.4	8	10	79.1	42.4
17	300	1.4	2	10	75.6	37.5
18	320	2.1	5	6	89.5	77.3
19	320	2.1	5	8	92.1	76.8
20	320	2.1	5	10	96.8	67.8
21	300	2.8	2	10	80.4	36
22	320	2.1	2	8	72.5	45.3
23	300	1.4	8	6	72.4	63.7
24	340	1.4	2	6	80.3	65.1
25	300	1.4	2	6	66.2	45.4
26	320	2.1	5	8	94.8	75.6
27	320	2.1	8	8	96.7	54.1

Table 6.3: Model adequacy verification for the face-centered central composite design: Oleic acid conversion

Source	R ²	Adjusted R ²	Predicted R ²	Sequential p-value	Lack of fit p-value
Linear	0.65	0.59	0.49	<0.0001	0.0469
2FI	0.73	0.57	0.21	0.5824	0.0429
Quadratic	0.94	0.86	0.68	0.0010	0.1248
Reduced Cubic	0.99	0.97	0.86	<0.0001	0.4263

Table 6.4: Model adequacy verification for the face-centered central composite design: Selectivity of jet fuel range hydrocarbons

Source	R ²	Adjusted R ²	Predicted R ²	Sequential p-value	Lack of fit p-value
Linear	0.27	0.14	-0.02	0.1199	0.0206
2FI	0.31	-0.13	-1.25	0.9906	0.0152
Reduced Quadratic	0.96	0.93	0.77	<0.0001	0.2070
Cubic	0.95	0.78	-6.80	0.0442	0.0442

R² (Correlation coefficient) is a statistical measure that shows the effectiveness of models in explaining experimental data (Tsegaye et al. 2019; Hamadache et al. 2020). The outcome of the adjustment of R² value to prevent too many terms is known as adjusted R² value (Adepoju et al. 2020; Daniyan et al. 2020). The reduced cubic acid conversion and reduced quadratic selectivity models given in Tables 6.3 and 6.4 have the highest R² values showing that they are the most effective models for the prediction of the experimental data presented in Table 6.2. A difference of less than 0.2 in the adjusted and predicted R², shows that there is no challenge of model overfitting (Bartlett et al. 2020; Rathi et al. 2020; Tesfay et al. 2020). The difference between the predicted and adjusted R² value of the reduced cubic oleic acid conversion and reduced quadratic selectivity models is less than 0.2 indicating a reasonable agreement.

F-value of a regression model is obtained by calculating the ratio of the mean squares of regression model and error. Similarly, F-value of each controlled variable and their interactions are also determined by evaluating the ratio of their mean square and that of the residuals (Shokri et al., 2020). F-value indicates the effects of process parameters on the regression model (Simsek

et al., 2020) Statistical significance of the models is demonstrated by the probability value (p-value) using the F-value. Lack of fit p-value shows that there is high non-significant lack of fit leading to a strong indication that the model fits adequately with the data obtained from experiment (Hosseinzadeh et al. 2019; Gayary et al. 2020). The highest lack of fit p-value presented in Tables 6.4 and 6.5 are 0.43 and 0.21, respectively, for the reduced cubic oleic acid conversion model and reduced quadratic selectivity of jet fuel range hydrocarbon model. The two highest lack of fit p-values are both greater than 0.05, hence they reflect good model adequacy.

The sequential p-values of the models in Tables 6.5 and 6.6 is the probability that their F-values occur due to noise. The p-values of the reduced cubic oleic acid conversion and reduced quadratic selectivity models are both 0.0001 indicating that they are significant. Hence, from the results shown in Tables 6.5 and 6.6, the reduced cubic model and the reduced quadratic model were selected for the best prediction of the experimental data presented in Table 6.2. The reduced cubic oleic acid conversion model and the reduced quadratic selectivity of jet fuel range hydrocarbons model are shown in equations 6.19 and 6.20, respectively.

$$\begin{aligned}
 X = & 92.68 + 3.50 T + 5.35 P + 12.10 C + 2.67 t - 2.52 TP + 0.9562 TC + 0.9562 PC \\
 & - 1.06 Pt - 1.16 Ct - 8.54 C^2 - 2.94 T^2P - 7.07 T^2C \\
 & + 2.33 TP^2
 \end{aligned} \tag{6.19}$$

$$\begin{aligned}
 S = & 75.13 + 3.93 T - 4.07 P + 4.42 C - 6.13 t - 2.53 TP + 0.65 TC - 0.8875 PC + 1.24 Pt \\
 & - 1.81 Ct - 24.27 C^2 \\
 & - 1.42 t^2
 \end{aligned} \tag{6.20}$$

Where X, S, T, P, C and t represent oleic acid conversion (%), selectivity of jet fuel range hydrocarbons (%), reaction temperature(°C), H₂ pressure (MPa), catalyst concentration (wt.%) and reaction time (t), respectively. The combined square terms in the equations are interaction and square terms of the models.

Analysis of variance (ANOVA) was carried out for the two responses to determine the significance of all the four controlled variables and their interactions using 95% confidence interval (p-value < 0.05). The ANOVA results for oleic acid conversion and selectivity of jet fuel range hydrocarbons are presented in Tables 6.5 and 6.6, respectively. P-value of 0.0001 means that the probability that the large 50.45 F- value occurs due to noise is as low as 0.01%. Since p-value is less than 0.05, the reduced cubic oleic acid model is significant. In the same vein, the p-values of the reaction temperature, H₂ pressure, catalyst concentration and reaction time are below

0.05. This indicates that all the four controlled variables have significant effects on oleic acid conversion. All the interactions shown in Table 6.6 have p-values below 0.05 with the exception of T^2 , P^2 and TP^2 . These three square and interaction terms have no significant effect on oleic acid conversion.

Table 6.5: Analysis of Variance (ANOVA) and Regression Analysis of the Reduced Cubic Models for Oleic Acid Conversion

Source	Sum of squares	Degree of freedom	Mean square	F-value	p-value	Remark
Model	2159.56	15	143.97	50.45	<0.0001	Significant
Temperature, T (°C)	24.50	1	24.50	8.58	0.0137	
H ₂ pressure, P (MPa)	57.24	1	57.24	20.06	0.0009	
Catalyst concentration, C (%)	292.82	1	292.82	102.61	<0.0001	
Reaction time, t (h)	128.00	1	128.00	44.85	<0.0001	
TP	101.51	1	101.51	35.57	<0.0001	
TC	14.63	1	14.63	5.13	0.0448	
PC	14.63	1	14.63	5.13	0.0448	
Pt	17.85	1	17.85	6.25	0.0295	
Ct	21.39	1	21.39	7.50	0.0193	
T ²	0.9528	1	0.9528	0.3339	0.5750	
P ²	7.78	1	7.78	2.73	0.1270	
C ²	171.08	1	171.08	59.95	<0.0001	
T ² P	15.41	1	15.41	5.40	0.0403	
T ² C	88.83	1	88.83	31.13	0.0002	
TP ²	9.66	1	9.66	3.39	0.0929	
Residual	31.39	11	2.85			
Lack of fit	27.75	9	3.08	1.69	0.4263	Not significant
Pure error	3.65	2	1.82			
Adequate precision	24.83					
R ²	0.99					
Adjusted R ²	0.97					
Predicted R ²	0.86					

The overall F-value and p-value of the reduced quadratic selectivity of jet fuel range hydrocarbons model are 30.24 and 0.0001, respectively as shown in Table 6.6. This indicates that the developed model is significant. The p-values of all the controlled variables are below 0.05 indicating that they all have significant effect on the selectivity of jet fuel range hydrocarbons. Of

all the interactions presented in Table 6.6, only the TP and C² interactions have significant effect on the selectivity of jet fuel range hydrocarbons.

Table 6.6: Analysis of Variance (ANOVA) and Regression Analysis of the Reduced Quadratic Models for Selectivity of Jet Fuel Range Hydrocarbons

Source	Sum of squares	Degree of freedom	Mean square	F-value	p-value	Remark
Model	5623.60	11	511.24	30.24	<0.0001	Significant
Temperature, T (°C)	278.48	1	278.48	16.47	0.0010	
H ₂ pressure, P (MPa)	298.49	1	298.49	17.66	0.0008	
Catalyst concentration, C (%)	352.01	1	352.01	20.82	0.0004	
Reaction time, t (h)	675.89	1	675.89	39.98	<0.0001	
TP	102.01	1	102.01	6.03	0.0267	
TC	6.76	1	6.76	0.3999	0.5367	
PC	12.60	1	12.60	0.7455	0.4015	
Pt	24.50	1	24.50	1.45	0.2473	
Ct	52.50	1	52.50	3.11	0.0982	
T ²	1962.90	1	1962.90	116.12	<0.0001	
P ²	6.69	1	6.69	0.3957	0.5388	
Residual	253.56	15	16.90			
Lack of fit	244.68	13	18.82	4.24	0.2070	Not significant
Pure error	8.89	2	4.44			
Adequate precision	15.69					
R ²	0.96					
Adjusted R ²	0.93					
Predicted R ²	0.77					

Adequate precision of a model is the ratio of its signal and noise. A ratio greater than 4 is desirable, indicating that the regression model is sufficient to navigate the design space (Fonseca et al. 2020; Ouma et al. 2020; Singh et al. 2020). Adequate precisions of 24.83 and 15.69 were obtained for the reduced cubic oleic acid conversion model and reduced quadratic selectivity model as shown in Tables 6.5 and 6.6, respectively. This indicates that the two models can be used to navigate the design.

Parity plots showing the correlation between the oleic acid conversion and selectivity of jet fuel range hydrocarbons obtained from experiment and their corresponding predicted values are presented in a parity plot depicted in Figures 6.1 and 6.2. The experimental data points in both

parity plots clustered around the line of unit slope. This strongly indicates that there is good agreement between the predicted and experimental response values.

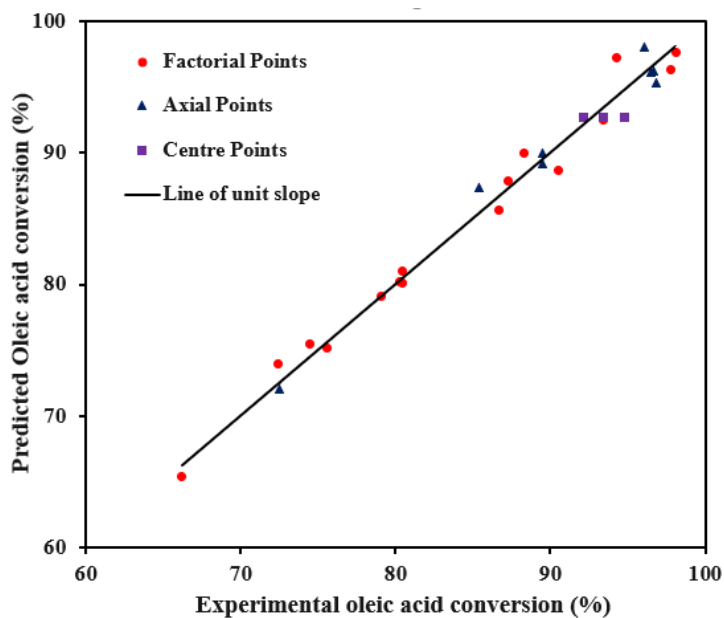


Figure 6.1: Parity plot of the predicted versus experimental oleic acid conversion

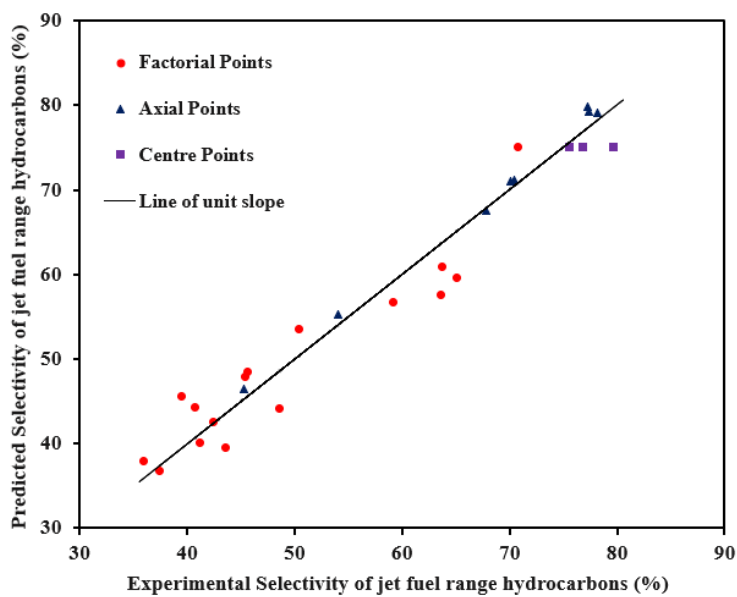


Figure 6.2: Parity plot of the predicted versus experimental selectivity of jet fuel range hydrocarbons

The effects of the operating variables and their interactions on oleic acid conversion and selectivity of jet fuel range hydrocarbons were investigated by plotting three dimensions surface curves while keeping other controlled variables constant at their centre point values as shown in Figures 6.3-6.6. The 3D response surface plots are graphical depiction of the oleic acid conversion and selectivity of jet fuel range hydrocarbons obtained respectively from equations 6.18 and 6.19 in terms of different operating parameters (reaction temperature, H₂ pressure catalyst concentration and reaction time). The two most significant interaction effects (TP and Ct) on oleic acid conversion and selectivity of jet fuel range hydrocarbons based on the ANOVA result were considered for 3D surface plot analysis.

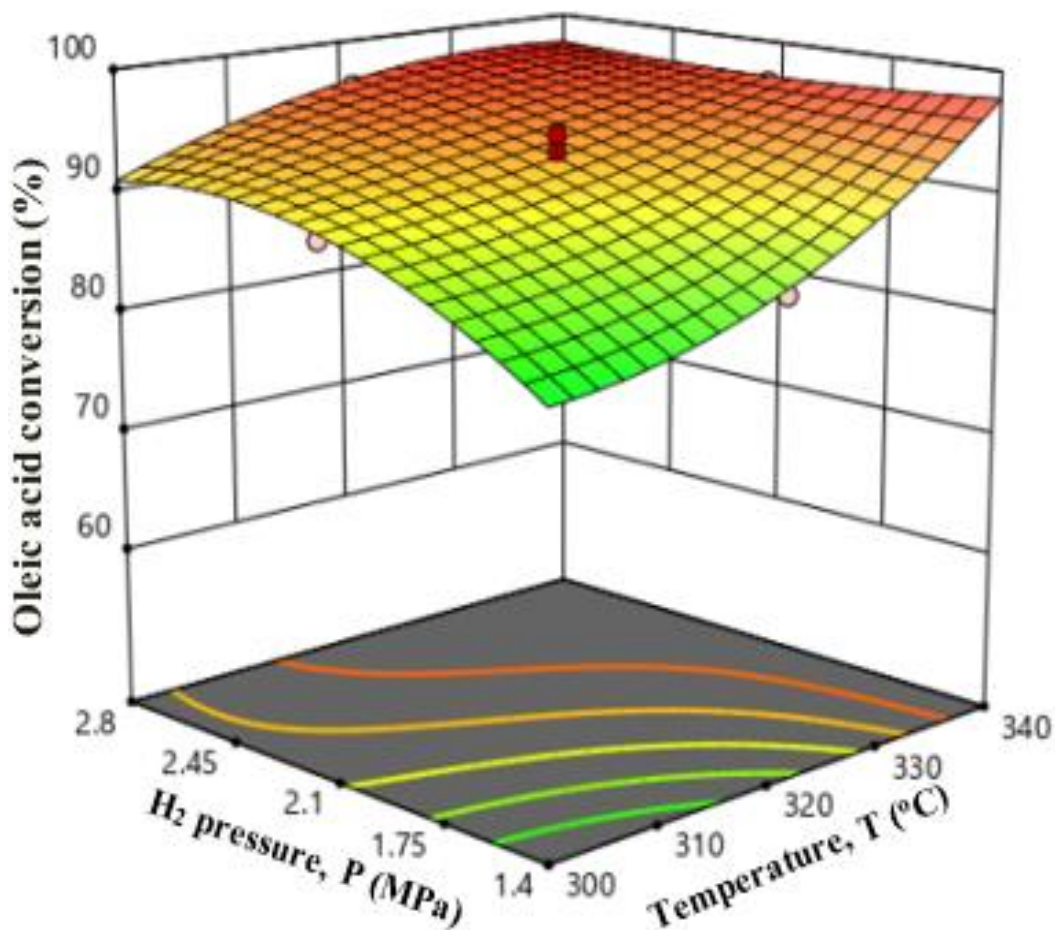


Figure 6.3: 3D response surface plot of the main and interaction effects of H₂ pressure and temperature on oleic acid conversion

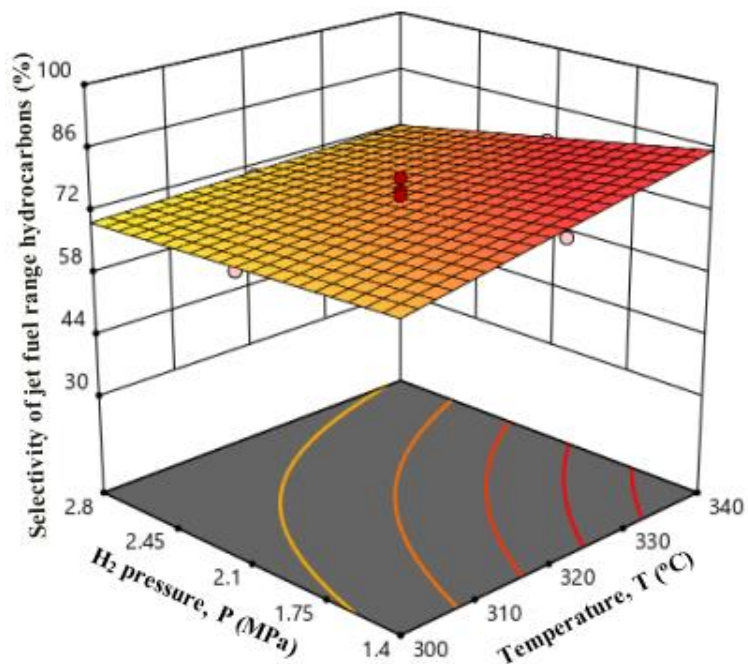


Figure 6.4: 3D response surface plot of the main and interaction effects of H₂ pressure and temperature on selectivity of jet fuel range hydrocarbons

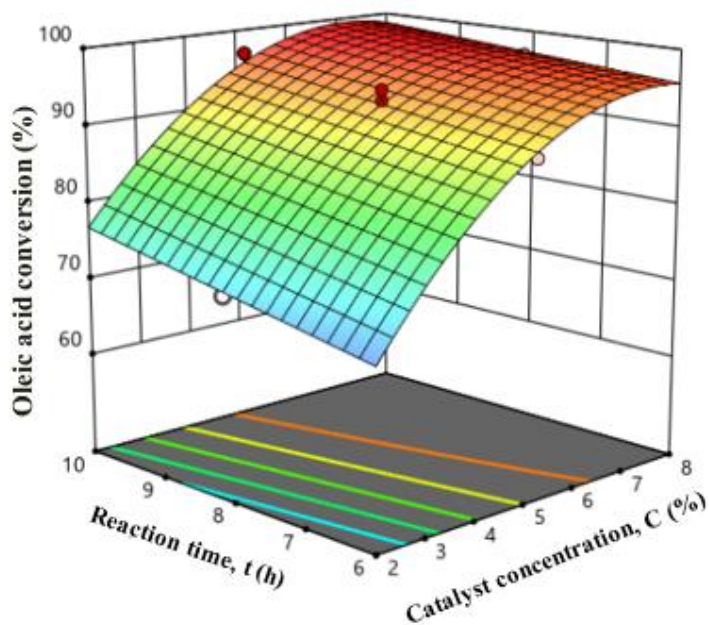


Figure 6.5: 3D response surface plot of the main and interaction effects of reaction time and catalyst concentration on oleic acid conversion

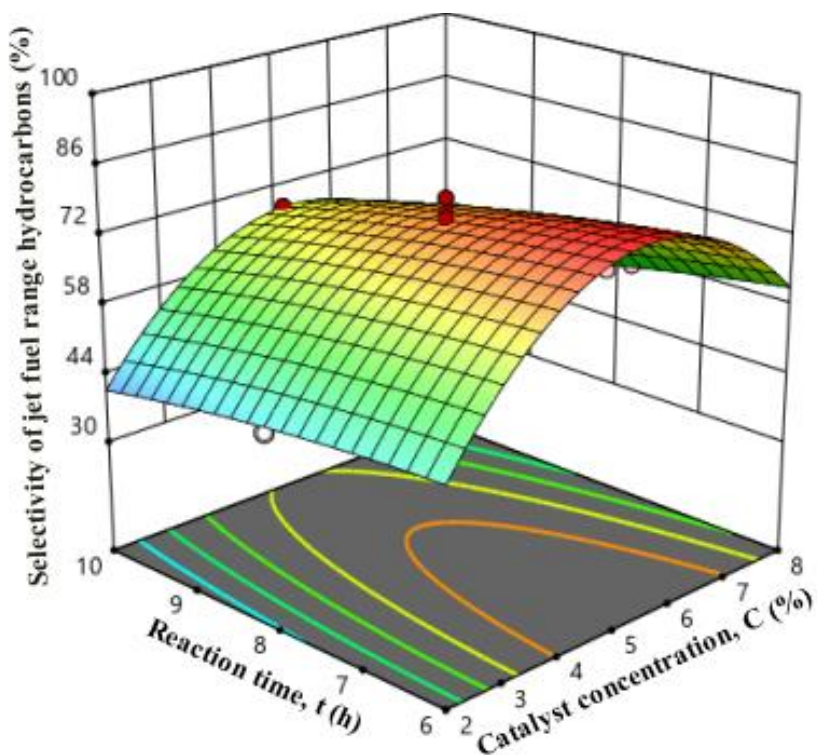


Figure 6.6 3D response surface plot of the main and interaction effects of reaction time and catalyst concentration on selectivity of jet fuel range hydrocarbons

Figure 6.3 shows the dependence of the main effects (reaction temperature and H_2 pressure) and their interaction effects on oleic acid conversion while maintaining catalyst concentration and reaction time at their centre point values. Oleic acid conversion increased as the temperature was increased from 300-340 °C in each of the considered H_2 pressure. This phenomenon is typical for hydroprocessing reactions. It indicates that the forward reaction is favoured by increasing the temperature of the reaction because a decrease in the conversion of oleic acid as a result of increase in temperature will indicate that backward reaction is favoured.

Increase in H_2 pressure from 1.4 MPa to 2.8 MPa at any constant temperature considered in this experiment leads to increase in oleic acid conversion. This can be attributed to the fact that by increasing the H_2 pressure, the collision of H_2 gas and oleic acid increases on the surface of the catalyst and automatically leads to increase in oleic acid conversion. Different researchers have shown this trend in the relationship between H_2 pressure and fatty acids/vegetable oils conversion

in hydroprocessing reactions (Snare et al. 2006; Kubickova et al. 2007; Kubicka et al. 2010; Kwon et al., 2010; Maki et al. 2011; Sotelo et al. 2011; Lee et al. 2013).

The effect of the interaction of reaction temperature and H₂ pressure on the oleic acid conversion is obvious on the 3D response surface plot in Figure 6.3. The rate of increment of oleic acid conversion, while H₂ pressure was raised from 1.4 to 2.8 MPa decreases as the temperature was increased from 300 °C to 340 °C indicating strong interaction between the two factors. During the hydroprocessing reaction in the Parr batch reactor, the initial H₂ pressure was set for each reaction run before raising the temperature of the reactor from ambient temperature to the desired temperature for reaction. The H₂ pressure increases with increase in the reaction temperature. This explains the strong interaction between the H₂ pressure and reaction temperature. It is clear that the two factors are not independent of each other.

The selectivity of jet fuel range hydrocarbons as a function of temperature of the reaction (300 °C- 340 °C), H₂ pressure (1.4 MPa -2.8 MPa) and their interactions at constant and reaction time are shown in Figure 6.4. The rate of increment of selectivity of jet fuel range hydrocarbons as H₂ pressure was raised from 1.4 to 2.8 MPa increased as temperature was raised from 300 to 340 °C due to a strong interaction between the temperature of the reaction and H₂ pressure used for the reaction.

The dependence of the oleic acid conversion on reaction time (6-10 h) and catalyst concentration (2-8 wt.%) and their interaction is presented in Figure 6.5. From the figure, oleic acid conversion increased with reaction time and catalyst concentration. On the effect of catalyst concentration in wt. %, this will allow for increase in the number of active sites and hence increase in oleic acid conversion. Increase in catalyst concentration causes increase in triglyceride/fatty acid conversion as explained by numerous researchers that worked on hydroprocessing reactions (Veriansyah et al. 2012; Ojagh et al. 2018; Le et al. 2020). Increase in reaction time leads to increase in oleic acid conversion since the forward reaction is the most favoured path. The rate of increment of oleic acid due to increase in reaction time from 6-8 h dwindled gradually as catalyst concentration was raised from 2 to 8 wt.% indicating strong interaction effect of these two factors on oleic acid conversion. Oleic acid conversion stabilized faster at high catalyst concentration due to high number of active sites involved in the reaction.

The selectivity of jet fuel range hydrocarbons as a function of catalyst concentration (2-8 wt. %) and reaction time (6-8 h) and their interaction is depicted in Figure 6.6. The selectivity

increases and later decreases as the catalyst concentration was raised from 2 wt. % to 8 wt. %. The increase in selectivity of jet fuel range hydrocarbons is attributed to increase in the number of catalyst active sites that are selective towards the production of jet fuel range hydrocarbons. The decrease in the selectivity of jet fuel range hydrocarbons can be ascribed to the production of lighter hydrocarbons due to its increase in the active sites of the catalyst. The change of the selectivity of jet fuel range hydrocarbons from 2-8 wt.% catalyst concentration decreased from 6-10 h reaction indicating strong interaction between the reaction time and catalyst concentration.

Face-centered central composite design was utilized to obtain the best combination of the four operating parameters (reaction temperature, H₂ pressure, catalyst concentration and reaction time) for the maximization of oleic acid conversion and selectivity of jet fuel range hydrocarbon. The optimization was carried out using the numerical optimization function of the Design Expert Software. Temperature, H₂ pressure, catalyst concentration and reaction time were set within the respective range of 300-340 °C, 1.4 -2.8 MPa, 2-8 wt % and 6-10 h.

Maximum oleic acid conversion and selectivity of jet fuel range hydrocarbons of 98.2 % and 82.2 % respectively were obtained from the optimum 339.5 °C reaction temperature, 1.6 MPa H₂ pressure, 6.2 wt. % catalyst concentration and 8.0 h reaction time as shown in Figure 6.7. Using the optimum reactions, the accuracy of the predicted reduced cubic oleic acid conversion model and reduced quadratic selectivity of jet fuel range hydrocarbons model was verified by running the experiment in triplicate. 98.4 % and 82.1 % were obtained from the mean of the responses. The experimental and predicted responses were used to evaluate percentage error using equation 6.19. The percentage error of oleic acid conversion and selectivity of jet fuel range hydrocarbons was found to be 0.2 and 0.1 %, respectively.

$$\text{Percentage error} = \frac{\text{Experimental value of response} - \text{Predicted value of response}}{\text{Experimental value of response}} \times 100 \quad (6.21)$$

6.5.2 Kinetic and thermodynamic study of the hydroprocessing reaction

The kinetics of the hydroprocessing reaction was carried out at optimum catalyst concentration (6.2 wt. %) and the pressure (1.6 MPa). The reaction temperature and reaction time were varied within the range of 300-340 °C and 2-10 h, respectively. Figure 6.8 depicts the exponential increase in the oleic acid conversion as a function of the reaction time (2-10 hrs) at various reaction temperatures (300-340 °C) indicating pseudo first order kinetics. Using the model, $\ln(1/(1-0.01X))$ was plotted against time based on equation 6.13 at various temperatures as shown in Figure 6.9. The data points were fitted using a zero intercept trendline. The rate constant was

determined from the slope of the curves at each reaction temperature. An Arrhenius plot of $\ln k$ versus $1/T$ as shown in Figure 6.10 using the obtained k values to evaluate the activation energy and pre-exponential factor from the slope and intercept of the graph, respectively using Equation 6.16.

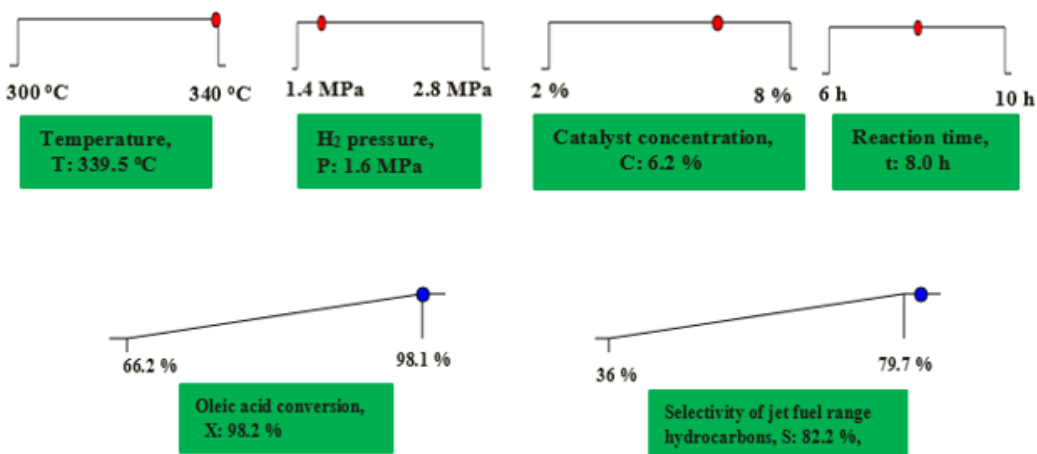


Figure 6.7. Experimental limit and optimum values of process parameters and responses

The activation energy (E_A) and pre-exponential factor (A) obtained are presented in Table 6.8. The activation energy obtained in this work is reviewed with previous works on oleic acid hydroprocessing and presented in Table 6.9. Konwar et al (2020) worked on hydroprocessing of tall oil fatty acids over Ru/C catalyst at reaction temperature of 296-326 °C, reaction time of 1-4 h, hydrogen pressure of 3.5 MPa and catalyst concentration of 2.5-7.5 wt. % and obtained an activation energy of 148.9kJ/mol. The same authors obtained a lower activation energy of 134.4kJ/mol over Pd/C catalyst at the similar operating conditions. Mederos et al (2021) utilized NiMo/Al₂O₃ catalyst for hydroprocessing of castor oil methyl ester at 395-425 °C, reaction time of 2-8 h, 2 MPa H_2 pressure and 5.6 wt. % catalyst concentration and obtained an activation energy of 123.4kJ/mol. Mirzayanti et al (2020) obtained 84.3kJ/mol activation energy for hydroprocessing of ceiba pentandra oil over NiMo/HZSM-5 at 300-400 °C, 0.5-7 h, 3 MPa H_2 pressure and 0.55 wt. % catalyst concentration. In our present study, a simultaneous variation of all the four operating parameters (300-340 °C, 6-10 h, 1.4-2.8 MPa H_2 pressure and 2-8 wt. % catalyst concentration) was carried out for hydroprocessing of oleic acid over 1 wt. % Sn promoted Fe(3)-Cu(13)/SiO₂-

Al₂O₃ catalyst. The 1 wt. % Sn promoted Fe(3)-Cu(13)/SiO₂-Al₂O₃ catalyst was able to lower the minimum energy required for hydroprocessing of oleic acid to 50.7kJ/mol as shown in Table 6.9. The activation energy obtained in this present work was the least as compared to all the reviews.

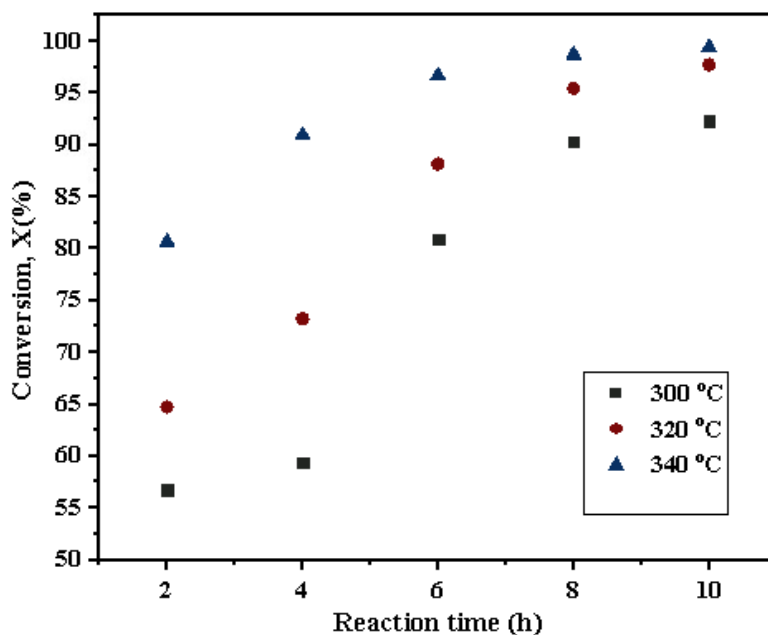


Figure 6.8. Effect of reaction temperature (300-340 °C) on oleic acid conversion, 1.6 MPa H₂ pressure and 6.2 wt. % catalyst concentration

Thermodynamic activation parameters were evaluated using equation 6.16 and Figure 6.11 and presented in Table 6.8. 45.8kJ/mol was obtained as activation enthalpy of the reaction. The positive enthalpy shows that the oleic acid hydroprocessing is endothermic that requires energy input during the process. The reactions during the oleic acid hydroprocessing reactions includes hydrodehydrogenation, hydrodecarboxylation, hydrodecarbonylation and hydrocracking. Although the hydrodehydrogenation and hydrocracking reactions are both dominant. The heat absorbed during hydrocracking transcends the heat emitted during hydrodehydrogenation, hence, the heat absorbed during the overall reactions is endothermic. -0.25kJ/mol was calculated as activation entropy of the reaction indicating irreversibility of the process. Gibb's free energy was calculated from the activation enthalpy and entropy at 300-340 °C using equation 6.18. The positive values of Gibb's free energy show that the reaction is non-spontaneous with higher energy level of transition state

than the reactant. Reaction can still proceed at operating temperatures in a non-spontaneous manner (Malhotra and Ali, 2018).

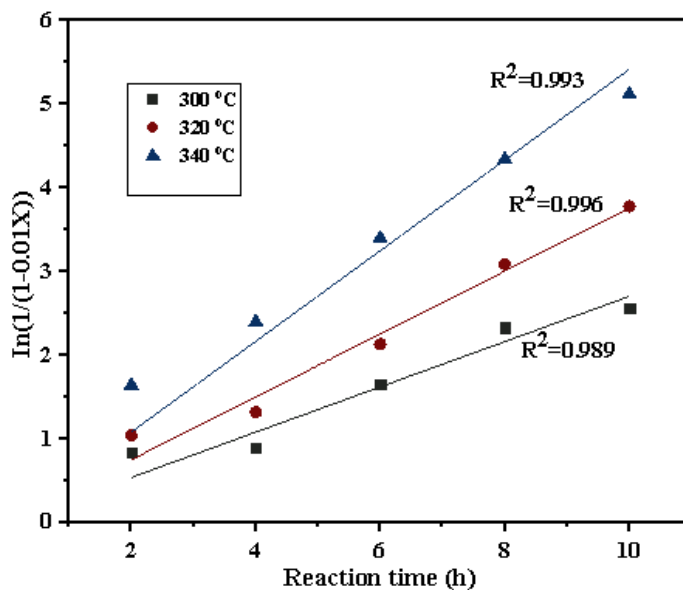


Figure 6.9. $\ln(1/(1-0.01X))$ versus reaction time at reaction temperature of 300-340 °C, 1.6 MPa H_2 pressure and catalyst concentration of 6.2 wt.%

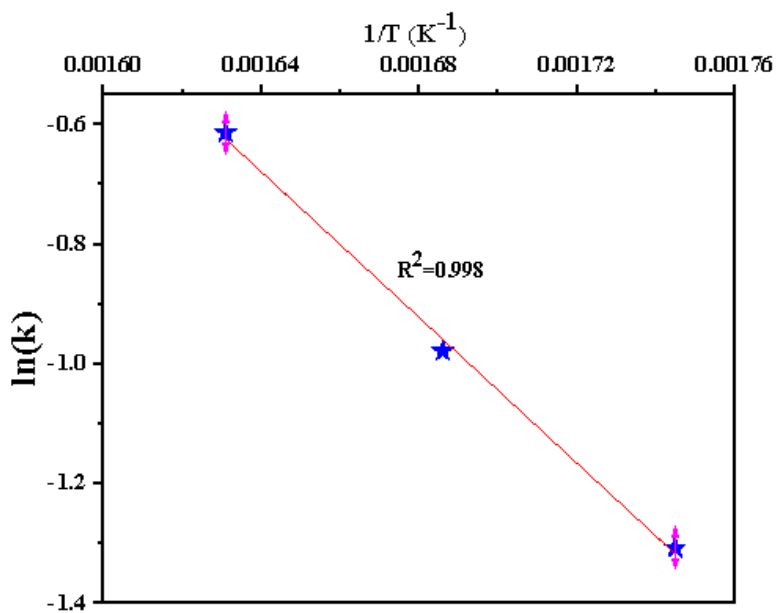


Figure 6.10. $\ln(k)$ versus $1/T$ at reaction temperature of 300-340 °C, 1.6 MPa H_2 pressure

Table 6.7: Kinetic and thermodynamic parameters for oleic acid hydroprocessing

T (°C)	k (h ⁻¹)	R ²	E _A (kJ/mol)	A (h ⁻¹)	ΔH (kJ/mol)	ΔS (kJ/molK)	ΔG (kJ/mol)
300	0.14	0.989	50.7	1.12×10 ⁴	45.78	-0.25	188.78
320	0.23	0.996					193.77
340	0.32	0.993					198.76

Table 6.8: A review on activation energy of hydroprocessing of fatty acids/triglycerides

Feedstock	Catalyst	Operating Conditions				Activation Energy (kJ/mol)	References
		Temperature (°C)	Time (h)	H ₂ pressure (MPa)	Catalyst Concentration (wt. %)		
Tall oils fatty acids (Oleic acid and Linoleic acid)	Ru/C sigma Pd/C sigma	296-326	1-4	3.5	2.5-7.5	134.4 148.9	Konwar et al., 2020
Castor oil methyl esters	NiMo/ Al ₂ O ₃	395-425	2-8	2	5.6	123.4	Mederos et al., 2020
Ceiba pentandra oil	NiMo/ HZSM-5	300-400	0.5-7	3	0.55	84.3	Mirzayanti et al., 2020
Oleic acid	Sn(1)- Fe(3)- Cu(13)/ SiO ₂ - Al ₂ O ₃	300-340	6-10	1.4-2.8	2-8	50.7	Present study

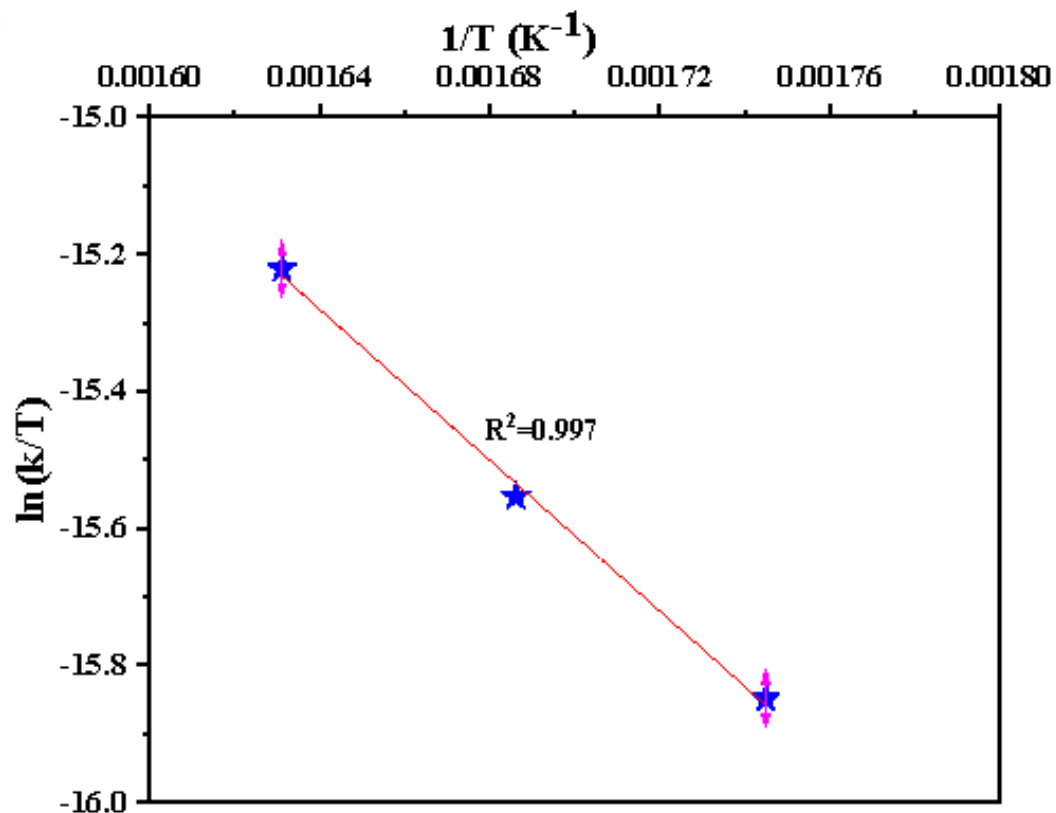


Figure 6.11. $\ln(k/T)$ versus $1/T$ at reaction temperature of 300-340 °C , 1.6 MPa H_2 pressure and catalyst concentration of 6.2 wt.%

6.6 Conclusions

For the first time, a response surface method based on a face-centered central composite design was utilized for oleic acid hydroprocessing. The process parameters used were within the range of 300-340°C reaction temperature, 1.4-2.8 MPa, H_2 pressure, 2-8 wt.% catalyst concentration and 6-8 h reaction time. Reduced cubic oleic acid conversion and reduced quadratic selectivity of jet fuel range hydrocarbons model of high adequate precision, high correlation coefficient and high significance levels based on low p-value was developed. Maximum oleic acid and maximum selectivity of jet fuel range hydrocarbons of 98.2% and 82.2%, respectively at optimum conditions of 339.5 °C temperature, 1.6 MPa H_2 pressure, 6.2 wt.% catalyst concentration and 8 h reaction time was obtained via numerical optimization. Kinetic and thermodynamic parameters' evaluations show that the reaction is endothermic and irreversible with activation enthalpy of 45.8kJ/mol and activation entropy of ΔS of -0.25kJ/mol.

CHAPTER 7

Technoeconomic analysis of jet fuel produced from greenseed canola oil over tin promoted catalyst

The content of this chapter will be submitted for publication as book chapter.

Contribution of the Ph.D. Candidate

Process simulation and technoeconomic analysis were carried out by Afees A. Ayandiran in due consultation with Dr. Ajay K. Dalai and Dr. Yongfeng Hu. The manuscript was drafted and reviewed by Afees A. Ayandiran based on the guidance and suggestions provided by Dr. Ajay K. Dalai and Dr. Yongfeng Hu.

Contribution of this chapter to the overall PhD work

This chapter investigates process simulation and Technoeconomic analysis of jet fuel produced from greenseed canola oil over tin promoted catalyst

7.1 Abstract

Production of sustainable aviation fuel that will be competitive with petroleum derived jet fuel in terms of its cost effectiveness has been the subject of different papers in recent years. In this study, process simulation and technoeconomic analysis of greenseed canola derived jet fuel range hydrocarbons were carried out using a SuperPro design software. 10,000 kg/h (79200 MT/year) of oleic acid (model compound of greenseed canola oil) was hydroprocessed with 1.6 MPa of hydrogen gas over a 1 wt. % Sn promoted trimetallic catalyst to produce 7493 kg/h (59345 MT/year) jet fuel range hydrocarbons of 99.5 wt. % purity. Economic evaluation of the production process revealed annual operating cost, yearly generated revenue and net annual profit of 35.89 million dollars, 37.95 million dollars and 1.25 million dollars, respectively. Apart from the profitability of the production project, its promising economic feasibility was also revealed in its 38.46 % return on investment and 2.6 years payback time.

7.2 Introduction

Air transport plays an essential role in the daily life of the contemporary world (Wang et al., 2016). The annual global consumption of jet fuel was reported to be 2.3 billion barrels in 2019 (ATAG, 2020). About 9.5% of conventional crude oil are utilized for jet fuel production (Wang

et al., 2016). The challenges of environmental impact, global security and the declining petroleum resources have made it imperative to produce sustainable fuels using clean technologies of high energy efficiency (Chen et al. 2020; Duan et al. 2020; Lin et al. 2020) Bio-jet fuels provide solutions to these problems due to their high renewability, sustainability, and energy efficiency (Wang et al., 2016).

Jet fuel are produced from different conversion technologies including upgrading of isoprenoids derived from fermentation of sugar, upgrading of Fischer Tropsch liquids derived from catalytic conversion of syngas, upgrading of alcohol and hydroprocessing of vegetable oil. Of all the process technologies, the only conversion route with far-reaching deployment are the hydroprocessing technique of producing jet fuel (Wang et al. 2016; Martinez et al. 2019). The hydroprocessed renewable jet fuels have high energy density, and emission of greenhouse gases from its combustion is low. The jet fuel is aromatic and sulphur free. Unlike biodiesel, they are non-biodegradable, hence they have resistance to the growth of microbes (Wang et al., 2016). They find application in conventional aviation turbine engines without modification and without blending with conventional petroleum-derived jet fuels. Hydroprocessed jet fuels are suitable for high altitude flights due to their high cold flow properties (Wang et al., 2016). The greatest importance of the bio jet fuel conversion route via hydroprocessing lies in its lowest minimum jet fuel selling price in comparison with other technologies (Martinez et al., 2019).

Diederichs et al (2020) carried out techno-economic analysis of jet fuel produced via vegetable oil hydroprocessing, Upgrading of the product of Fischer Tropsch synthesis and also upgrading of sugar cane juice derived ethanol by developing process flow diagram, material balance and equipment design for the three biojet fuel conversion routes using ASPEN Plus simulations to obtain minimum jet fuel selling prices of 1.42 \$/kg, 1.56 \$/L and 1.63 \$/kg; respectively. The authors obtain a total capital investment of 179.4 million dollars. Li et al worked on the techno-economic assessment of camelina oil derived jet fuel using SuperPro Design software to obtain 1.06 \$/L minimum jet fuel selling price for a 225 million litres capacity bio-refinery plant (Diederichs et al., 2020). An indepth techno-economic analysis was carried out by Tongpun et al (2019) to determine economic feasibility of jet fuel derived from jatropha using a fruit to fuel process which include dehulling of jatropha fruit, combustion of jatropha shell, extraction of jatropha oil, hydroprocessing of the oil and product separation to obtain a minimum jet fuel selling

price of 6.25 \$/L. Tao et al (2017) obtained the minimum jet fuel selling price within the range of 3.8 and 11.0 \$ /gallon from the technoeconomic analysis of hydroprocessed renewable jet fuel produced from castor oil, yellow grease oil, pennycress oil, camelina oil and jatropha oil.

The main challenge for jet fuel production over the years has always been the minimization of selling price of jet fuel to make it competitive with the conventional petroleum derived jet fuel (Li et al., 2018). Jet fuel production will be cost-effective with use of cheap and available feedstock (Wang et al., 2016). Due to the challenge of food/fuel crisis, the inedible oils are preferred over the edible oils for bio-jet fuel production (Upare et al., 2020). Comparative analysis of the cost of inedible oils such as jatropha oil, camelina oil, waste cooking oil, castor oil, algal oil, palm oil and greenseed canola oil shows that the greenseed canola oil is the least expensive inedible oil with high availability in Saskatchewan, Canada (Mohammad et al. 2014; Baroi et al. 2015; Wang et al. 2016; Li et al. 2018; Wang et al. 2019;). Oleic acid constitutes 64 % of the fatty acid components of canola oil (Jones et al. 2014; Loganés et al. 2016; Edwards et al. 2017). For the production of jet fuel range hydrocarbons, 1 wt.% Sn promoted trimetallic catalyst has been proven in our previous work (Ayandiran et al; 2020) to obtain 98.2 % feedstock conversion and 80.7 % yield of jet fuel range hydrocarbons from optimal operating conditions of 339.5 °C reaction temperature, 1.6 MPa H₂ pressure, 6.2 wt. % catalyst concentration and 8.0 reaction time. The goal of this study is to carry out a technoeconomic assessment of greenseed canola derived jet fuel range hydrocarbons using oleic acid as its model compound of the feedstock. The economic feasibility of the process was done based on the optimal operating conditions obtained from our previous work (Ayandiran et al; 2020).

7.3 Methods and approaches of the simulation of jet fuel produced from greenseed canola oil over tin promoted catalyst

SuperPro version simulation package was used to prepare a process flow diagram for production of jet fuel range hydrocarbons. The package was also used for technoeconomic analysis of the process. Oleic acid was chosen as model compound of canola oil in the SuperPro simulation software. Jet fuel range hydrocarbons product was chosen as mixtures of C₈-C₁₆ hydrocarbons. The components and mixtures were chosen from the SuperPro components and mixtures database. The simulation calculations were carried out based on equilibrium model as shown in Appendix C.

7.4 Process Description

The process utilized 10,000 kg/h of oleic acid (model compound of canola oil) as feedstock and was pressurized and hydroprocessed with excess 1.6 MPa H₂. The choice of 10000 kg/h of canola oil was based on the production rate of canola oil in Saskatchewan. The H₂/feedstock mass ratio was 0.032. The process flow diagram for the plant operation is depicted in Figure 7.1 and the properties and composition of the major streams are shown in Table 7.1. The feedstock (oleic acid) in the storage tank V-101 was pumped and heated in a heat exchanger, HX 104 to 339.5 °C before leaving for the reactor. Hydrogen gas was pumped into the reactor at a pressure of 1.6 MPa to pressurize the feedstock and also for hydroprocessing of the oleic acid. 1 wt. % Sn promoted catalyst was passed to the reactor, R-101 using catalyst/feed ratio of 6.2 wt. %. The reactor is a continuous stirred tank reactor that is made up of Cr-Mo-V alloy steel with required toughness and strength properties that can withstand the reaction temperature and pressure. The product from the reactor was heated in a heat exchanger, HX-101 in order to achieve efficient separation of its components. The heated product in stream S-109 from the heat exchanger HX 101 was distilled using a short cut distillation equipment, C-105. Heptane and water were the light and heavy key components, respectively in the C-105 column. Hydrogen, carbon oxides, C₁-C₇ hydrocarbons and water were produced as distillate, S-107 from the column, while the C₇-C₁₈ hydrocarbons, water, oleic acid and the catalyst were produced as the bottom products. Another shortcut distillation column, C-102 was used to separate the most volatile component, H₂ from stream S-107, while the bulk of the components were separated as bottom products. The hydrogen produced was recycled by mixing it with hydrogen gas in stream S-112. The catalyst in the stream S-108 was separated in a screw pressing equipment, SP-101. The filtrate (S-116) from the screw pressing equipment has water and C₇-C₁₈ hydrocarbons and oleic acid. Due to the polar nature of water and its relatively high density, a decanter to separate water from stream S-116. Water was separated as the heavy phase product from the decanter, while the C₇-C₁₈ hydrocarbons and oleic acid constitute the light phase in stream S-117. The stream, S-117 was heated using a heat exchanger, HX-103 to achieve efficient separation of C₈-C₁₆ hydrocarbons in the short distillation column, C-101. The bottom product from the column, C-101 consist majorly of heptadecane, octadecane, oleic acid and minute quantity of hexadecane. The top product (S-125) from the column, C-101 is the jet fuel range hydrocarbons, C₈-C₁₆ with 0.05 wt. % of heptadecane. The percentage purity of the product

is 99.5 %. The plant capacity is 7493.1175 kg/h. The product yield with respect to the field stock is 74.93 %.

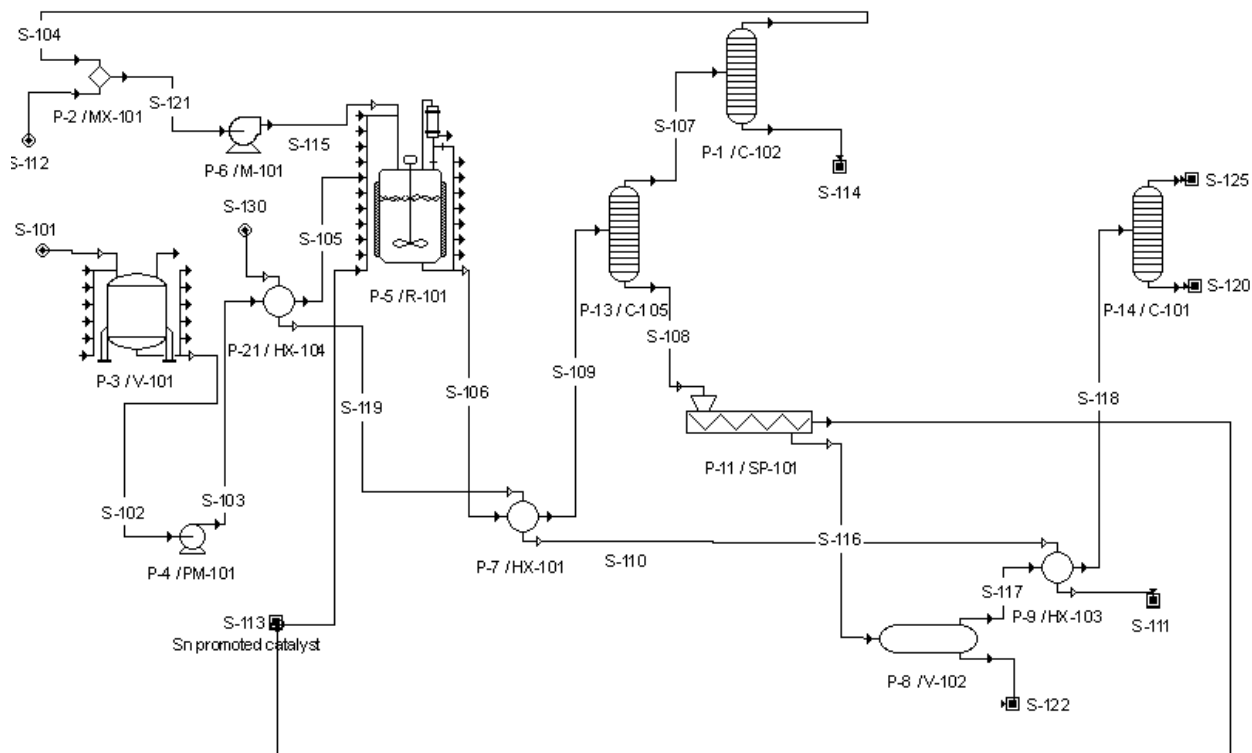


Figure 7.1. Process flow diagram for jet fuel production from green seed canola oil using 1 wt. % Sn promoted catalyst

7.5 Technoeconomic analysis

The capacity of the plant in terms of its product quantity is 7493 kg/h which is an equivalent of 59345 MT/year using 330 days operation per year and 35 days for plant for maintenance. The equipment used for production of jet fuel range hydrocarbons are shown in Fig. 7.1 and itemized with their respective cost in Table 7.2. The purchase cost was based on the Super Pro Designer 2020 built in module which utilizes the Chemical Engineering Plant Cost Index. The stirred reactor is the most expensive equipment, while the centrifugal pump is the least expensive equipment.

The fixed capital estimate for the plant operation was shown in Table 7.3. The total plant direct cost which consist of equipment purchase cost, installation, process piping, instrumentation, insulation, electrical expenses, buildings, yard improvement and auxiliary facilities were estimated to be 7.81 million dollars. Engineering and construction cost estimate constitute the total plant

indirect cost which was estimated as 4.69 million dollars (Ruffino et al. 2008; Kumar et al. 2015). Contractors and contingency fees are budgeted to be 0.75 million dollars. Therefore, the portion of the project budgeted for expenditure on fixed assets which also known as the fixed capital estimate is the sum of the total plant direct cost, total plant indirect cost and contractor's and contingency fees, which is estimated as 13.25 million dollars as shown in Table 7.3.

Table 7.1. Properties and compositions of the main streams

	Feed streams		Main Output streams		
	S101	S112	S125: Jet fuel (C ₈ -C ₁₆)	S114	S120
Temperature (°C)	25	25	213.09	100	302.25
Pressure (MPa)	0.101	0.101	0.101	0.101	0.101
Mass flow rate (Kg/h)	10000	315	7493.12	724.3	922.82
Components	Mass percent (%)				
Hydrogen	0	100	0	0.1	0
Methane	0	0	0	3.3	0
Ethane	0	0	0	6.3	0
Propane	0	0	0	9.2	0
Butane	0	0	0	12.1	0
Pentane	0	0	0	15.1	0
Hexane	0	0	0	18.0	0
Heptane	0	0	0	20.9	0
Octane	0	0	6.9	0	0
Nonane	0	0	7.8	0	0
Decane	0	0	8.6	0	0
Undecane	0	0	12.6	0	0
Dodecane	0	0	10.3	0	0
Tridecane	0	0	11.2	0	0
Tetradecane	0	0	16.0	0	0
Pentadecane	0	0	12.8	0	0
Hexadecane	0	0	13.7	0	0
Heptadecane	0	0	0.1	0	38.8
Octadecane	0	0	0	0	41.7
Oleic acid	100	0	0	0	19.5
Carbon (II) oxide	0	0	0	5.8	0
Carbon (IV) oxide	0	0	0	9.2	0
Water	0	0	0	0	0

Table 7.2. Cost of Equipment

Name of Equipment	Cost (million \$)
Vertical-on-Legs tank (V-101)	0.031
Centrifugal Pump (PM-101)	0.012
Heat Exchangers (HX-104, HX-101, HX-103)	0.318
Stirred Reactor (R-101)	0.863
Distillation Columns (C-101, C-102, C-105)	0.124
Screw Press (SP-101)	0.441
Centrifugal fan (M-101)	0.017
Decanter tank (V-102)	0.352
Mixer (MX-101)	0.54
Total	2.698

Table 7.3. Estimation of fixed capital for the plant operation

Fixed capital estimate parameters	Cost (million \$)
Total plant direct cost	7.81
Total plant indirect cost	4.69
Contractor's fee and contingency	0.75
Direct Fixed Capital cost	13.25

Table 7.4. Profitability analysis

Profitability analysis parameters	Cost (million \$)
Total capital investment	16.36
Capital investment charged to this project	3.25
Annual operating cost (Raw materials + Labor + facility + utility)	35.89
Total Revenue	37.95
Gross Profit	2.06
Taxes (40 %)	0.82
Depreciation	0.013
Net Profit	1.25

The profitability analysis of the production plant project was shown in Table 7.4. Annual operating cost was calculated from the cost of raw materials, labor, facilities and utilities (Nandi et. 2016). The capital investment charged to this project was estimated as 3.25 million dollars. Total revenue of 37.95 million dollars was evaluated based on the sales of jet fuel. The total annual operating cost was deducted from the total revenue to obtain a gross profit of 2.06 million dollars using eq. 7.1.

$$\text{Gross profit} = \text{yearly generated revenue} - \text{annual operating cost} \quad (7.1)$$

(Hamd et al., 2020)

40 % of the gross profit was accounted for taxes and deducted from the gross profit. 13000 dollars depreciation was added to the gross profit minus tax to obtain the net annual profit of 1.25 million dollars using eq. 7.2. Hence, 1.25 million dollars is the cash available as a return on the initial investment.

$$\text{Net annual profit} = \text{Gross profit} - \text{taxes} + \text{depreciation} \quad (7.2) \quad (\text{Yang et al., 2019})$$

The unit production cost/revenue and economic feasibility criteria of the project is shown in Table 7.5. The unit production cost for a kg of jet fuel was estimated as 0.60 \$/kg from the annual operating cost (\$) and annual production capacity of jet fuel (kg) using eq. 7.3, while the unit production revenue of 0.64 \$/kg was calculated from the total revenue (\$) and the annual production of jet fuel (kg) using eq. 7.4.

$$\text{Unit production cost} = \frac{\text{Annual operating cost} (\$)}{\text{Production capacity} (\text{kg})} \quad (7.3)$$

$$\text{Unit production revenue} = \frac{\text{Yearly generated revenue} (\$)}{\text{Production capacity} (\text{kg})} \quad (7.4)$$

Gross margin was estimated as 5.43 % using eq. 7.5. Hence, 5.43 % of the total revenue exceeds the annual operating cost.

$$\text{Gross margin} = \frac{\text{yearly generated revenue} - \text{Annual operating cost}}{\text{yearly generated revenue}} \times 100 \% \quad (5) \quad (\text{Marchetti et al., 2008; Zabet et al., 2018}).$$

Return on investment of 38.46 % was calculated from the net annual profit and investment charged with the project using eq. 7.6, meaning that 38.4 % of the money invested in the project will be realized as net profit within a year

$$\text{Return on investment} = \frac{\text{Net annual profit}}{\text{total investment}} \times 100 \% \quad (7.6)$$

(Zuorro et al., 2020)

The time required to pay off the initial investment from income after the start of the project is the payback time. Payback time is estimated from percentage of the reciprocal of return on investment.

$$\text{Payback time} = \frac{1}{\text{Return on investment}} \times 100 \% \quad (7.7)$$

(Cheng et al., 2020)

Hence, it will take 2.6 years to realize the initial investment from income after project start up.

Table 7.5. Unit Production Cost/Revenue and economic feasibility criteria

Unit Production Cost	0.60 \$/kg
Unit Production Revenue	0.64 \$/kg
Gross Margin	5.43 %
Return on Investment	38.46 %
Payback time	2.60 years
Minimum jet fuel selling price	0.51 \$/L

The economic evaluation parameters obtained from this jet fuel plant operation was compared with previous work on technoeconomic analysis of bio-jet fuel production as shown in Table 7.6. The minimum jet fuel selling price reported was within the range 0.68 \$/L – 1.46 \$/L. This present work has a relatively low minimum jet fuel selling price of 0.51 \$/L.

Table 7.6. A review on minimum jet fuel selling price from technoeconomic analyses of jet fuel production

Plant (MT/year)	Capacity	Minimum jet fuel selling price of jet fuel (\$/L)	References
9520		1.35	Martinez et al., 2019
66000		1.11	Tao et al., 2017
180000		1.06	Li et al., 2018
792000		1.43	Wang et al., 2016
79200		0.51	Present work

7.6 Conclusions

In conclusion, technoeconomic analysis of production of jet fuel range hydrocarbons from green seed canola oil by designing a plant with a feedstock capacity of 79200 MT/year to produce 7,493 kg/h (59,345 MT/year) of jet fuel. The budgeted annual operating cost of the project is 35.89 million dollars with a yearly generated revenue of 37.95 million dollars. The net annual profit of the project was evaluated as 1.25 million dollars with 38.46 % return on investment and 2.6 years payback time. The minimum selling price of jet fuel produced was 0.51 \$/L.

A profitable bio-jet fuel conversion route with optimized operating conditions (339.5 °C reaction temperature, 1.6 MPa H₂ pressure and 6.2 wt. % catalyst concentration), high percentage purity of jet fuel was developed with a promising return on investment and payback time reflecting its promising economic feasibility.

CHAPTER 8

Conclusions and Recommendations

8.1 Overall discussion and conclusions

Iron loading, copper loading and supports ($\text{SiO}_2\text{-Al}_2\text{O}_3$, ZSM-5 and HZSM-5) optimization was performed in the phase 1 of this research. Fe(3)-Cu(13)/ $\text{SiO}_2\text{-Al}_2\text{O}_3$ catalyst was confirmed to be the most promising catalyst performance with yield and selectivity of jet-fuel range hydrocarbons of 59.5% and 73.6%, respectively. This promising performance was ascribed to its large surface area, large pore diameter, large pore volume, low crystallite size and weak metal–support interaction from H_2 -TPR analysis, corroborating, high metal dispersion from CO chemisorption analysis, mild Brønsted acid sites from pyridine FTIR analysis and high oxophilic iron content from XPS fitting.

Fe(3)-Cu(13)/ $\text{SiO}_2\text{-Al}_2\text{O}_3$ catalyst was promoted with each of 0.5, 1 and 2 wt.% of Sn and 1 wt.% Ti and Zr in the phase 2 of this research. The 1 wt.% Sn-promoted catalyst exhibited the highest catalyst performance of 76.8% and 71.7% selectivity and yield of jet fuel range hydrocarbons, respectively. The optimum 1 wt.% Sn-promoter loading on Fe(3)-Cu(13)/ $\text{SiO}_2\text{-Al}_2\text{O}_3$ gave the highest selectivity and yield of jet fuel range hydrocarbons, hence, being the most promising catalyst. The performance of this highly promising catalyst was due to its weak metal–support interaction and low crystallite size indicating high metal dispersion, high surface area, high pore volume and high oxophilic reduced iron obtained from XPS analysis.

In the phase 3 of this research, selectivity of jet fuel range hydrocarbons and conversion of oleic acid was maximized using the best combination of process parameters for the evaluation of 1 wt.% Sn promoted Fe(3)-Cu(13)/ $\text{SiO}_2\text{-Al}_2\text{O}_3$ catalyst for oleic acid hydroprocessing for production of jet fuel range hydrocarbons. Reaction temperature of 339.5 °C, 6.2 wt.% catalyst concentration, 1.6 MPa H_2 pressure and 8.0 h reaction time was found to be the optimum process parameters that can maximize oleic acid conversion and selectivity of jet fuel range hydrocarbons at 98.2 % and 82.2 %, respectively. The minimum energy required for the reaction to take place was evaluated to be 50.7kJ/mol. This process was found to be endothermic, irreversible and non-spontaneous with 45.8kJ/mol activation enthalpy of reaction, 0.25kJ/mol entropy of reaction and the reaction's Gibb's free energy of 198.8kJ/mol at 340 °C.

In the phase 4 of this research, techno-economic assessment of greenseed canola derived jet fuel range hydrocarbons was performed using a SuperPro design software. 79,200 MT/year of oleic acid (model compound of greenseed canola oil) was hydroprocessed with 1.6 MPa of hydrogen gas over a 1 wt. % Sn promoted Fe(3)-Cu(13)/SiO₂-Al₂O₃ catalyst to produce jet fuel range hydrocarbons of production capacity of 59345 MT/year and 99.5 wt. % purity. Economic evaluation of the production process revealed a net annual profit of 1.25 million dollars, 38.46 % return on investment and 2.6 years payback time.

8.2 Recommendations

1. Investigation of hydroprocessing of real feedstock (for example, greenseed canola oil) should be a focus of future research. This will examine the efficiency of the catalysts used in this research.
2. In-situ characterization of catalysts during hydroprocessing reaction is essential and can be a focus of future research.
3. Techno-economic analysis of hydroprocessing of real feedstock should be carried out to determine a more reliable economic evaluation of the production process.
4. A flow system should be used for future research in order to have better similarity with industrial production

References

- Adepoju T.F., Ekanem U., Ibeh M.A., Udoetuk E.N. A derived novel mesoporous catalyst for biodiesel synthesis from Hura creptian-Sesamum indicum-Blighia sapida-Ayo/Ncho oil blend: A case of Brachyura, Achatina fulica and Littorina littorea shells mix. *Renew Sustain. Energy Rev.* 134 (2020) 110163-110163.
- Air Transport Action Group, Facts and figures, Geneva, Switzerland. <http://www.atag.org/facts-and-figures.html>, 2020 (accessed 7 September 2020).
- Ali M.A., Tatsumi T., Masuda T. Development of heavy oil hydrocracking catalysts using amorphous silica-alumina and zeolites as catalyst supports. *Appl. Catal. A: Gen.* 233 (2002) 77–90.
- Anand M., Farooqui S.A., Kumar R. Kinetics, thermodynamics and mechanisms for hydroprocessing of renewable oils. *Appl Catal. A: Gen.* 516 (2016) 144-152.
- Anderson M.J., Pitcomb P.J. Optimizing processes using response surface methods for design of experiments. Mark J. CRC Press, Whitcomb. Danvers, M.A., USA 6 (2017) 12-15
- Anderson V. L., McLean R. A. Design of Experiments: A Realistic Approach. Dekker, N. Y, 8 (1974) 15-19.
- Anderson C.M., Borrer C.M., Montgomery D.C. Response surface design evaluation and comparison. *J. Stat. Plan. Inference.* 139 (2009) 629-641.
- Ayandiran A.A., Boahene P.E., Dalai A.K., Hu Y. Hydroprocessing of oleic acid for production of jet-fuel range hydrocarbons over Cu and FeCu catalysts. *Catalysts* 9 (2019) 1051-1058.
- Ayandiran A.A., Boahene P. E., Nanda S., Dalai A. K., Hu Y. Hydroprocessing of oleic acid for the production of aviation turbine fuel range hydrocarbons over bimetallic Fe-Cu/SiO₂-Al₂O₃ catalysts promoted by Sn, Ti and Zr, *Molecular Catal.* 10 (2021) 111358-111367.
- Ayodele O.B., Farouk H.U., Mohammed J., Uemura Y., Daud W.M.A.W. Hydrodeoxygenation of oleic acid into n- and iso-paraffin biofuel using zeolite supported fluoro-oxalate modified molybdenum catalyst: Kinetics study. *J Taiwan Inst. Chem. Eng.* 50 (2014) 142-152.
- Baroi C., Dalai A.K., Simultaneous esterification, transesterification and chlorophyll removal from green seed canola oil using solid acid catalysts, *Catal. Today.* 207 (2013) 74–85.

- Baroi C., Dalai A.K., Process sustainability of biodiesel production process from green seed canola oil using homogeneous and heterogeneous acid catalysts, *Fuel Process. Technol.* 133 (2015) 105–119.
- Bartlett P.L., Long P.M., Lugosi G., Tsigler A. Benign overfitting in linear regression. *Proc. Natl. Acad. Sci.* 19 (2020) 73-78.
- Barzetti T., Selli E., Moscotti D., Forn L. Pyridine and ammonia as probes for FTIR analysis of solid acid catalysts. *J. Chem. Soc.* 92 (1996) 1401–1407.
- Bennici S., Gervasini A., Ravasio N., Zaccheria F. Optimization of Tailoring of CuO_x Species of Silica Alumina Supported Catalysts for the Selective Catalytic Reduction of NO_x. *J. Phys. Chem. B* 107 (2003) 5168–5176.
- Betancourt-Galindo R., Reyes-Rodríguez P.Y., Puente-Urbina B.A., Avila-Orta, C.A., Rodríguez-Fernández O.S., Cadenas-Pliego G., García-Cerda L.A. Synthesis of Copper Nanoparticles by Thermal Decomposition and Their Antimicrobial Properties. *J. Nanomater.* 2014 (2014) 1–5.
- Biesinger M.C., Laua L.W.M., Gerson A.R., Smart R.S.C. Resolving surface chemical states in XPS analysis of first row transition metals, oxides and hydroxides: Sc, Ti, V., Cu and Zn. *Appl. Surf. Sci.* 257 (2010) 887–898.
- Biesinger M.C., Payne, B.P., Grosvenor, A.P., Laua, L.W.M., Gerson, A.R., Smart, R.S.C. Resolving surface chemical states in XPS analysis of first row transition metals, oxides and hydroxides: Cr, Mn, Fe, Co and Ni. *Appl. Surf. Sci.* 257 (2011) 2717–2730.
- Boffa A.B., Lin C., Lewis acidity as an explanation for oxide promotion of metals: implications of its importance and limits for catalytic reactions, *Catal. Lett.* 27 (1994) 243–249.
- Bwapwaa, J.K., Anandraj, A., Trois, C. Possibilities for conversion of microalgae oil into aviation fuel: A review. *Renew. Sust. Energ. Rev.* 80 (2017) 1345–1354.
- Bykova M.V., Yu, D., Ermakov V.V., Kaichev O.A., Bulavchenko A.A., Saraev M., Yu, L., Yakovlev V.A. Ni-based sol–gel catalysts as promising systems for crude bio-oil upgrading: Guaiacol hydrodeoxygenation study. *Appl. Catal. B Environ.* 113 (2012) 296–307.
- Chen L., Chen C., Liang K., Chang S.H., Tseng Z., Yeh S., Chen C., Wu W., Wu. C. Nano-structured CuO-Cu₂O Complex Thin Film for Application in CH₃NH₃PbI₃ Perovskite Solar Cells. *Nanoscale Res. Lett.* 11 (2016) 402-410.

- Cheng J., Zhang Z., Zhang X., Fan Z., Liu J., Zhou J., Continuous hydroprocessing of microalgae biodiesel to jet fuel range hydrocarbons promoted by Ni/hierarchical mesoporous Y zeolite catalyst, *Int. J. Hydrogen Energy* 44 (2019) 11765-11773.
- Cheng M.H., Rosentrater K.A. Techno-economic analysis of extruding-expelling of soybeans to produce oil and meal, *Agric.* 9 (2019) 85-103.
- Choi I.H., Lee J.S, Kim C.U., Kim T.W., Lee K.Y., Hwang K.R. Production of bio-jet fuel range alkanes from catalytic deoxygenation of *Jatropha* fatty acids on a $WO_x/Pt/TiO_2$ catalyst. *Fuel*. 215 (2018) 675-685.
- Daniyan I., Bello E., Ogedengbe T., Mpofo K. Use of Central Composite Design and Artificial Neural Network for Predicting the Yield of Biodiesel. *Procedia C.I.R.P.* 89 (2020) 59-67.
- Deepak V., Rohit K., Bharat S.R., Anil K.S. Aviation fuel production from lipids by a single-step route using hierarchical mesoporous zeolites. *Energ. Environ. Sci.* 4 (2011) 1667-1675.
- Diederichs G.W., Mandegari M.A., Farzad S., Görgens J.F. Techno-economic comparison of biojet fuel production from lignocellulose, vegetable oil and sugar cane juice. *Bioresour. Technol.* 216 (2016) 331–339.
- Doliente S.S., Narayan A., Tapia J.F.D., Samsatli N.J., Zhao Y., Samsatli S. Bio-aviation Fuel: A Comprehensive Review and Analysis of the Supply Chain Components. *Front Energy Res.* 8 (2020) 1-38.
- Duan D., Zhang Y., Wang Y., Lei H., Wang Q., Ruan R. Production of renewable jet fuel and gasoline range hydrocarbons from catalytic pyrolysis of soapstock over corn cob-derived activated carbons, *Energy* 209 (2020) 118454-118464.
- Dubale A.A., Tamirat A.G., Chen H.M., Berhe T.A., Pan C.J., Su W.N., Hwang B.J., A highly stable CuS and $CuS-Pt$ modified Cu_2O/CuO heterostructure as an efficient photocathode for the hydrogen evolution reaction, *J. Mater. Chem. A* 4 (2016) 2205–2216.
- Edwards K.M., Rice G.W., Sanderson S.L. Separating oil from water: Suspension-feeding goldfish ingest liquid vegetable oil, *Can. J. Fish. Aquat. Sci.* 74 (2017) 524–532.
- Feng F., Wang L., Zhang X., Wang Q., Selective hydroconversion of oleic acid into aviation-fuel-range alkanes over ultrathin Ni/ZSM-5 nanosheets, *Ind. Eng. Chem. Res.* 58 (2019) 5432–5444.

- Feng X., Cao Y., Lan L., Lin C., Li Y., Xu H., Gong M., Chen Y. The promotional effect of Ce on CuFe/beta monolith catalyst for selective catalytic reduction of NO_x by ammonia. *Chem. Eng. J.* 302 (2016) 697–706.
- Fogler H.S. *Elements of Chemical Reaction Engineering*, Pearson Education Incorporation: Upper Saddle River, N.J. 6 (2016) 734–735.
- Fonseca A.B. Dos S., Beringhs A.O.R., Ferraz H.G., Stulzer H.K., Sonaglio D., Pezzini B.R. Liquidolid pellets: Mixture experimental design assessment of critical quality attributes influencing the manufacturing performance via extrusion-spheronization. *J. Drug Deliv. Sci. Technol.* 57(2020) 101630-101638.
- Galadima A., Muraza O. Catalytic upgrading of vegetable oils into jet fuels range hydrocarbons using heterogeneous catalysts: A review. *J. Ind. Eng. Chem.* 29 (2015) 12–23
- Gao W., Zhao Y., Liu J., Huang Q., He S., Li C., Zhao J., Wei M. Catalytic conversion of syngas to mixed alcohols over CuFe-based catalysts derived from layered double hydroxides. *Catal. Sci. Technol.* 3 (2013) 1324-1335.
- Gayary M.A., Mahanta C.L. Optimization of process parameters of osmotic pressure treatment and heat moisture treatment for rice starch using response surface methodology. *J Food Meas Charact.* 14(2020) 2862-2877.
- Guillot J.F., Fabreguette L., Imhoff O., Heintz M.C., Marco M., Sacilotti B., Domenichini S.B. Amorphous TiO₂ in LP-OMCVD TiN_xO_y thin films revealed by XPS. *Appl. Surf. Sci.* 177 (2001) 268-272
- Hamadache M., Si M.C., Laidi M., Hanini S., Belmadani S. Artificial Neural Network Models for Prediction of Density and Kinematic Viscosity of Different Systems of Biofuels and Their Blends with Diesel Fuel. *Comparative Analysis. Kem. Ind.* 69 (2020) 355-364.
- Hamd_H.H., Moharram M.R., Yssin M.A., Gouda M.A., Embaby A.K. Effect of Cutoff Grade and Stripping Ratio on the Net Present Value for Hamama Gold Project, Eastern Desert, Egypt, *J. Eng. Res. Reports.* 11 (2020) 1–8.
- He Q., Yang X., He R., Bueno L. A., Miller H., Ren X., Yang W. Koel B.E. Electrochemical and spectroscopic study of novel Cu and Fe-based catalysts for oxygen reduction in alkaline media. *J. Power Sources* 213 (2012) 169–179.

- He Q., Yang X., Ren X., Bruce E., Koel B.E., Ramaswamy N., Mukerjee S., KostECKI R. A. novel CuFe-based catalyst for the oxygen reduction reaction in alkaline media. *J. Power Sources* 196 (2011) 7404–7410.
- Hosseinpour M., Golzary A., Saber M., Yoshikawa K. Denitrogenation of biocrude oil from algal biomass in high temperature water and formic acid mixture over HZSM-5 nanocatalyst, *Fuel* 206 (2017) 628–637.
- Hosseinzadeh S.B., Ansari S.M., Shirneshan A., Fayyazi E., Najafi G., Rostami S. Evaluation of an enhanced ultrasonic-assisted biodiesel synthesized using safflower oil in a diesel power generator. *Biofuels* 11(2020) 523-532.
- Hu T., Yin H., Zhang R., Wu H., Jiang T., Wada Y. Gas phase hydrogenation of maleic anhydride to γ -butyrolactone by Cu–Zn–Ti catalysts. *Catal. Comm.* 8 (2007) 193–199.
- International Civil Aviation Organisation, 2018. Sustainable aviation fuels guide. Version 2, ICAO, Montreal.
- Ipek B., Altiparmak I. Remarkable isosteric heat of hydrogen adsorption on Cu(I)-exchanged SSZ-39. *Int J Hydrogen Energy* 8 (2020) 1-11.
- Ishihara A., Negura H., Hashimoto T., Nasu H. Catalytic properties of amorphous silica-alumina prepared using malic acid as a matrix in catalytic cracking of n-dodecane. *Appl. Catal. A Gen.* 388 (2010) 68–76.
- Jęczmionek Ł, Porzycka S.K. Hydrodeoxygenation, decarboxylation and decarbonylation reactions while co-processing vegetable oils over a NiMo hydrotreatment catalyst. Part I: Thermal effects - Theoretical considerations. *Fuel.* 131 (2014) 1-5.
- Jens W. Catalytic Hydrocracking—Mechanisms and Versatility of the Process. *ChemCatChem* 4 (2012) 292 – 306.
- Jones P.J.H., Senanayake V.K., Pu S., Jenkins D.J.A., Connelly P.W., Lamarche B., Couture P., Charest A., Baril G. L., West S.G., Liu X., Fleming J.A., McCrea C.E., Kris-Etherton P.M. Dha-enriched high-oleic acid canola oil improves lipid profile and lowers predicted cardiovascular disease risk in the canola oil multicenter randomized controlled trial, *Am. J. Clin. Nutr.* 100 (2014) 88–97.
- Jothimurugesan K., Gangwal S.K. Titania-Supported Bimetallic Catalysts Combined with HZSM-5 for Fischer-Tropsch Synthesis. *Ind. Eng. Chem. Res.* 37 (1998) 1181–1188.

- Kandel K., Anderegg J.W., Nelson N.C., Chaudhary U., Slowing I.I. Supported iron nanoparticles for the hydrodeoxygenation of microalgal oil to green diesel. *J. Catal.* 314 (2014) 142–148.
- Kazuhisa M., Yanyong L., Megumu I., Isao T. Production of Synthetic Diesel by Hydrotreatment of Jatropha Oils Using Pt-Re/H-ZSM-5 Catalyst. *Energy Fuel* 24 (2010) 2404–2409.
- Kieckhäfer K., Quante G., Müller C., Spengler T.S., Lossau M., Jonas W. Simulation-Based Analysis of the Potential of Alternative Fuels towards Reducing CO₂ Emissions from Aviation. *Simulation-Based Analysis of the Potential of Alternative Fuels towards Reducing CO₂ Emissions from Aviation. Energies* 11 (2018) 186-195.
- Kim M.Y., Kim J.K., Lee M.E., Lee S., Choi M. Maximizing Biojet Fuel Production from Triglyceride: Importance of the Hydrocracking Catalyst and Separate Deoxygenation/Hydrocracking Steps. *ACS Catal.* 7 (2017) 6256-6267.
- Konwar L.J., Oliani B., Samikannu A., Canu P., and Mikkola J. Efficient hydrothermal deoxygenation of tall oil fatty acids into n-paraffinic hydrocarbons and alcohols in the presence of aqueous formic acid. *Biomass Conv. Bioref.* 3 (2020) 1103-1112.
- Kubicka D., Jan H. Deactivation of HDS catalysts in deoxygenation of vegetable oils. *Appl. Catal. A: General* 394 (2011) 9–17.
- Kumar P., Yenumala S.R., Maity S.K., Shee D. Kinetics of hydrodeoxygenation of stearic acid using supported nickel catalysts: Effects of supports. *Appl. Catal. A Gen.* 471 (2014) 28-38.
- Kumar R., Sharma A.K., Tewari P.C. Cost analysis of a coal-fired power plant using the NPV method. *J. Ind. Eng. Int.* 11 (2015) 495–504.
- Laudenschleger D, Ruland H, Muhler M. Identifying the nature of the active sites in methanol synthesis over Cu/ZnO/Al₂O₃ catalysts. *Nat Commun.* 11 (2020) 1-10.
- Leofanti G.M., Padovan G., Tozzola B.V. Surface area and pore texture of catalysts, *Catal. Today* 41 (1998) 207–219.
- Li D., Bui P., Zhao H.Y., Oyama S.T., Dou T., Shen Z.H. Rake mechanism for the deoxygenation of ethanol over a supported Ni₂P/SiO₂ catalyst. *J. Catal.* 290 (2012) 1–12.
- Li X., Mupondwa E., Tabil L., Technoeconomic analysis of biojet fuel production from camelina at commercial scale: Case of Canadian Prairies, *Bioresour. Technol.* 249 (2018) 196–205.
- Liu G., Yan B., Chen G. Technical review on jet fuel production. *Renewable and Sustainable Energy Reviews* 25 (2013) 59-70.

- Liu S., Zhu Q., Guan Q., He L., Li W. Bio-aviation fuel production from hydroprocessing castor oil promoted by the nickel-based bifunctional catalysts. *Bioresource Technol.* 183 (2015) 93–100.
- Loganes C., Ballali S., Minto C. Main Properties of Canola Oil Components: A Descriptive Review of Current Knowledge, *Open Agric. J.* 10 (2016) 69–74.
- Lup A.N.K., Abnisa F., Daud W.M.A.W, Aroua M.K. Acidity, oxophilicity and hydrogen sticking probability of supported metal catalysts for hydrodeoxygenation process, *IOP Conf. Ser. Mater. Sci. Eng.* 334 (2018) 0–6.
- Ma T., Zhang L., Song Y., Shang Y., Zhai Y., Gong Y. A comparative synthesis of ZSM-5 with ethanol or TPABr template: Distinction of Brønsted/Lewis acidity ratio and its impact on n-hexane cracking. *Catal. Sci. Technol.* 8(2018)1923-1934.
- Malhotra R., Ali A. Lithium-doped ceria supported SBA-15 as mesoporous solid reusable and homogenous catalyst for biodiesel production via simultaneous esterification and transesterification of waste cottonseed oil. *Renew. Energy* 119 (2018) 32-34.
- Manikandan M., Venugopal A.K., Nagpure A.S., Chilukuri S., Raja T. Promotional effect of Fe on the performance of supported Cu catalyst for ambient pressure hydrogenation of furfural. *RSC Adv.* 6 (2016) 3888-3898.
- Marchetti J.M., Errazu A.F. Technoeconomic study of supercritical biodiesel production plant, *Energy Convers. Manag.* 49 (2008) 2160–2164.
- Marimuthu M., Venugopal A.K., Nagpure A.S., Satyanarayana C., Thirumalaiswamy R. Promotional effect of Fe on the performance of supported Cu catalyst for ambient pressure hydrogenation of furfural, *RSC Adv.* 6 (2015) 3888-3896.
- Martinez H. E., Ramírez V.L.F., Amezcua A.M.A., Aburto J. Process simulation and techno-economic analysis of bio-jet fuel and green diesel production — Minimum selling prices, Yang M., Rosentrater K.A. Techno-economic analysis of the production process of structural bio-adhesive derived from glycerol, *J. Clean. Prod.* 228 (2019) 388–398.
- Mayer J.T., Deibold U., Madey T.E., Garfunkel E. Titanium and reduced titania overlayers on titanium dioxide. *J. Electron Spectros. Relat. Phenomena* 73 (1995) 1-11
- Mederos N. S., Santoyo A.O., Centeno N.G., Mena C.V.Y., Trejo F., Ramírez J.E. Renewable fuels production from the hydrotreating over NiMo / γ -Al₂O₃ catalyst of castor oil methyl esters obtained by reactive extraction. 285(2020)1-11.

- Mirzayanti Y.W., Prajitno D.H., Roesyadi A., Febriyanti E. Kinetic Study of Catalytic Hydrocracking Ceiba pentandra oil to Liquid Fuels Over Nickel-Molybdenum / HZSM-5. 988(2020) 128–136.
- Mohammadshirazi A., Akram A., Rafiee S., Kalhor E. B. Energy and cost analyses of biodiesel production from waste cooking oil, *Renew. Sustain. Energy Rev.* 33 (2014) 44–49.
- Monnier J., Sulimma H., Dalai A., Caravaggio G. Hydrodeoxygenation of oleic acid and canola oil over alumina-supported metal nitrides. *Applied Catalysis A: Gen.* 382 (2010) 176–180.
- Morant C., Sanz J.M., Galan L., Soriano L., Rueda F. An XPS study of the interaction of oxygen with zirconium, *Surf. Sci.* 218 (1989) 331–345
- Morettia G., Dossib C., Fusib A., Recchiab S., Psarob R. A. comparison between Cu-ZSM-5, Cu/S-1 and Cu/mesoporous silica alumina as catalysts for NO decomposition. *Appl. Catal. B Environ.* 20 (1999)67–73.
- Muhammad M, Kandaramath H.T., Yaakob Z, Chandra S.Y., Sopian K. Overview on the production of paraffin based-biofuels via catalytic hydrodeoxygenation. *Renew Sustain Energy Rev.* 22(2013)121-132.
- Nandi S., Kwong A.T., Holtz B.R., Erwin R.L., Marcel S., McDonald K.A., Techno-economic analysis of a transient plant-based platform for monoclonal antibody production, *MAbs.* 8 (2016) 1456–1466.
- Naveenji A., Rajesh V. S., Dalai A. K. Green diesel synthesis by hydrodeoxygenation of bio-based feedstocks: Strategies for catalyst design and development. *Renewable and Sustainable Energy Reviews* 48 (2015) 240–255.
- Nur A., Mohammad A., Hamdah A., Robiah Y., Zulkifly A., Rozita O., Umer R., Azhari M.S. Kinetics and thermodynamics of synthesis of palm oil-based trimethylpropane triester using microwave irradiation. *J. Saudi Chem. Soc.* 24 (2020) 522-566.
- Olcese R., Bettahar M.M., Malaman B., Ghanbaja J., Tibavizco L., Petitjean D., Dufour A. Gas-phase hydrodeoxygenation of guaiacol over iron-based catalysts. Effect of gases composition, iron load and supports (silica and activated carbon). *Applied Catalysis B: Environmental* 129 (2013) 528– 538.
- Ouma L., Ofomaja A. Probing the interaction effects of metal ions in Mn: XFe(3-x)O₄ on arsenite oxidation and adsorption. *RSC Adv.* 10(2020) 2812-2822.

- Pattanaik B.P, Misra R.D. Effect of reaction pathway and operating parameters on the deoxygenation of vegetable oils to produce diesel range hydrocarbon fuels: A review. *Renew Sustain Energy Rev.* 73(2017)545-557.
- Platon A., Thomson W.J. Quantitative Lewis/Bronsted Ratios Using DRIFTS. *Ind. Eng. Chem. Res.* 24 (2003) 24-29.
- Rabaev M., Landau M.V., Vidruk-Nehemya R., Koukouliev V., Zarchin R., Herskowitz M. Conversion of vegetable oils on Pt/Al₂O₃/SAPO-11 to diesel and jet fuels containing aromatics. *Fuel* 161 (2015) 287–294.
- Rathi A.K. To study the effect of submerged arc welding parameters on bead geometry and hardness for mild steel (IS-2062A) using fractional factorial design. *Mater Today Proc.* 34 (2020) 525-530
- Roustilla A., Chene J., Severac C., XPS study of hydrogen and oxygen interactions on the surface of zirconium. *J. Alloys Comp.* 356-357 (2003) 330-335.
- Ruffino B., Zanetti M.C. Recycling of steel from grinding scraps: Reclamation plant design and cost analysis, *Resour. Conserv. Recycl.* 52 (2008) 1315–1321.
- Ru-ling L., Hua-qing Z., Zhi-wei W., Zhang-feng Q., Wei-bin F., Jian-guo W. Aromatization of propane over Ga-modified ZSM-5 catalysts, *J. Fuel Chem. Technol.* 43 (2015) 961-965.
- Saber O., Gobara H.M. Optimization of silica content in alumina-silica nanocomposites to achieve high catalytic dehydrogenation activity of supported Pt catalyst. *Egypt. J. Petrol.* 23 (2014) 445–454.
- Sanchez M.Z., Mauricio J.E., Paredes A.R., Gamero P., Cortés D. Antimicrobial properties of ZSM-5 type zeolite functionalized with silver. *Mater. Lett.* 191 (2017) 65–68.
- Scaldferrri C.A., Pasa V.M.D. Production of jet fuel and green diesel range biohydrocarbons by hydroprocessing of soybean oil over niobium phosphate catalyst. *Fuel* 245 (2019) 458-466.
- Scaldferrri C.A., Pasa V.M.D. Hydrogen-free process to convert lipids into bio-jet fuel and green diesel over niobium phosphate catalyst in one-step, *Chem. Eng. J.* 370 (2019) 98–109.
- Scott A.S. Estimating Crystallite Size using XRD. MIT Centre for Material Science and Engineering. <http://prism.mit.edu/X-ray> 2016 (accessed 10 May 2021).
- Sgouridis S., Bonnefoy P.A., Hansman R.J. Air transportation in a carbon constrained world: Long-term dynamics of policies and strategies for mitigating the carbon footprint of commercial aviation. *Transp. Res. Part A Policy Pract.* 45 (2011) 1077-1091.

- Shalaby N.H., Elsalamony, R.A., El Naggar A.M.A. Mesoporous waste-extracted SiO₂-Al₂O₃-supported Ni and Ni-H₃PW₁₂O₄₀ nano-catalysts for photo-degradation of methyl orange dye under UV irradiation. *New J. Chem.* 42 (2018) 9177–9186.
- Sheng H., Lobo R.F. Iron-Promotion of Silica-Supported Copper Catalysts for Furfural Hydrodeoxygenation. *ChemCatChem* 8 (2016) 3402–3408.
- Shokri A. Degradation of 4-Chloro phenol in aqueous media thru UV/Persulfate method by Artificial Neural Network and full factorial design method. *Int J Environ Anal Chem.* Published online 12 (2020) 1-15.
- Simsek S., Uslu S. Determination of a diesel engine operating parameters powered with canola, safflower and waste vegetable oil-based biodiesel combination using response surface methodology (RSM). *Fuel.* 270 (2020)117496-117504.
- Simsek S., Uslu S. Investigation of the effects of biodiesel/2-ethylhexyl nitrate (EHN) fuel blends on diesel engine performance and emissions by response surface methodology (RSM). *Fuel* 275 (2020) 118005-118012.
- Singh R.S., Singh T., Pandey A. Fungal endoinulinase production from raw Asparagus inulin for the production of fructooligosaccharides. *Bioresour Technol Reports.* 10(2020)100417-100426.
- Sotelo-Boyas R., Liu Y., Minowa T. Renewable Diesel Production from the Hydrotreating of Rapeseed Oil with Pt/Zeolite and NiMo/Al₂O₃ Catalysts. *Ind. Eng. Chem. Res.* 50 (2011) 2791–2796.
- Sousa F.P., Silva L.N., de Rezende D.B., de Oliveira L.C.A., Pasa V.M.D. Simultaneous deoxygenation, cracking and isomerization of palm kernel oil and palm olein over beta zeolite to produce biogasoline, green diesel and biojet-fuel. *Fuel.* 223(2018)149-156.
- Srifa A., Faungnawakij K., Itthibenchapong V., Assabumrungrat S. Roles of monometallic catalysts in hydrodeoxygenation of palm oil to green diesel. *Chem. Eng. J.* 278 (2015) 249–258.
- Sustainable aviation fuels guide. International Civil Aviation Organisation, <https://www.icao.int/environmentalprotection/knowledgesharing/Docs/Sustainable%20Aviation%20Fuels%20Guidevf.pdf>, 2017 (accessed 8 September 2020).
- Tao Y., Kanoh H., Kaneko K. ZSM-5 Monolith of Uniform Mesoporous Channels. *J. Am. Chem. Soc.* 125 (2003) 6044–6045.

- Tao L., Markham J.N., Haq Z., Bidy M.J. Techno-economic analysis for upgrading the biomass-derived ethanol-to-jet blendstocks, *Green Chem.* 19 (2017) 1082–1101.
- Tesfay D, Abrha S, Yilma Z, Woldu G, Molla F. Preparation, Optimization, and Evaluation of Epichlorohydrin Cross-Linked Enset (*Ensete ventricosum* (Welw.) Cheeseman) Starch as Drug Release Sustaining Excipient in Microsphere Formulation. *Biomed Res Int.* 2020;2020.
- Tirado A., Trejo F., and Ancheyta J. Simulation of bench-scale hydrotreating of vegetable oil reactor under non- isothermal conditions. *Fuel*, 275 (2020) 117960-117965
- Toyama N., Inoue N., Ohki S., Tansho M., Shimizu T., Umegaki T., Kojima Y. Influence of hollow silica-alumina composite spheres prepared using various amount of L(+)-arginine on their activity for hydrolytic dehydrogenation of ammonia borane. *Adv. Mater. Lett.* 7 (2016) 339–343.
- Tsegaye B., Balomajumder C., Roy P. Organosolv pretreatments of rice straw followed by microbial hydrolysis for efficient biofuel production. *Renew Energy.* 148(2020):923-934.
- Upare D.P., Upare P.P. Biomass-Derived Triglyceride: A Source of Renewable Aviation Fuel and Biodiesel, 698 (2020) 639.
- Verma D., Rana B.S., Sibi M.G., Sinha A.K. Diesel and aviation kerosene with desired aromatics from hydroprocessing of jatropha oil over hydrogenation catalysts supported on hierarchical mesoporous SAPO-11. *Appl. Catal. A Gen.* 490 (2015) 108–116.
- Vogelaar B. M., Eijssbouts S., Bergwerff J.A., Heiszwolf J. J. Hydroprocessing catalyst deactivation in commercial practice. *Catalysis Today* 154 (2010) 256–263.
- Wang W.C., Tao L. Bio-jet fuel conversion technologies. *Renew. Sustain. Energy Rev.* 53 (2016) 801–822.
- Wang W.C. Techno-economic analysis for evaluating the potential feedstocks for producing hydro-processed renewable jet fuel in Taiwan, *Energy* 179 (2019) 771–783.
- Wang W., Tao L. Bio-jet fuel conversion technologies. *Renew. Sust. Energ. Rev.* 53 (2016) 801–822.
- Wang W.C. Techno-economic analysis of a bio-refinery process for producing Hydro-processed Renewable Jet fuel from *Jatropha*. *Renew. Energy.* 95 (2016) 63–73.

- Wang M., Shu Z., Zhang L., Fan X., Tao G., Wang Y., Chen L., Wu M., Shi J. Amorphous Fe²⁺ rich FeOx loaded in mesoporous silica as a highly efficient heterogeneous Fenton catalyst. *Dalton Trans.* 43 (2014) 9234.
- Wei H., Liu W., Chen X., Yang Q., Li J., Chen H. Renewable bio-aviation turbine fuel production for aviation: A review, *Fuel* 254 (2019) 115599.
- Xiao Z., Jin S., Wang X., Li W., Wang J., Liang C. Preparation, structure and catalytic properties of magnetically separable Cu–Fe catalysts for glycerol hydrogenolysis. *J. Mater. Chem.* 22 (2012) 16598-16607.
- Xue H., Meng T., Liu F., Guo X., Wang S., Mao D. Enhanced resistance to calcium poisoning on Zr-modified Cu/ZSM-5 catalysts for the selective catalytic reduction of NO with NH₃, *RSC Adv.* 9 (2019) 38477–38485.
- Yanyong L., Rogelio S., Kazuhisa, M., Tomoaki M., Kinya S. Hydrotreatment of Vegetable Oils to Produce Bio-Hydrogenated Diesel and Liquefied Petroleum Gas Fuel over Catalysts Containing Sulfided NiMo and Solid Acids. *Energy Fuel* 25 (2011) 4675–4685.
- Ye R.P., Lin L., Li Q. Recent progress in improving the stability of copper-based catalysts for hydrogenation of carbon-oxygen bonds. *Catal Sci Technol.* 8 (2018) 3428-3449.
- Yue Y., Liu B., Qin P., Lv N., Wang T., Bi X., Zhu H., Yuan P., Bai Z., Cui Q., Bao X. One-pot synthesis of FeCu-SSZ-13 zeolite with superior performance in selective catalytic reduction of NO by NH₃ from natural aluminosilicates, *Chem. Eng. J.* 398 (2020) 125515-125527.
- Zabot G.L., Moraes M.N., Meireles M.A.A. Process integration for producing tocotrienols-rich oil and bixin-rich extract from annatto seeds: A techno-economic approach, *Food Bioprod. Process.* 109 (2018) 122–138.
- Zavelev D.E., Zhidomirov G.M., Tsodikov M. V. Theoretical study of deoxygenation of esters on small Pt – Sn intermetallic clusters, *Kinetics Catal.* 61 (2020) 1–39.
- Zhang Z., Wang Q., Chen H., Zhang X. Hydroconversion of Waste Cooking Oil into Bio-Jet Fuel over a Hierarchical NiMo/USY@Al-SBA-15 Zeolite. *Chem Eng Technol.* 41(2018)590-597.
- Zou S., Ji, Y., Li J., Zhang Y., Jin Z., Jia L., Su F. Novel leaflike Cu–O–Sn nanosheets as highly efficient catalysts for the Rochow reaction, *J. Catal.* 337 (2016) 1–13.

Zuorro A., Moreno-Sader K., González-Delgado A., Economic Evaluation and Techno-Economic Sensitivity Analysis of a Mass Integrated Shrimp, Polymers (Basel). 12 (2020) 2397.

Appendix A

Additional Data

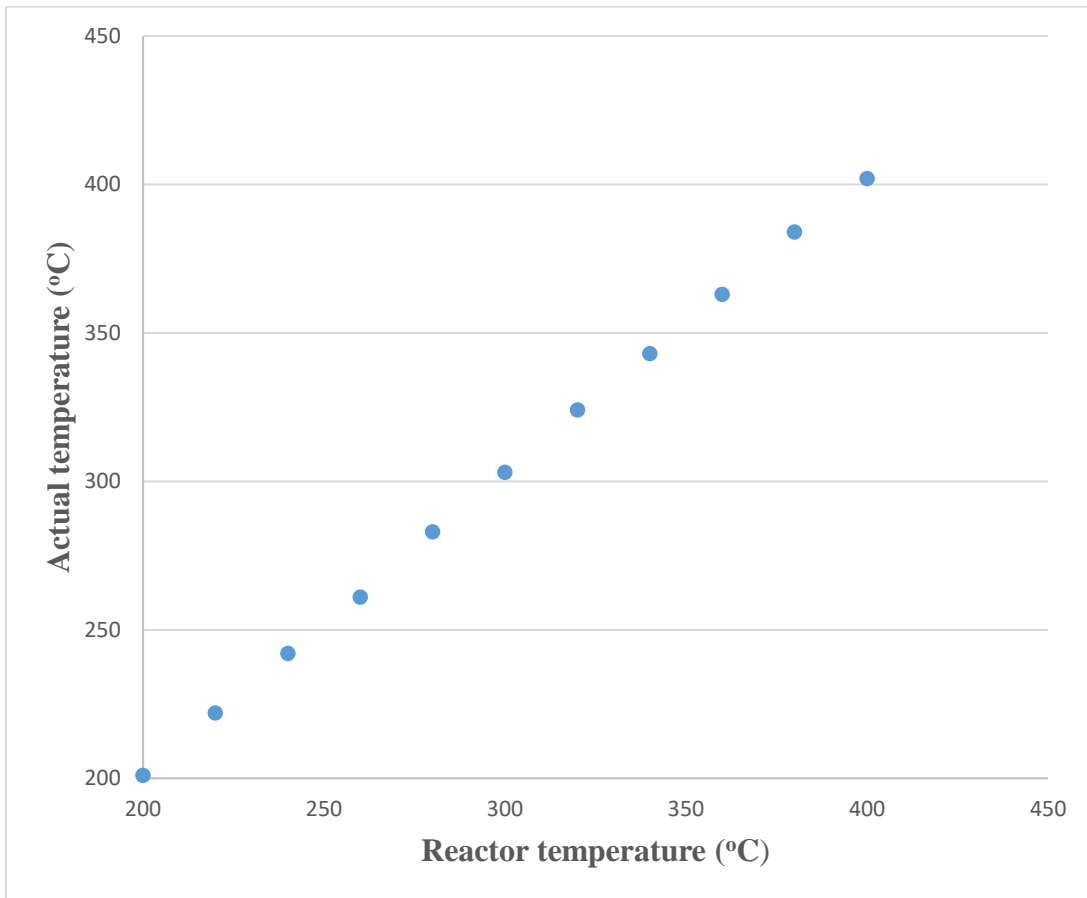


Figure A.1. Temperature Calibration of the Parr Reactor

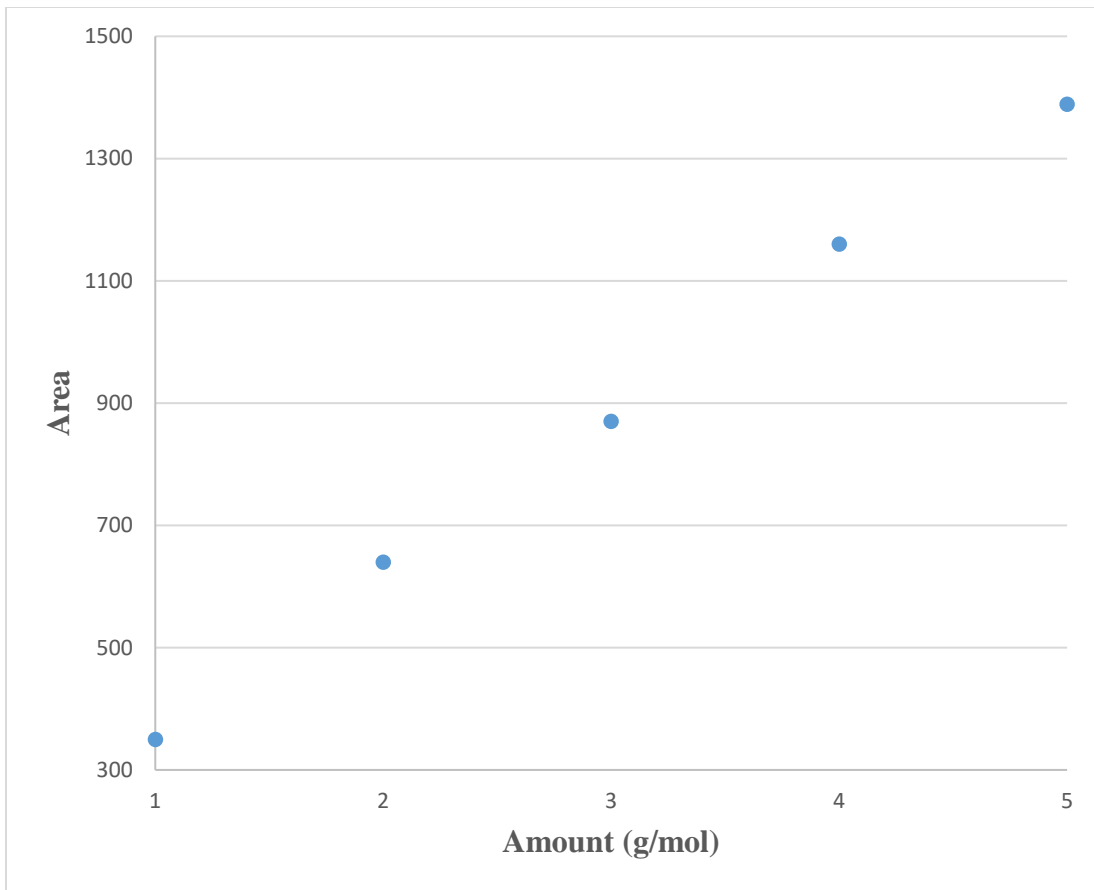


Figure A.2. GC Calibration curve for the jet fuel range hydrocarbons

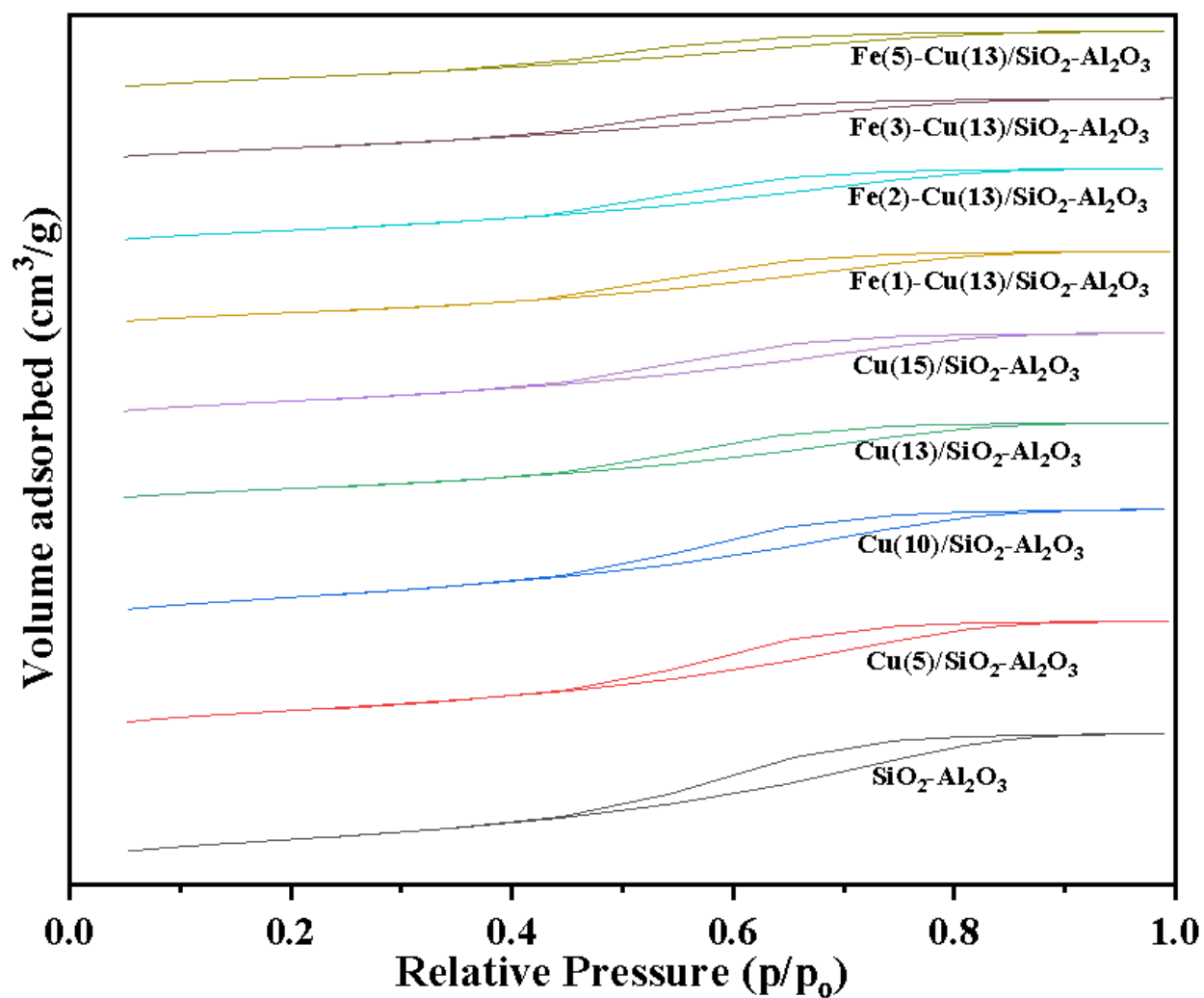


Figure A.3. N₂-adsorption isotherms of SiO₂-Al₂O₃, Cu(5)/SiO₂-Al₂O₃, Cu(10)/SiO₂-Al₂O₃, Cu(13)/SiO₂-Al₂O₃ and Cu(15)/SiO₂-Al₂O₃, Fe(1)-Cu(13)/SiO₂-Al₂O₃, Fe(2)-Cu(13)/SiO₂-Al₂O₃, Fe(3)-Cu(13)/SiO₂-Al₂O₃ and Fe(5)-Cu(13)/SiO₂-Al₂O₃ catalysts

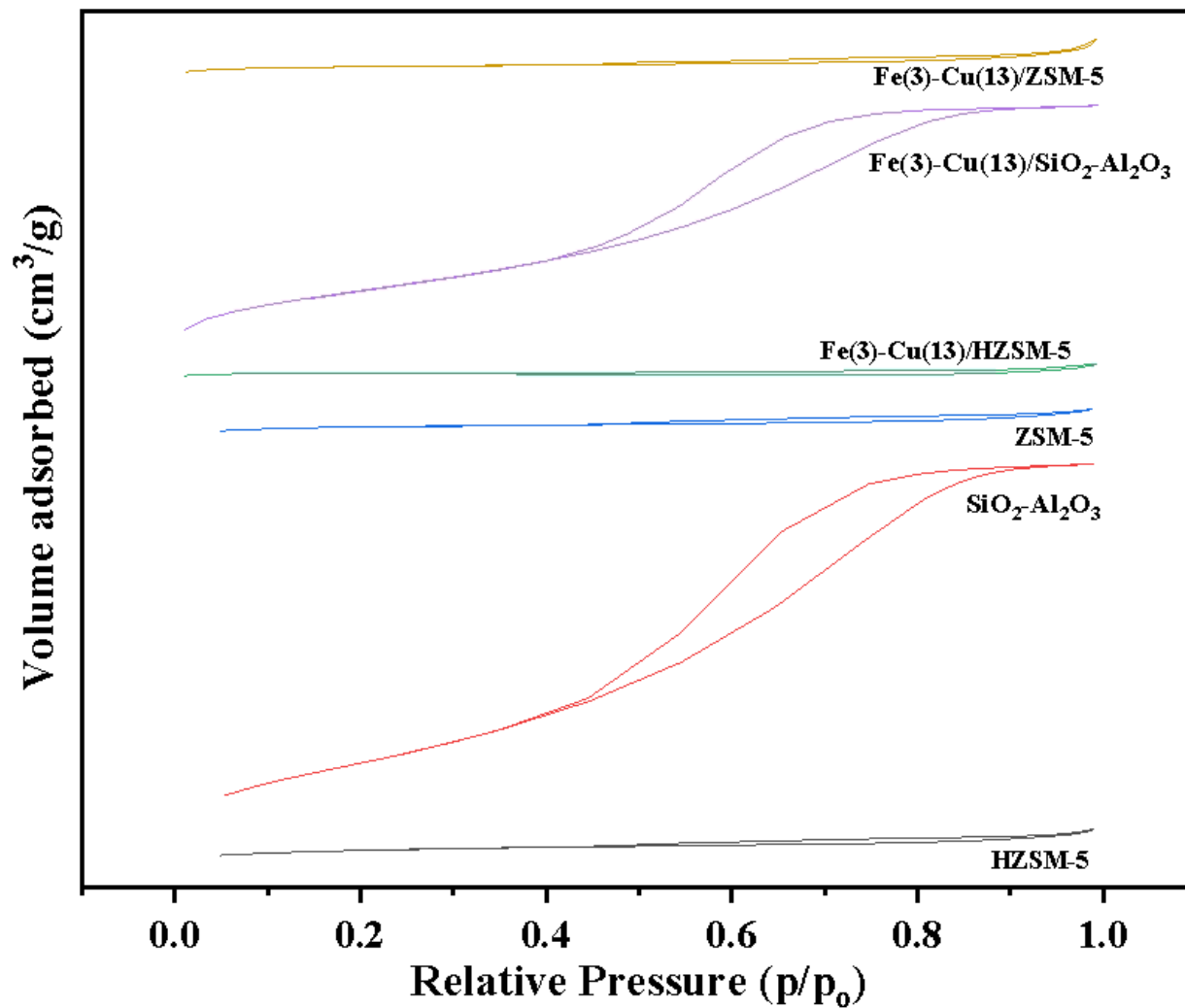


Figure A.4. N₂-adsorption isotherms of SiO₂-Al₂O₃, ZSM-5 and HZSM-5 supports; Fe(3)-Cu(13)/SiO₂-Al₂O₃, Fe(3)-Cu(13)/ZSM-5 and Fe(3)-Cu(13)/HZSM catalysts

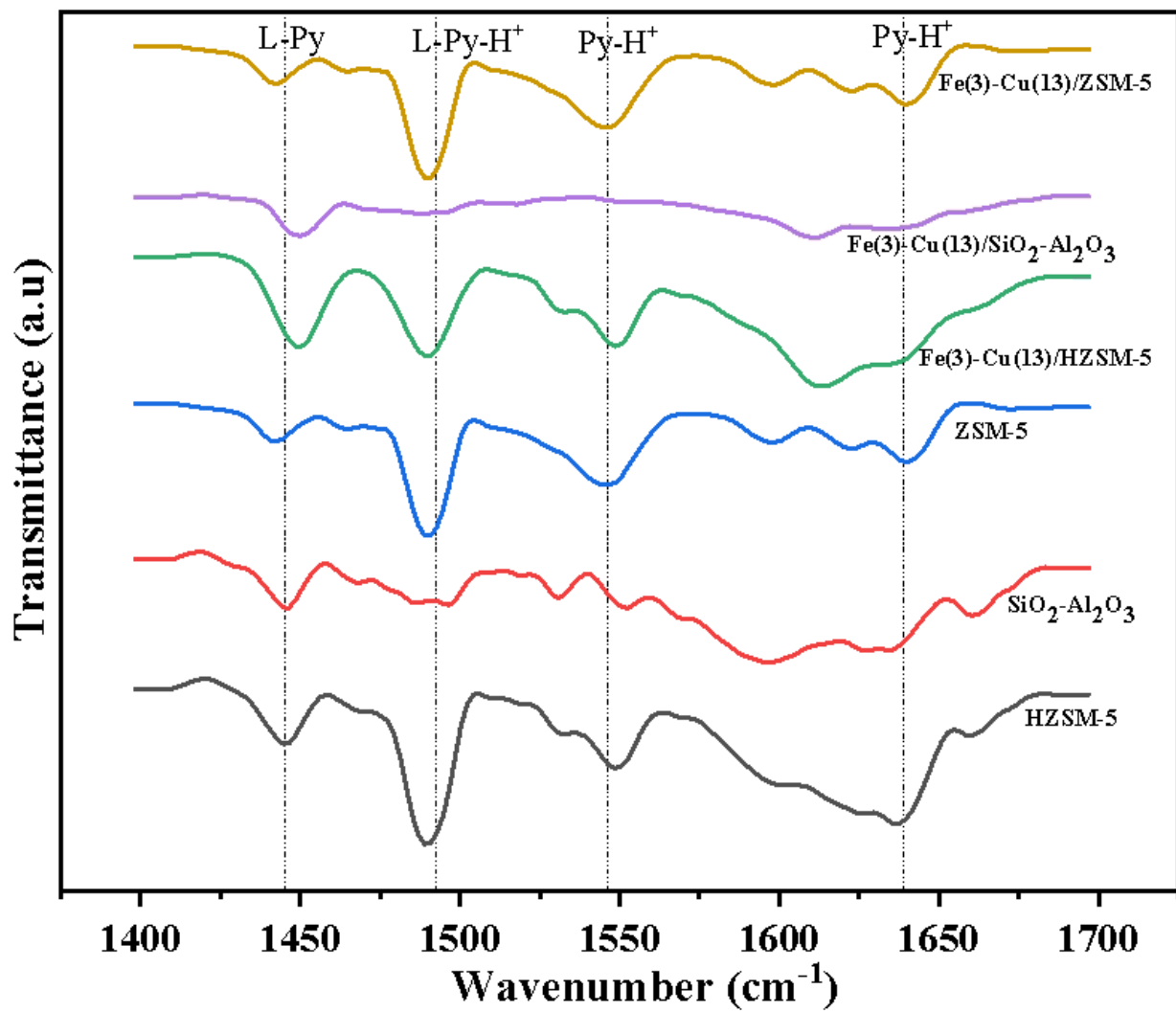


Figure A.5. Py-FTIR spectra of SiO₂-Al₂O₃, ZSM-5 and HZSM-5 supports; Fe(3)-Cu(13)/SiO₂-Al₂O₃, Fe(3)-Cu(13)/ZSM-5 and Fe(3)-Cu(13)/HZSM catalysts.

Table A.1. Selectivity of lighter hydrocarbons at t: 8 hrs; T: 300 °C, and P_{H2}: 2.07 MPa H₂ pressure

Catalysts	Product Distribution (%)		
	C ₅	C ₆	C ₇
Fe(3)-Cu(13)/SiO ₂ -Al ₂ O ₃	5.1	6.7	4.6
Fe(3)-Cu(13)/ ZSM-5	8.7	9.3	7.4
Fe(3)-Cu(13)/ HZSM-5	10.1	12.5	15.2

Table A.2. Selectivity of C₈-C₁₆ hydrocarbons at t: 8 hrs; T: 300 °C, and P_{H2}: 2.07 MPa H₂ pressure

Catalysts	Product Distribution (%)									
	C ₈	C ₉	C ₁₀	C ₁₁	C ₁₂	C ₁₃	C ₁₄	C ₁₅	C ₁₆	
Fe(3)-Cu(13)/SiO ₂ -Al ₂ O ₃	7.1	6.4	8.1	5.2	8.5	9.2	9.7	8.9	10.5	
Fe(3)-Cu(13)/ ZSM-5	7.6	8.1	7.3	7.9	6.8	4.1	3.9	4.5	3.6	
Fe(3)-Cu(13)/ HZSM-5	6.3	5.7	7.2	6.4	4.8	3.1	3.5	3.1	2.5	

Table A.3. Catalysts productivity towards C₈-C₁₆ hydrocarbons at t: 8 hours; T: 300-340 °C, and P_{H₂}: 2.07 MPa H₂ pressure

Catalysts	Temperature (°C)	G Jet Catalyst/hour	Fuel/g G Jet Fuel/m ² Area/g Catalyst	Metals Surface
Fe(3)-Cu(13)/SiO ₂ -Al ₂ O ₃	300	1.0	2.6	
	320	0.7	1.8	
	340	0.9	2.2	
Fe(3)-Cu(13)/ ZSM-5	300	0.7	1.8	
	320	0.6	1.5	
	340	0.9	2.4	
Fe(3)-Cu(13)/ HZSM-5	300	0.5	1.6	
	320	0.7	2.1	
	340	0.7	2.1	

Appendix B

Sample calculations for absence of internal mass transfer limitations

In the absence of external mass transfer limitations shown in Table 5.6, Weiz –Prater Criterion for internal diffusion

Catalysts – Fe(3)-Cu(13)/SiO₂-Al₂O₃ at the optimized reaction conditions

$$CWP=r'(obs)\times\rho_c\times R^2/D_{12},\text{ eff}C_{AS}\dots\dots\dots(B.1)$$

Where;

ρ_c - density of the catalyst, bulk density $\rho_B=\rho_c(1-\emptyset)$; R^2 - radius of the catalyst ; C_{AS} - is the reactant concentration at the catalysts surface and $r'(obs)$ - observed rate of reaction , mol/g.s

No mass transfer limitations- $C_{Ab}=C_{As}=C_A$

Using equation C.1, $c_{wp}=3.6 \times 10^{-7}$

C_{WP} value was found to be less than 1, therefore the influence of internal mass transfer is negligible.

Appendix C

SuperPro simulation results for production of jet fuel range hydrocarbons

Economics

Total Investment	16361250	\$
Total Revenues	37951736	\$/yr
Operating Cost	35891429	\$/yr
Unit Production Ref. Rate	59345490.73	kg MP/yr
Unit Production Cost		
incl. depreciation	0.60	\$/kg MP
excl. depreciation	0.60	\$/kg MP

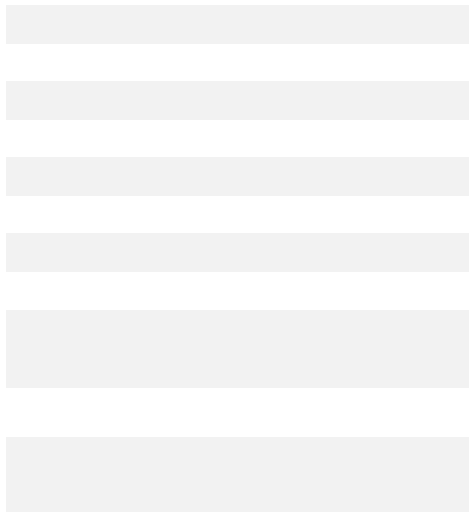
MP = Total Flow of Stream 'S-125'

Project Indices

Gross Margin	5.43	%
Return On Investment	38.48	%
Payback Time	2.60	years
IRR Before Taxes	68.05	%
IRR After Taxes	40.08	%
NPV at (10.00 %)	6978391	\$

Size

Throughput	7493.12	kg MP/hr
Annual Throughput	59345490.73	kg MP/yr



Material Consumption

Material	kg/yr	kg/h	kg/kg MP
Cu	638,352.00	80.60	0.01
Fe	147,312.00	18.60	0.00
Hydrogen	2,494,800.00	315.00	0.04
Oleic Acid	79,200,000.00	10,000.00	1.33
silica alumina	4,075,632.00	514.60	0.07
Sn	49,104.00	6.20	0.00
Water	79,200,000,000,000.00	10,000,000,000.00	1,334,558.01
TOTAL	79,200,086,605,200.00	10,000,010,935.00	1,334,559.47

Material Output

Material	kg/yr	kg/h	kg/kg MP
Butane	695,807.55	87.85	0.01
Carb. Dioxide	526,856.67	66.52	0.01
Carbon Monoxide	335,315.96	42.34	0.01
Cu	638,352.00	80.60	0.01
Decane	5,109,971.01	645.20	0.09
Dodecane	6,117,463.19	772.41	0.10
Ethane	359,964.86	45.45	0.01
Fe	147,312.00	18.60	0.00
Heptadecane	2,878,749.17	363.48	0.05
Heptane	1,199,559.63	151.46	0.02
Hexadecane	8,132,519.37	1,026.83	0.14
Hexane	1,031,650.25	130.26	0.02
Hydrogen	2,788.08	0.35	0.00
Methane	192,055.48	24.25	0.00
Nonane	4,606,206.97	581.59	0.08
Octadecane	3,046,670.52	384.68	0.05
Octane	4,102,442.92	517.99	0.07
Oleic Acid	1,425,600.00	180.00	0.02
Pentadecane	7,628,755.32	963.23	0.13
Pentane	863,728.90	109.06	0.01
Propane	527,886.20	66.65	0.01
silica alumina	4,075,632.00	514.60	0.07
Sn	49,104.00	6.20	0.00
tetradecane	9,499,940.49	1,199.49	0.16
Tridecane	6,621,227.23	836.01	0.11
Undecane	7,484,980.08	945.07	0.13
Water	79,200,009,273,503.45	10,000,001,170.90	1,334,558.17
TOTAL	79,200,086,605,200.00	10,000,010,935.00	1,334,559.47